Winter 2018

THE SAUDI ARAMCO JOURNAL OF TECHNOLOGY
A quarterly publication of the Saudi Arabian Oil Company

Saudi Aramco Journal of Technology

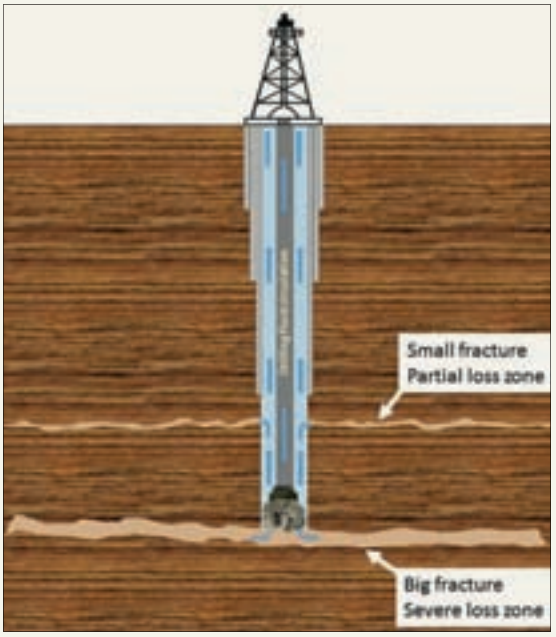

Lost circulation is one of the primary contributors for nonproductive drilling time in drilling operations. Depending on the magnitude of the fracture, lost circulation is classified as a seepage, partial or severe loss.

On the Cover

The industry standard testing equipment currently used for screening lost circulation material is limited to simulate fractures only up to 5 mm, whereas there are fractures and vugs more than 50 mm in diameter causing severe lost circulation. The new in-house designed test fixture will be able to simulate fractures/vugs of up to 40 mm. This will enable better screening and evaluation of lost circulation products and timely recommendations for field applications.

MORE SAUDI ARAMCO JOURNAL OF TECHNOLOGY ARTICLES AVAILABLE ON THE INTERNET.

Additional articles that were submitted for publication in the *Saudi Aramco Journal of Technology* are being made available online. You can read them at this link on the Saudi Aramco Internet Website: www.saudiaramco.com/jot

The *Saudi Aramco Journal of Technology* is published quarterly by the Saudi Arabian Oil Company, Dhahran, Saudi Arabia, to provide the company's scientific and engineering communities a forum for the exchange of ideas through the presentation of technical information aimed at advancing knowledge in the hydrocarbon industry.

Complete issues of the Journal in PDF format are available on the Internet at: http://www.saudiaramco.com (click on "publications").

SUBSCRIPTIONS

Send individual subscription orders, address changes (see page 70) and related questions to:

Saudi Aramco Corporate Communications
Support Department
JOT Distribution
Box 5000
Dhahran 31311, Saudi Arabia
Website: www.saudiaramco.com/jot

CONTRIBUTIONS

Relevant articles are welcome. Submission guidelines are printed on the last page. Please address all manuscript and editorial correspondence to:

EDITOR

William E. Bradshaw
The *Saudi Aramco Journal of Technology*
C-11B, Room AN-1080
North Admin Building #175
Dhahran 31311, KSA
Tel: +966-013-876-0498
Email: william.bradshaw.1@aramco.com.sa

Unsolicited articles will be returned only when accompanied by a self-addressed envelope.

PRODUCTION COORDINATION

Richard E. Doughty

DESIGN

Graphic Engine Design Studio,
Austin, Texas, U.S.A.

ISSN 1319-2388.

The *Saudi Aramco Journal of Technology* gratefully acknowledges the assistance, contribution and cooperation of numerous operating organizations throughout the company.

أرامكو السعودية
saudi aramco

Winter 2018

THE SAUDI ARAMCO JOURNAL OF TECHNOLOGY
A quarterly publication of the Saudi Arabian Oil Company

Saudi Aramco Journal of Technology

Contents

A Large Aperture Test Apparatus for Severe Lost Circulation Material Evaluation

Dr. Jothibasu Ramasamy, Dr. Md. Amanullah, and Mohammad K. Al-Arfaj

ABSTRACT

Failure to have a reliable and adequate evaluation method and apparatus for materials used to combat severe lost circulation causes significant nonproductive time (NPT) in the drilling industry, due to frequent failure to control moderate to severe loss circulation. Apart from losing whole drilling mud while drilling, lost circulation can lead to additional problems such as differential sticking, borehole instability and also well control situations if not controlled properly. There are different types of lost circulation materials (LCMs) such as fibrous, flaky, particulate, and polymers, or their blends developed to mitigate severe mud losses. Subsequently, the nonavailability of a reliable apparatus for simulating the loss zone and an appropriate testing method for evaluation of materials for severe loss scenarios make the selection of a proper loss control material very difficult, and therefore, in most cases, treatment of severe lost circulation is addressed on a trial and error basis. Moreover, the conventional severe loss control method has a very low probability of success.

To address this ongoing problem, there must be a method and apparatus to evaluate and validate products for lost circulation based on the loss zone characteristics relevant to severe loss circulation problems. The article describes a reliable test method and apparatus capable of simulating fractures and vugular zones up to 40 mm for screening and evaluating LCMs for moderate to severe loss of circulation problems.

The test apparatus is made of several components, such as a test cell, a mud reservoir, a spacer/activator reservoir, and a LCM reservoir. All of these components are engineered and assembled in a systematic way using various fixtures such as ball valves, relief valve, connecting pipes, pressure inlet, fluid outlet and various discs with slotted and circular openings and/or holes to simulate various loss zones. The test cell is capable of holding a slotted metal disk having slots up to 40 mm to represent a fractured loss zone and discs with circular holes to represent a vugular loss zone. The test apparatus has been designed to test various LCM products up to a 600 psi working pressure. The reservoir chambers containing mud, spacer and LCM slurry are individually connected to 500 psi pressure lines to push the material from the reservoir chamber to the test cell whenever required. Once the desired material is placed inside the test cell, the ball valve connecting the test cell chamber and the reservoirs is closed. The test can be carried out up to 600 psi to evaluate the blocking efficiency of the materials. The material passing through the slotted or circular hole containing discs will be collected through the outlet in the bottom of the test cell. The amount of material collected through the outlet will be used to evaluate the performance of the LCM.

The newly developed test method and apparatus will play a vital role in the screening of different materials for lost circulation and selection of the right material based on the loss type. Therefore, it is expected to have a positive contribution in trouble-free and safe drilling operations.

INTRODUCTION

Lost circulation is the partial or total loss of drilling mud or cement slurries inside the wellbore during drilling, running casing or cementing operations. Lost circulation is one of the frequently occurring challenges encountered during drilling operations and it was reported that around 20% to 25% of wells drilled around the globe encounter lost circulation[1]. Lost circulation can be encountered during any stage of the drilling operation. It results when drilling fluid or drilling mud pumped into a well returns partially, or does not return to the surface. While some fluid loss is anticipated, extreme fluid loss is undesirable from a safety, an economical, or an environmental point of view. It is one of the most difficult and expensive problems faced while drilling a well. Millions of dollars are being spent each year owing to lost circulation and the detrimental effects it causes. Lost circulation is also responsible for reduced production in that loss zones resulted in the failure to secure production tests and samples, while the plugging of production zones have led to decreased productivity[2].

Lost circulation is one of the major operation challenges of drilling and is the major contributor for nonproductive time (NPT) when drilling. Moreover, it often triggers other drilling problems that are difficult to control and usually lead to exponential growth of NPT and the unwanted cost. Even a single loss circulation event can lead to a huge financial loss by causing a series of other drilling complications that could cost the company millions of dollars[3]. In extreme cases, lost circulation problems may force abandonment of a well. Therefore, mitiga-

tion or elimination of these loss-related drilling problems is very vital for safe, economic and trouble-free drilling operations.

Lost circulation can occur in several formations, such as naturally fractured formations, cavernous formations, and high permeable formations. Lost circulation can be classified by the amount of fluid or mud lost as seepage type, moderate type, severe type, and total loss. The amount of the fluid loss and the ability to control the lost circulation with a lost circulation material (LCM) depends on the type of formation in which the lost circulation occurs. Seepage type and moderate type lost circulation may occur in high permeable formations, extremely high permeable formations — referred to as "super-K" formations — and fissured and fractured formations. In addition to the natural causes of lost circulation, subsurface formations with a narrow mud weight window, such as weak and unconsolidated formations, depleted formations, and high-pressure zone formations, may also cause a moderate type to a severe type of lost circulation, due to the creation of induced fractures in the near wellbore formation. Such lost circulation may occur when the mud weight used for well control and borehole stability exceeds the fracture gradient of the formation.

LCMs are used to mitigate the lost circulation by blocking the flow of the drilling mud into the formation. The type of LCM used in a lost circulation situation depends on the extent of lost circulation and the type of formation. LCMs may be classified into different categories, such as fibrous materials, flaky materials, granular materials, gel type materials, crosslinking polymers, and loss control slurries[4, 5]. Such materials are frequently used either as stand-alone or in combination with other materials to form a pill to control the loss of circulation. The costs incurred in lost circulation situations may be due to lost time, loss of drilling fluids, and loss of production.

There are different mechanisms to tackle the lost circulation such as physical ways of minimizing losses utilizing sized particulate materials[6, 7], chemical ways to solve the lost circulation using polymers[8, 9] or using cement as a LCM[10]. Each approach has its own pros and cons. Selection of a lost treatment method should be based on several factors, including type of losses, type of loss zone, risk factor, etc.

There are materials specifically designed to combat particular types of loss. The design of these materials include development of a LCM and its performance evaluation in the lab. The most common and widely used industry recognized method of evaluation of these LCMs is by performing a pore plugging test (PPT). It is also called a permeability plugging apparatus. For these tests, slotted disks of varying widths such as 0.5 mm, 1 mm, and 2 mm are typically used to evaluate the designed materials under a given temperature and pressure conditions. Consequently, materials claimed to be effective in controlling severe losses are also tested in a permeability plugging apparatus using a 2 mm slotted disk. In reality, the width of fractures responsible for severe losses are bigger than 2 mm[11], and the materials claimed to be effective in controlling severe losses often fail to mitigate losses. Therefore, it is not a valid test to evaluate materials for severe losses; however, there are no test apparatus available in the industry to evaluate and validate materials for extreme drilling conditions having a loss zone gap or fracture sizes of more than 2 mm. The current limitation to test LCM performance simulating extreme drilling conditions often lead to failure of a LCM treatment job that cost millions of dollars, creating a drastic increase in total operating cost.

A conventional PPT with 2 mm slotted discs, which is assumed to be effective in controlling severe losses, often lead to unsuccessful LCM treatment jobs. As such, there is need for a fit-for-purpose and appropriate test apparatus with a simulation capacity of loss zones with more than 5 mm vugs or fractures. This article describes the design and development of new LCM test apparatus that can be used to simulate fractures from 5 mm to 40 mm. The slotted disks have circular or slotted openings to simulate the fractured or vugular loss zone.

DESIGN AND METHODOLOGY

Figure 1 is the 3D diagram of the LCM testing device. The design of the instrument includes one main test cell in which the material evaluation is carried out. There are three other additional chambers, or reservoirs: (1) drilling mud, (2) spacer, and (3) LCM slurry reservoir. These additional chambers can be used to perform tests for a two component system, contamination study, delayed mixing, testing different LCMs, tandem pills evaluation, etc. The main test cell and the additional chambers are connected by a valve. To control the flow, each reservoir cell has a valve. All three chambers are connected by a connecting pipe, which on one side is connected to the main test cell by a valve, and on the other end it is connected to a hose pipe with a valve for cleaning purposes. All the cells are fitted with a cap having a pressure inlet and outlet valves, as well as a safety relieve valve. The bottom of the main test cell has a cap with a valve to collect the output from the cell. Using nitrogen gas lines, all the chambers can be pressurized and released independently without affecting the other cells.

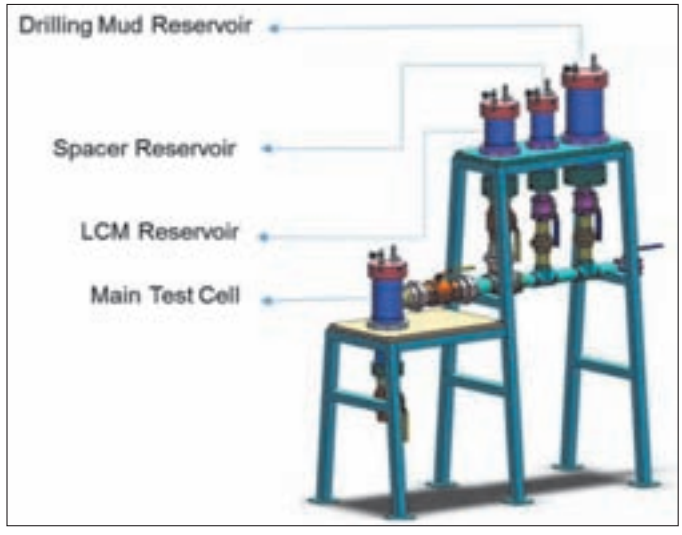

Fig. 1. A 3D model of the LCM testing device.

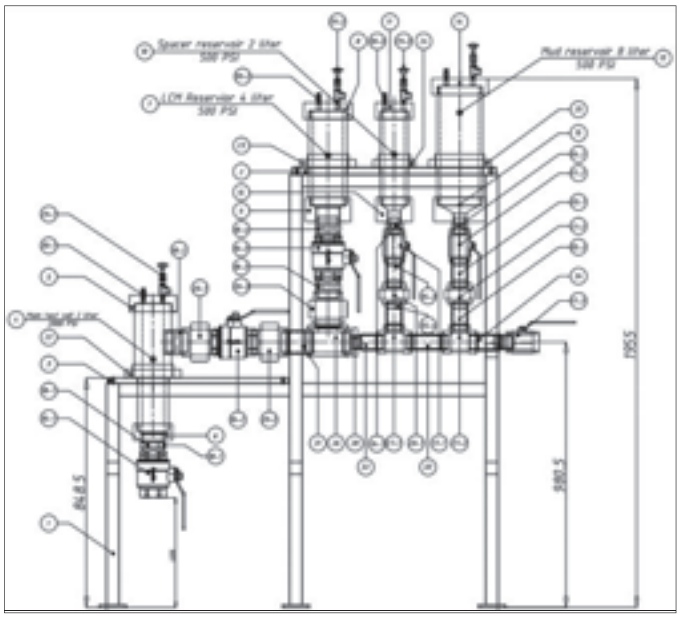

Fig. 2. Diagram of the test assembly for materials reference.

Figure 2 shows the individual parts used in the instrument. Table 1 lists the details of each part such as quantity, material type, and dimensions. We also have designed the filter mediums, which are commonly referred as slotted disks, Fig. 3. There are two types of holes, namely slotted and circular holes, which simulates the fractured or vugular zones. We have designed a number of disks with varying sizes of slots or circular openings. The range is from 5 mm to 40 mm so as to simulate a partial loss zone to a total loss zone. Depending upon the type of loss and type of material in the LCM slurry design, the selection of slotted or circular disks are made. Typically, for new material, it is recommended to start from a lower slot or circular size and move to a larger size. Therefore, we can categorize the material as for moderate or partial loss of circulation or for severe and/or total loss of circulation.

Specifications of the Test Assembly

1. Weight of the total assembly approximately: 600 kg
2. Dimensions of the assembly: 1504 mm × 669 mm × 1955 mm (59.21" × 26.34" × 76.97")
3. Mud reservoir capacity: 8 L
4. Spacer reservoir capacity: 2 L
5. LCM reservoir capacity: 4 L
6. Main test cell capacity: 2 L
7. Material of all test cells: Stainless steel
8. Maximum operating pressure of the main test cell: 600 psi/ Design pressure = 1,200 psi
9. Maximum operating pressure of the three reservoir cells: 500 psi/Design pressure = 1,000 psi

The LCM is evaluated in the main test cell using various slotted and vugular metal disks. Figure 4 shows the labeling of the parts of the test assembly. The test cell has a threaded type top cap (C1) and bottom cap (C1.1). A pressure inlet/outlet needle valve (NV1) and safety valve (SV1) are fixed on the top cap. A ball valve (V2) is attached with the bottom cap, which is the outlet of the main test cell.

There are three reservoirs included in the test assembly: (1) LCM reservoir, (2) spacer reservoir, and (3) mud reservoir. These reservoirs have threaded caps (C2, C3, and C4) and bottom caps (C2.1, C3.1, and C4.1), respectively. The top caps of the reservoir chambers are fixed with a pressure inlet/outlet needle valve (NV2, NV3, and NV4) and a safety valve (SV2, AV3, and SV4). The bottom cap of the reservoir chambers are fixed with ball valves (V3, V4, and V5), which are connected to the union. The other end of the unions of the three reservoirs are connected to Tee joints, which are connecting a pipe to the main test cell through a ball valve (V1). There is a valve fixed on the other end of the pipe.

The whole assembly is supported by a metal stand and can be mounted on the floor. The main test cell and three reservoir chambers are interconnected through various ball valves and can be disconnected by removing the unions connecting different parts. This feature will be very helpful for cleaning the test assembly.

Safety Requirements and Features

1. Do not exceed 600 psi as the primary pressure in the main test cell.
2. Do not exceed 500 psi as the primary pressure in the three reservoir cells.
3. In case of trapped pressure inside the main test cell, please use the following procedure:
   - Start relieving the pressure through the needle valve (NV1 in Fig. 4).
   - If not enough pressure is relieved, use the safety valve (SV1 in Fig. 4) for reducing the pressure.
   - If the above steps did not work, release the union for V1 (Fig. 4) slowly so the trapped pressure can escape from the main test cell.

The large aperture LCM test cell assembly is a pressure vessel and these safety precautions should be followed. Cell bodies that show signs of stress cracking, severe pitting or have damaged threads must not be used. Cell caps showing evidence of damaged or deformed threads must not be used.

4. When working with pressurized vessels, always wear protective safety glasses. Excessive pressure puts stress on four main areas of the cell:
   - Cap bending: May be observed either by eye or by

measurement.

- Cap compression: May be observed as deformed or bent threads.
- Cylinder shear: Elevated areas along the end of the cell bodies.
- Cylinder stress: Stress cracking or severe pitting will appear on the cell body.

Operation Instructions

1. Maximum operating pressure for the test cell: 600 psi
2. Maximum operating pressure for the reservoir chambers: 500 psi
3. Maximum test duration: 2 hours

#	Description	Quantity	Material	Finish Size
1	Stand	1	—	—
2	Locating Plate 1 Top	1	MS	25 × 320 × 758
3	Locating Plate 2 Middle	1	MS	25 × 436 × 670
4	Main Test Cell (2 L)	1	SS	ϕ150 × 475
5	Main Test Top Cap	1	SS	ϕ176 × 60
6	Main Test Bottom Cap	1	SS	ϕ145 × 60
7	LCM Reservoir (4 L)	1	SS	ϕ150 × 350
8	LCM Top Cap	1	SS	ϕ176 × 60
9	LCM Bottom Cap	1	SS	ϕ165 × 90
10	Spacer Reservoir (2 L)	1	SS	ϕ115 × 350
11	Spacer Reservoir Top Cap	1	SS	ϕ140 × 60
12	Spacer Reservoir Bottom Cap	1	SS	ϕ165 × 90
13	Mud Reservoir (8 L)	1	SS	ϕ181 × 440
14	Mud Reservoir Top Cap	1	SS	ϕ181 × 440
15	Mud Reservoir Bottom Cap	1	SS	ϕ207 × 60
16	Ball Valve 1 (3″)	3	SS	STD
17	Ball Valve 2 (2″)	3	SS	STD
18	Nipple 1 (3″)	4	SS	STD
19	Nipple 2 (2″)	2	SS	STD
20	Union 1 (3″)	3	SS	STD
21	Union 2 (2″)	2	SS	STD
22	Main Test Cell Adjusting Nut	2	SS	STD
23	LCM Reservoir Cell Adjusting Nut	2	SS	STD
24	Spacer Reservoir Cell Adjusting Nut	2	SS	STD
25	Drilling Mud Reservoir Cell Adjusting Nut	2	SS	STD
26	Tee 1 (3″)	1	SS	STD
27	Tee 2 (2″)	2	SS	STD
28	Reducer Connector 3″	1	SS	STD
29	Safety Valve	4	SS	STD
30	Needle Valve	4	SS	STD
31	3″ Union to 3″ Tee Connecting Pipe	1	SS	ϕ86 × 113
32	Reducer Connector to 2″ Tee Connecting Pipe	1	SS	ϕ60 × 110
33	2″ Tee to 2″ Tee Connecting Pipe	1	SS	ϕ58 × 150
34	2″ Tee Ball Valve 2 Connecting Pipe	1	SS	ϕ60 × 165
35	Ball Valve to 2″ Union Connecting Pipe	4	SS	ϕ60 × 105
36	Allen Bolt	8	STD	M10 × 30

Table 1. List of parts and key information of the LCM testing device

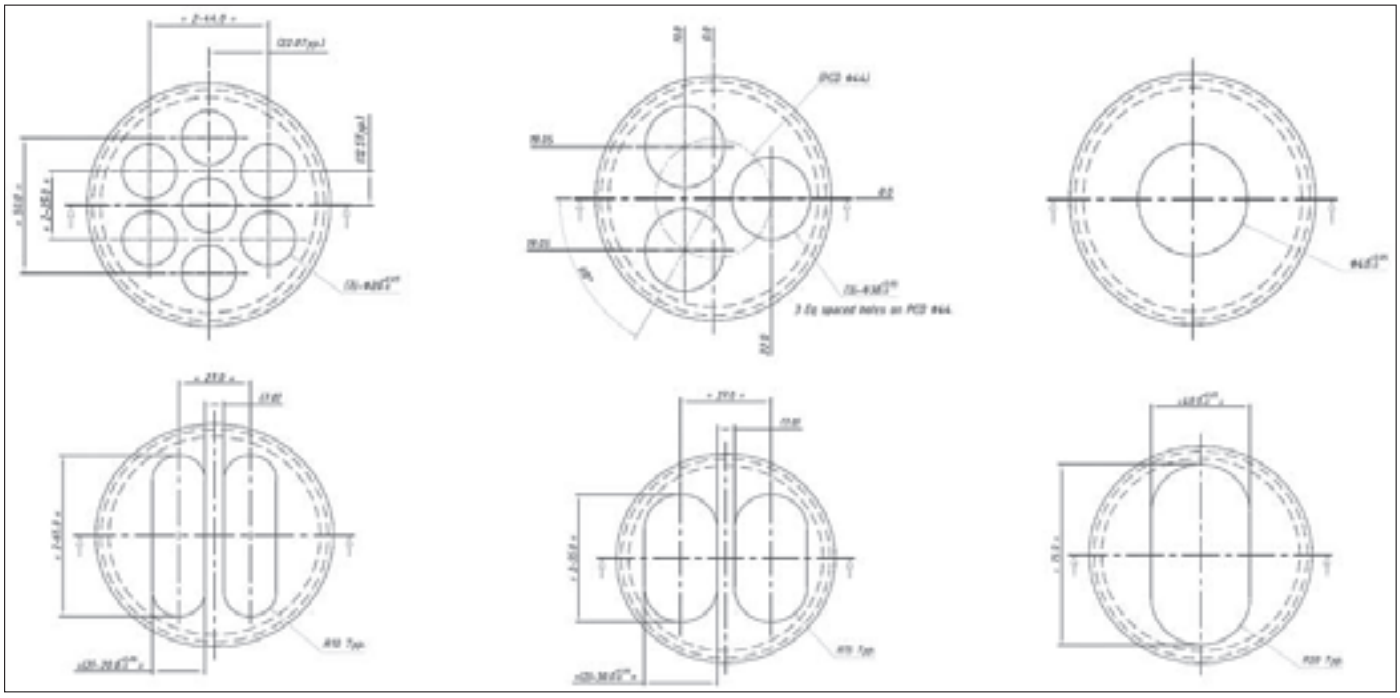

Fig. 3. Different types of slotted disks.

Preparation for the Test

1. Before starting a test, close all valves and ensure that all regulators are rotated fully counterclockwise.
2. Check all O-rings and replace any that are worn or damaged.
3. Apply a thin coat of silicone grease around the O-rings.
4. Also apply a thin coat of never-seize stopcock grease to the threads of the cell caps.
5. Check the O-ring recess to make sure it is clean. Carefully insert an O-ring inside the cell recess.
6. Select a slotted disk for the test and insert into the test cell from the bottom, and using the spanner provided, carefully screw on the cell bottom cap, C1.1.
7. Using the spanner provided, carefully screw the cell top cap, C1, into the test cell body. It is best to use a spanner wrench or strap wrench to prevent cell body rotation while installing the top cap.
8. Using the spanner provided, insert the caps of the mud, spacer, and LCM reservoir cells.
9. Start the pre-setup for the pressure safety valve for each chamber individually, based on the below instructions:
   - Ensure all caps and valves are closed completely.
   - Select and install the spring that covers the required set pressure and adjust it to the maximum.
   - Apply pressure to the chamber until it reaches the required pressure.
   - Close the inlet valve.

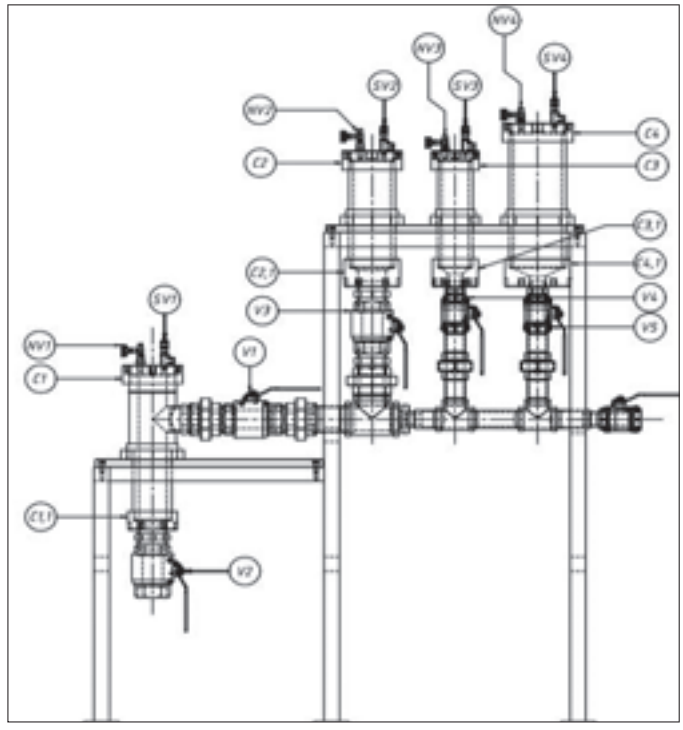

Fig. 4. Labeling of caps, needle valves, and safety valves.

- Unscrew the safety valve slowly until the pressure inside the chamber is released.
- Lock the safety valve cap into position.

Spring kits include a spring, label, 302 stainless steel lock wire with seal, spring support and installation instructions.

Always make sure not to exceed 600 psi as the primary pressure in the main test cell, and 500 psi as the primary pressure in the three reservoir cells. Keep all caps and valves closed.

LCM Placement

1. Open cap C2 and place the LCM inside the LCM chamber and close C2.
2. Open valve V1, V3, and loosen cap C1.
3. Apply pressure through NV2 to move the LCM to the test cell from the LCM chamber for 2 minutes.
4. Stop applying pressure and ensure that enough LCM is placed inside the test cell — if not, repeat #3.
5. Close C1, V1, and V3. Follow a similar procedure for the mud and spacer placement.

Conducting Tests

1. Open valve V2 and place the collection vessel at the outlet of the cell.
2. Start applying pressure through NV1 in increments, increasing by 50 psi. Keep increasing the pressure in increments until reaching the desired test pressure and close NV1 for the test duration of 30 minutes.
3. Stop applying pressure by closing NV1 in case of rapid discharge of material in bulk volume through the outlet while increasing the pressure in increments.
4. Collect and record the total amount of filtrate and/or mud for 30 minutes along with pressure and test duration.
5. After the test, disconnect all the pressure lines from NV1, NV2, NV3, and/or NV4. Then, release the pressure inside the cells by opening NV1, NV2, NV3, and/or NV4.
6. In case of trapped pressure inside the main test cell, refer to point #3 in the safety section.

For maintenance, clean the test cells, cell caps, and all fittings thoroughly after each test. Make sure all threads are clean and free of debris. Blow air through all fittings to clean out any remaining material. Before each test, lubricate all O-rings with grease to ensure a proper fit and increased life. Periodically inspect the threads of the valves for damage or wear. Replace any damaged valves if necessary.

SUMMARY

In summary, a new test setup for LCM evaluation has been designed and developed. The design included the shortcomings of the current test setup. This novel test setup can be utilized to screen and evaluate materials using 5 mm to 40 mm slotted or circular disks, and will be able to recommend suitable materials for the type and magnitude of the fractures and vugular zones. Identifying the right material of choice is extremely crucial in combating lost circulation to reduce NPT and other drilling related issues. Therefore, this new device will be very useful for drilling engineers and drilling fluid engineers to select the right material and react swiftly for curing lost circulation.

ACKNOWLEDGMENTS

The authors would like to thank the management of Saudi Aramco for their support and permission to publish this article. The authors would also like to thank Ali Radhwan and Turki Alsubaie for their involvement in manufacturing of the instrument.

This article was presented at the SPE Kingdom of Saudi Arabia Annual Technical Symposium and Exhibition, Dammam, Saudi Arabia, April 23-26, 2018.

REFERENCES

1. Economides, M.J., Watters, L.T. and Dunn-Norman, S.: *Petroleum Well Construction, Chapter 5*, John Wiley and Sons, New York, 1998, 640 p.
2. Bruton, J.R., Ivan, C.D. and Heinz, T.J.: "Lost Circulation Control: Evolving Techniques and Strategies to Reduce Downhole Mud Losses," SPE paper 67735, presented at the SPE/IADC Drilling Conference, Amsterdam, the Netherlands, February 27-March 1, 2001.
3. Kumar, A. and Savari, S.: "Loss Circulation Control and Wellbore Strengthening: Looking beyond Particle Size Distribution," paper AADE-11-NTCE-21, presented at the American Association of Drilling Engineers National Technical Conference and Exhibition, Houston, Texas, April 12-14, 2011.
4. White, R.J.: "Lost Circulation Materials and their Evaluations," paper API-56-352, presented at the Drilling and Production Practice Conference, New York, USA, January 1, 1956.
5. Whitfill, D.: "Lost Circulation Materials Selection, Particle Size Distribution and Fracture Modeling with Fracture Simulation Software," SPE paper 115039, presented at the IADC/SPE Asia Pacific Drilling Technology Conference and Exhibition, Jakarta, Indonesia, August 25-27, 2008.
6. Amanullah, M.: "Characteristics, Behavior and Performance of ARC Plug — A Date Seed-based Sized Particulate LCM," SPE paper 182840, presented at the SPE Kingdom of Saudi Arabia Annual Technical Symposium and Exhibition, Dammam, Saudi Arabia, April 25-28, 2016.
7. Ramasamy, J. and Amanullah, M.: "Two Component Lost Circulation Material for Controlling Seepage to Moderate Losses," SPE paper 188101, presented at the SPE Kingdom of Saudi Arabia Annual Technical Symposium and Exhibition, Dammam, Saudi Arabia, April 24-27, 2017.
8. Boukadi, F., Yaghi, B., Al-Hadrami, H.A., Bemani, A.A., et al.: "A Comparative Study of Lost Circulation Materials,"

Energy Sources, Vol. 26, Issue 24, 2004, pp. 1043-1051.

9. Ramasamy, J. and Amanullah, M.: "Novel Fibrous Lost Circulation Materials Derived from Deceased Date Tree Waste," SPE paper 187989, presented at the SPE Kingdom of Saudi Arabia Annual Technical Symposium and Exhibition, Dammam, Saudi Arabia, April 24-27, 2017.
10. Fidan, E., Babadagli, T. and Kuru, E.: "Use of Cement as Lost Circulation Material — Field Case Studies," SPE paper 88005, presented at the IADC/SPE Asia Pacific Drilling Technology Conference and Exhibition, Kuala Lumpur, Malaysia, September 13-15, 2004.
11. Gooneratne, C.P., Gomez Gonzalez, E.S., Al-Musa, A.S. and Osorio, H.F.: "Thirsty Reservoirs — Challenges in Drilling Through Severe Lost Circulation Zones," SPE paper 188461, presented at the Abu Dhabi International Petroleum Exhibition and Conference, Abu Dhabi, UAE, November 13-16, 2017.

BIOGRAPHIES

Dr. Jothibasu Ramasamy is a Petroleum Scientist working with the Drilling Technology Team of Saudi Aramco's Exploration and Petroleum Engineering Center – Advanced Research Center (EXPEC ARC). He joined Saudi Aramco in July 2013. Prior to this, he worked as a Research Fellow with the Department of Chemistry at the National University of Singapore and as a Postdoctoral Fellow with the Catalysis Center at the King Abdullah University of Science and Technology (KAUST), Saudi Arabia.

Jothibasu received his B.S. degree in Chemistry from Bharathidasan University, Tiruchirappalli, India, and his M.S. degree, also in Chemistry, from Anna University, Chennai, India. In 2010, he received his Ph.D. degree in Chemistry from the National University of Singapore, Singapore.

Jothibasu has published 15 technical papers and filed three patents.

Dr. Md. Amanullah is a Senior Petroleum Engineering Consultant working at Saudi Aramco's Exploration and Petroleum Engineering Center – Advanced Research Center (EXPEC ARC). Prior to joining Saudi Aramco, he worked as a Principal Research Scientist at CSIRO in Australia.

Aman is the lead inventor of a vegetable oil-based dielectric fluid (patented) that led to the formation of a spinoff company in Australia for commercialization of the product.

He has published more than 100 technical papers and filed more than 70 patents, with 18 already granted. Two of Aman's patents were highlighted in scholarly editions of two books published in the U.S.

He is one of the recipients of the 2005 Green Chemistry Challenge Award from the Royal Australian Chemical Institute. Aman also received the CSIRO Performance Cash Reward in 2006, the Saudi Aramco Mentorship Award in 2008 and 2010, the World Oil Certificate Award for nano-based drilling fluid development in 2009, the Intellectual Asset Recognition Award in 2014, and the Award of Recognition for Outstanding Contribution to the success of agricultural waste and environmental protection in 2014. His date tree waste-based product development was highlighted in *The Arabian Sun*, the *Arab News* and also in the Al Riyadh newspaper.

Aman is a member of the Society of Petroleum Engineers (SPE). He received the SPE Regional Service Award in 2014 and also the SPE Middle East Drilling Engineering Award in 2016 for his contribution to the industry. Aman also received the Middle East Oil and Gas Technical Innovation of the Year Award in 2017, and in 2018, he received the Board of Engineers Recognition Certificate for Date Seed-based ARC Plug development.

Aman received his M.S. degree (First Class) in Mechanical Engineering from the Moscow Oil and Gas Institute, Moscow, Russia, and his Ph.D. degree in Petroleum Engineering from Imperial College, London, U.K.

Mohammed K. Al-Arfaj joined Saudi Aramco in 2006 as a Petroleum Engineer, working with the Drilling Technology Team in the Exploration and Petroleum Engineering Center – Advanced Research Center (EXPEC ARC). He works in the area of drilling and completion, and has conducted several projects in the areas of shale inhibition, drilling nano-fluids, loss circulation materials, spotting fluids, swellable packers, completion fluids, and oil well cementing.

Mohammed received his B.S. degree in Chemical Engineering from King Fahd University of Petroleum and Minerals (KFUPM), Dhahran, Saudi Arabia, in 2006. In 2009, he received his M.S. degree in Petroleum Engineering from Heriot-Watt University, Edinburgh, Scotland. In 2017, Mohammed received his Ph.D. degree in Petroleum Engineering specializing in molecular modeling and experimental studies of shale fluid interactions from KFUPM.

Pressure Conditioned Modeling: Application of Time-Lapse Shut-in Pressure Data to Map Connected Reservoir Regions for Conditioning of 3D Geomodel Property Distributions

Babatope O. Kayode, Mohammed A. Al-Saleh, Stig Lyngra, and Dr. Zeid M. Al-Ghareeb

ABSTRACT

In the traditional sequential workflow approach, the geomodeler builds static models based solely on log and core data interpretations, sometimes supplemented with geological understanding, without any dynamic data considerations. In the consequent step in the traditional workflow, the simulation engineer modifies the static model, as required, to achieve a match to the dynamic data, sometimes ending up with a modified geomodel that is significantly different from the original static geomodel. In the modern integrated reservoir modeling practice, the established workflows have become a cyclical process where learnings from the history match are taken back to refine the geomodel.

For example, if a well does not produce its historical rate during history match, the permeability thickness product (*kh*) around the well is calibrated to well testing *kh* using pressure transient derivative matching, and the discrepancy is taken back to the geomodel to be resolved. With the intent to reduce history match cycle time, different approaches have been developed to use underlying data input, e.g., seismic impedance[1, 2], object-based geological features[3], pressure transient derivative signature[4-9] or pressure stream lines, to constrain the geomodel 3D property population to more realistic outcomes based on the geological understanding and available dynamic data. This article proposes a new approach: pressure conditioned modeling (PCM). The PCM concept is based on grouping wells with similar time-lapse static reservoir pressure trends into the same connected reservoir region (CRR).

PCM is based on the assumption that similarity of time-lapse shut-in reservoir pressure trends between wells in a reservoir is an indication that the producers are draining from the same CRR, and no large-scale geomodel permeability barrier is allowed to exist between these wells. Time-lapse shut-in pressure data of all wells in the reservoir are grouped on the basis of similar trends. A CRR map is created to reflect the spatial distribution of the hydraulically connected wells. The geomodeler then uses this CRR map as input in the 3D permeability variogram definition. The core permeability data existing within each CRR is distributed only inside the subject CRR in such a way that no undesirable intra-CRR permeability barrier occurs.

The PCM methodology imposes a connectivity range on 3D permeability distribution, thereby ensuring that the connected areas within a globally heterogeneous reservoir are properly designated. A synthetic model example discussed in this article resulted in a better pre-modification history match of wells, and therefore, would require less time for history matching. More realistic field development predictions would also be achieved due to the improved connectivity between injectors and producers within each CRR in a fashion consistent with the observed field data.

For reservoirs with different multiple distinct multiwell pressure trends in the existing production history, the PCM concept should be used as it will produce a higher quality initial geomodel, and significantly reduce the time required to obtain a history matched model without the need for significant modifications.

INTRODUCTION

The motivation for this new methodology is that the current practice of using only core and log data as the basis of building geomodels quite often results in geomodels that have to be significantly modified before achieving a history matching of observed dynamic data, e.g., average drainage area pressure. This arises because while core and log data could have a good vertical resolution of heterogeneity, they do not offer any understanding of lateral continuity of properties due to the fact that these data are obtained from samples with a limited volume of investigation. Several approaches have been used to infer the property distribution between wells, including seismic acoustic impedance maps, sedimentary depositional facies map, and pressure transient calibration. In the absence of these maps, the inter-well region property distribution are based on purely geostatistical algorithms like sequential Gaussian simulation (SGS).

A new methodology has been developed, which uses time-lapse average shut-in pressure data to determine a connected reservoir region (CRR) map. According to Dake's fundamentals of reservoir engineering[10], wells producing at a pseudo-steady-state within a reservoir, develop a contiguous drainage volume, which is a function of their production rates, Fig. 1.

If any of these wells is shut-in, its stabilized shut-in pressure represents the average pressure within its pre-shut-in drainage volume. Therefore, as the individual wells are shut-in at

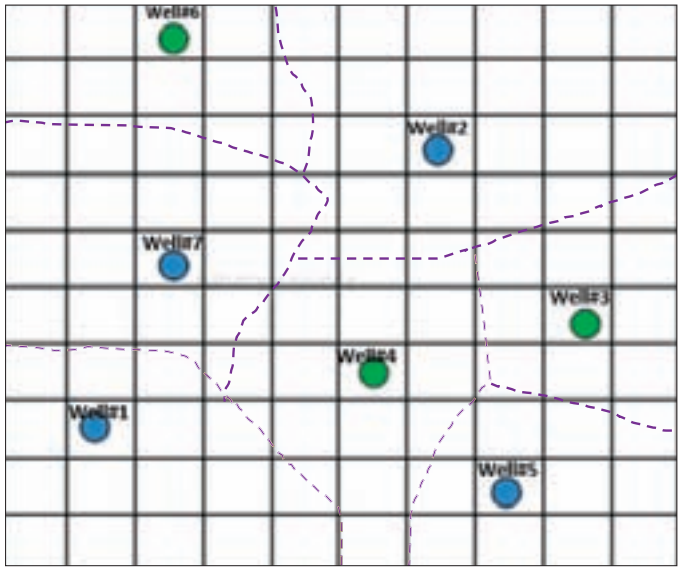

Fig. 1. Illustration of contiguous drainage boundaries developed around wells during production.

different times and stabilized pressure recorded, we can determine the presence of connectivity, baffle or barrier between different drainage volumes. In a non-faulted reservoir, wells that show a similar time-lapse average drainage area pressure trend are connected, while wells that show different trends indicate the presence of permeability baffle. A CRR map is created by spatially delineating all regions where well average drainage area pressures show a similar time-lapse trend.

The geomodeler then uses the CRR map in his workflow to determine areas where inter-well property distribution should reflect continuity, baffles or barriers.

The objective of pressure conditioned modeling (PCM) is to build a geomodel that honors both well data — logs and cores — and reservoir performance data — time-lapse pressure communication — with the goal that such models would require little or no further modifications during history matching.

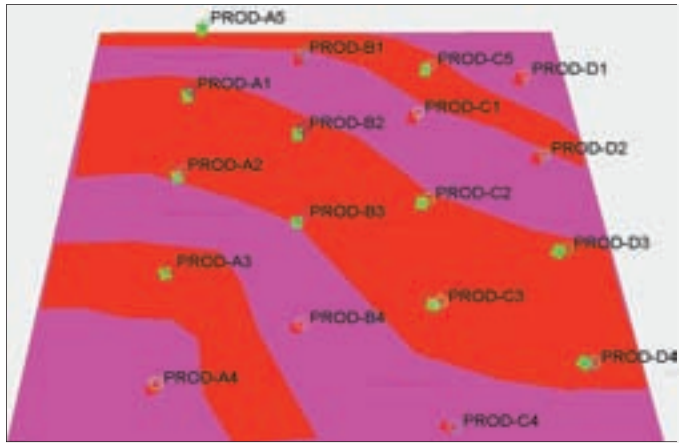

Fig. 2. Permeability distribution in a hypothetical geomodel containing three sets of high permeability channels cutting through low permeability levees. The high permeability channel sands are colored red while the low permeability levees are colored pink.

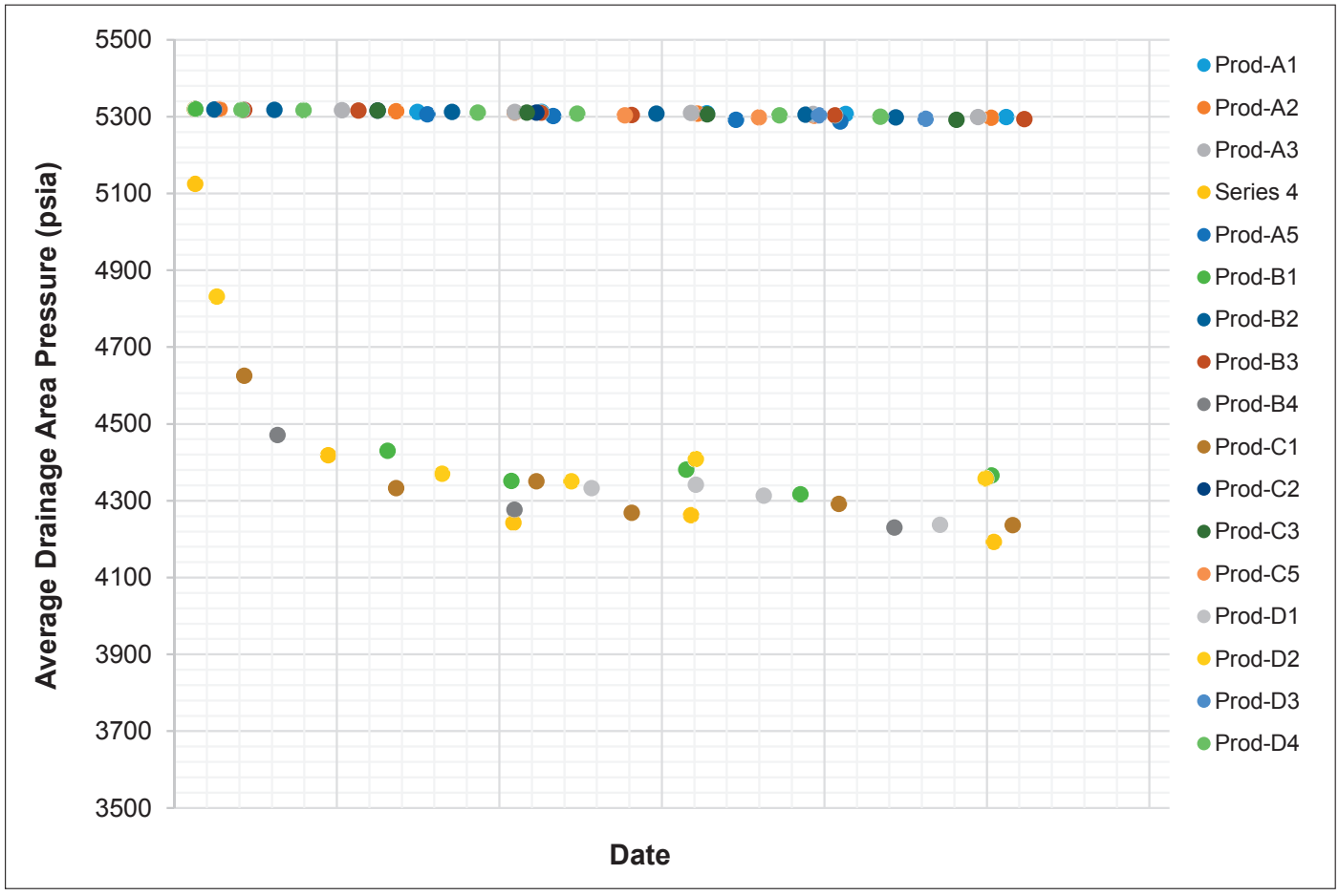

Fig. 3. Time-lapse drainage area pressure over a period of 15 years for all wells in the hypothetical geomodel.

	Prod-A1	Prod-A2	Prod-A3	Prod-A4	Prod-A5	Prod-B1	Prod-B2	Prod-B3	Prod-B4
Pressure Data	Yes	Yes	Yes	Yes	Yes	Yes	Yes	Yes	Yes
Core Data	Yes	—	Yes	—	Yes	Yes	Yes	—	Yes
K md	500	—	500	1	500	1	500	—	1

	Prod-C1	Prod-C2	Prod-C3	Prod-C4	Prod-C5	Prod-D1	Prod-D2	Prod-D3	Prod-D4	Prod-D5
Pressure Data	Yes	Yes	Yes	Yes	Yes	Yes	Yes	Yes	Yes	Yes
Core Data	Yes	—	Yes	—	Yes	Yes	—	Yes	—	—
K md	1	—	500	—	500	1	1	500	—	—

Table 1. A list of the data available per well

INPUT DATA DESCRIPTION

There are two pieces of input data that go into PCM: (1) multiwell time-lapse average drainage area pressure, and (2) core permeability. In this article, the inputs are based on a synthetic data set.

A hypothetical 15 km × 15 km × 200 ft geomodel containing three channel systems was constructed. A permeability of 1 md was imposed everywhere in the model except within the channels in which a permeability of 500 md was defined. A total of 18 producers were defined in the model and the reservoir was produced in depletion mode with all wells perforated from top to bottom of the reservoir.

All the wells have a shut-in average drainage area pressure, which was measured over a 15 year production history, but only nine out of these wells have core permeability data.

In this particular exercise, the channels are known from high resolution seismic acoustic impedance. Subsequently, the goal of this article is to show how to use information from time-lapse pressure data to infer the description of permeability heterogeneity when seismic acoustic impedance data is not available. Figure 2 shows the permeability distribution in the hypothetical geomodel, and all the well locations. In red are the high permeability channel sands and in pink are the low permeability levees.

Figure 3 shows the time-lapse average drainage area pressure of all the wells over a production period of 15 years. Each average drainage area pressure is based on 72 hours of shut-in duration.

Core permeability data is also available on some of the wells, Table 1.

METHODOLOGY

If we use the current practice of geostatistical distributions, e.g., SGS to distribute the available core permeability data, the resulting geomodel is as shown in Fig. 4.

Consequently, from Fig. 3, two clear trends of pressure behavior can be identified as some wells show very little pressure depletion while other wells show a significant depletion. After a detailed investigation, it was confirmed that this reservoir does not contain any structural compartmentalization, although it is known to be a channelized system of good sand cutting through a much poorer levee.

Wells within each pressure group were then identified, Table 2. Each group is called a CRR, where non-depleted wells = 1, and depleted wells = 0.

Figure 5 shows the different well locations with their corresponding CRR flags.

Next, geologically/depositionally reasonable polygons are drawn to spatially delineate the different CRR regions, and as expected, several realizations are possible at this stage. Three scenarios are presented:

1. A geomodeling tool is allowed to spatially delineate similar CRR flags with no constraints.
2. A geomodeling tool is allowed to delineate the CRR flags with constraint on channel width and orientation.
3. Manual delineation of the CRR flag's constraint to observed seismic acoustic impedance trend.

The spatial delineation polygons created were converted into a CRR map, which is then used as a sort of variogram

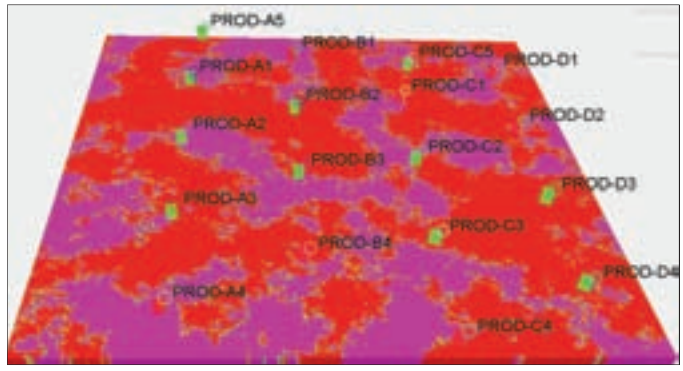

Fig. 4. Attempt to recreate the hypothetical geomodel by using the well's core permeability data by applying SGS.

	Prod-A1	Prod-A2	Prod-A3	Prod-A4	Prod-A5	Prod-B1	Prod-B2	Prod-B3	Prod-B4
Pressure Data	Yes	Yes	Yes	Yes	Yes	Yes	Yes	Yes	Yes
Core Data	Yes	—	Yes	—	Yes	Yes	Yes	—	Yes
K md	500	—	500	1	500	1	500	—	1
CRR	1	1	1	0	1	0	1	1	0

	Prod-C1	Prod-C2	Prod-C3	Prod-C4	Prod-C5	Prod-D1	Prod-D2	Prod-D3	Prod-D4	Prod-D5
Pressure Data	Yes	Yes	Yes	Yes	Yes	Yes	Yes	Yes	Yes	Yes
Core Data	Yes	—	Yes	—	Yes	Yes	—	Yes	—	—
K md	1	—	500	—	500	1	1	500	—	—
CRR	0	1	1	0	1	0	0	1	1	—

Table 2. Categorizing of the wells into CRR regions based on time-lapse drainage area pressure trend

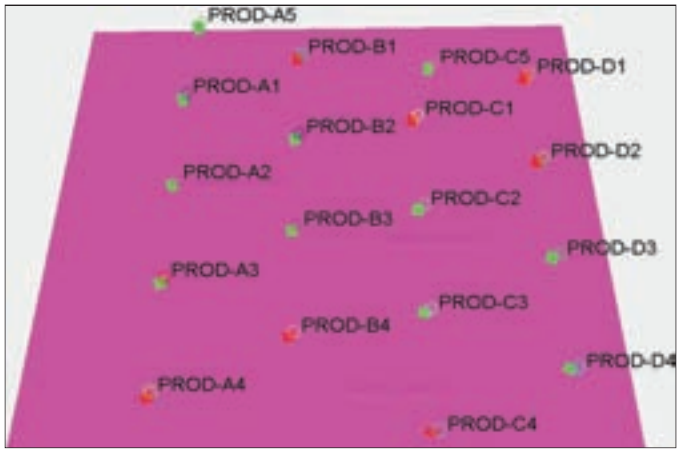

Fig. 5. Wells and their corresponding CRR flags. The green flag represents wells without significant pressure depletion, and the red flag represents wells with significant pressure depletion.

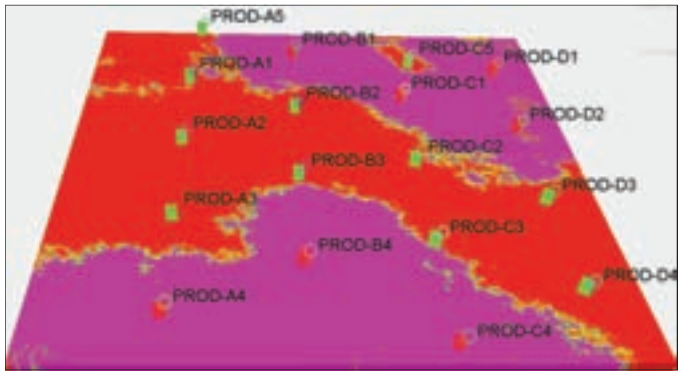

Fig. 6. The CRR map-based permeability distribution when the geomodeling tool is allowed to spatially connect the CRR flags with no constraints.

guide to distribute permeability into the model using only wells within each CRR to distribute properties within the CRR, and to ensure that no large-scale low permeability barriers occur within each CRR.

The resulting permeability distribution for the different CRR scenarios discussed are as shown in Fig. 6, Fig. 7, and Fig. 8.

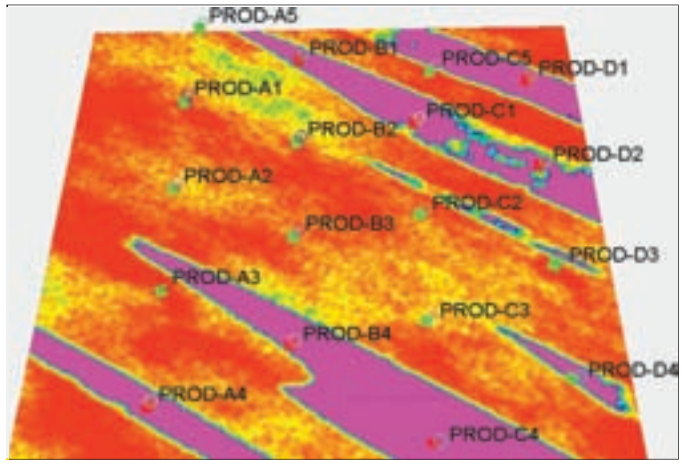

Fig. 7. The CRR map-based permeability distribution when the geomodeling tool is allowed to spatially connect the CRR flags with constraints on channel width and orientation.

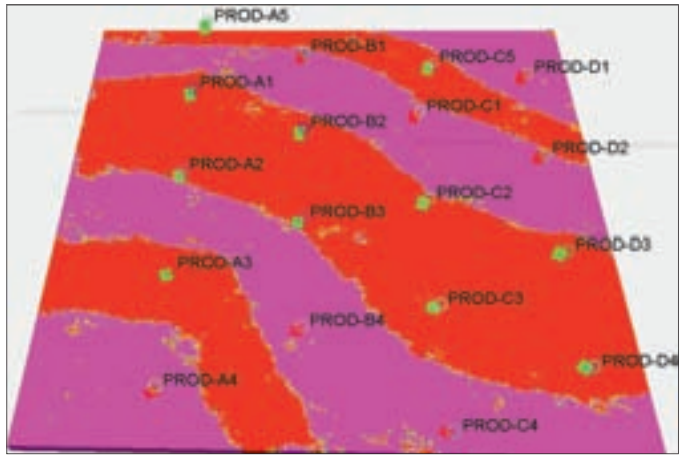

Fig. 8. The CRR map-based permeability distribution with the manual connection of the CRR flags constrained to observe seismic impedance trends.

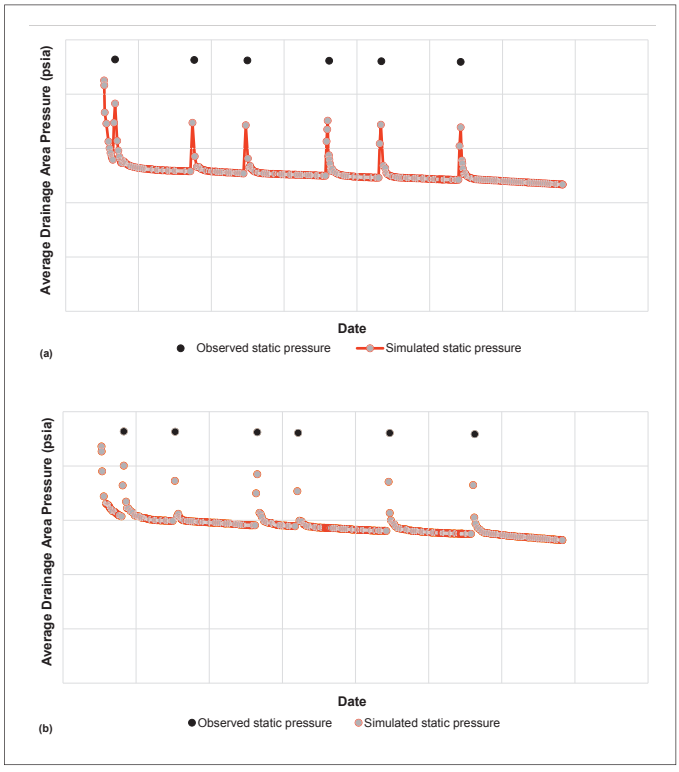

Fig. 9. Pressure comparison showing that the permeability distributed around Prod-A2 (a), and Prod-A3 (b), by SGS modeling is inconsistent with the wells' observed static pressure performance.

DISCUSSION OF RESULTS

In the extreme case where we have a complete understanding of the channel configuration, due to availability of seismic acoustic impedance, we can generate a CRR map based on that understanding and use that map as a trend control for permeability distribution, Fig. 8, to obtain a perfect replica of the hypothetical reservoir model. But this situation is rarely the case.

In reality, geomodels are built to respect well control data as much as possible, but properties distribution between well control points are based on best judgement, better algorithms or using other static properties like facies, seismic acoustic impedance, etc. Once the geomodel has been built, it is now passed to the simulation engineer who would need to enhance or degrade the permeability between well control points to match the dynamic data. The model based on SGS and the model based on PCM scenario-1 were run in simulation and the results are discussed next.

Previously, in Fig. 4, we saw that the geomodel created from SGS honors the permeability data at every well where there is core data, but in wells such as Prod-A2 and Prod-B3 where there is no core data, low permeability was distributed around these wells by the SGS algorithm. There is no way to know whether the permeability distributed around Prod-A2 and Prod-B3 are consistent with dynamic data or not at the phase of static modeling. When the model is run in simulation, the following observations can be made:

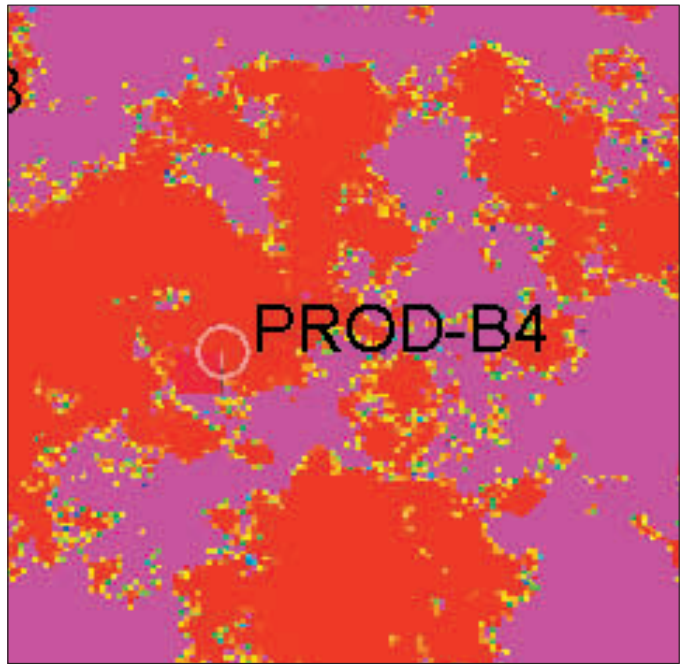

Fig. 10. Prod-B4 low core permeability was captured at the well's location, but the SGS modeling puts high permeability values immediately around the well.

- These two wells could not reproduce their historical production rate.
- These two wells experienced more pressure depletion than the observed pressure data, Fig. 9.

Another limitation of the purely SGS workflow can be seen in Prod-B4, Fig. 10, which is a close-up view of Fig. 4. The geomodel appropriately captures the low well core data permeability at the well level, but immediately away from the well, we see a lot of high permeability grids. There is no way to detect if there is anything wrong with this geomodel realization at the phase of static modeling, but when this model is taken into simulation, it is observed that the simulated pressure is much higher than the observed pressure data, Fig. 11. This is linked to the high permeability grids that have been distributed close to the well, thereby making Prod-B4 behave like a CRR = 1 region instead of a CRR = 0 region.

To improve the match of these example wells, the simulation engineer would have to use permeability multipliers to

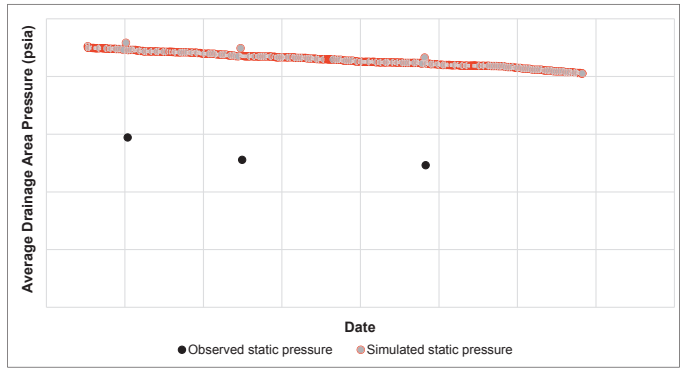

Fig. 11. Pressure comparison showing that permeability distributed around Prod-B4 by SGS modeling is inconsistent with the wells' observed pressure performance.

re-work the original static model. If the dynamic understanding of the CRR has been incorporated into the geomodeling from the beginning, the match of the original static model to observe dynamic data could be significantly enhanced.

Going back to Prod-A2 and Prod-B3, but now using the model incorporating the CRR flags previously seen in Fig. 6, we can see that even though Prod-A2 and Prod-B3 do not have core permeability data, the good permeability was populated around them because they have been flagged as CRR = 1, and the good permeability around CRR = 1 cored wells have been extended to them in the property distribution.

Figure 12 shows better pressure matches for Prod-A2 and Prod-A3 using the CRR flag constrained model than by just using a pure SGS model.

The pressure depletion of Prod-B4 is also better matched

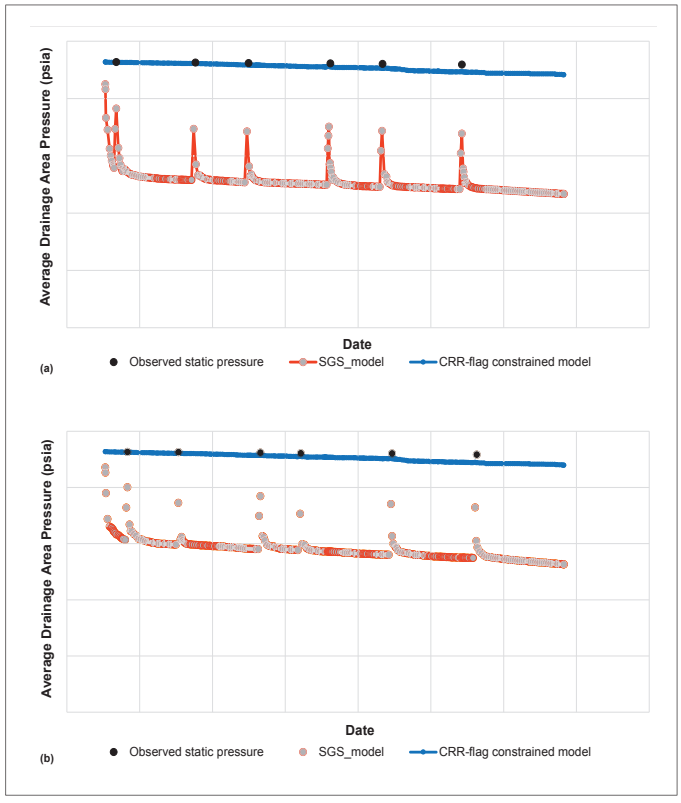

Fig. 12. Pressure comparison showing that permeability distributed around (a) Prod-A2, and (b) Prod-A3, using the CRR flag constrained model shows a better match the by just using a pure SGS model.

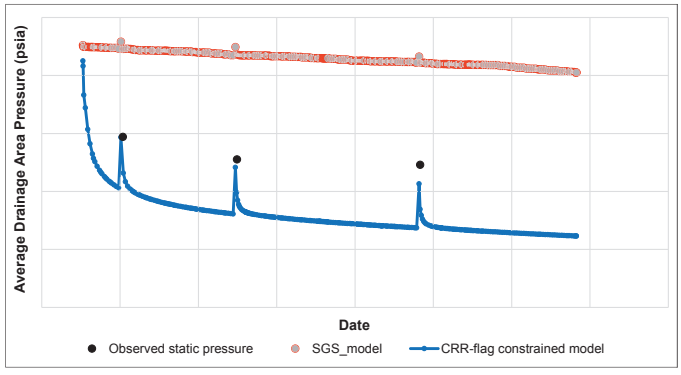

Fig. 13. Pressure comparison showing that permeability distributed around Prod-B4 is also better matched with the CRR flag constrained geomodel.

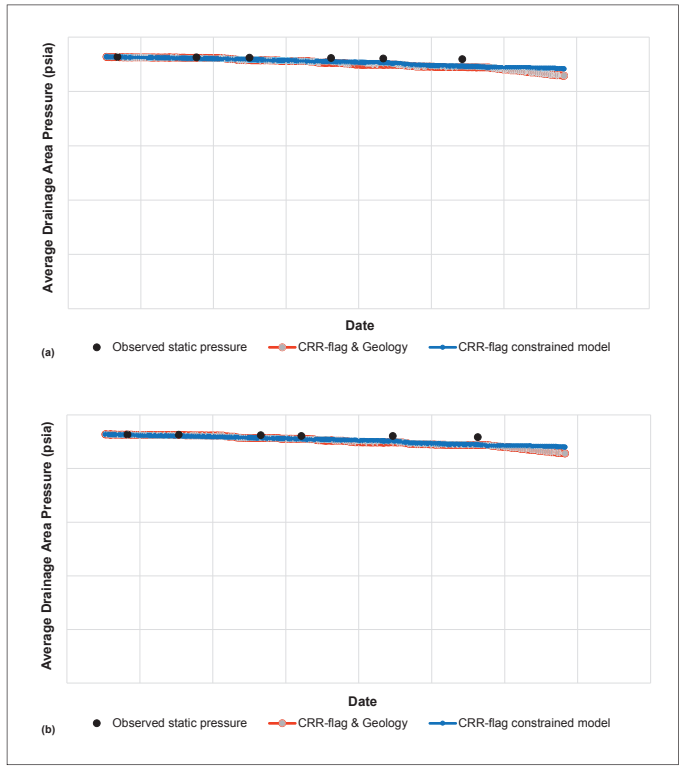

Fig. 14. Geology information in addition to the CRR flag also provides an adequate match of dynamic data for Prod-A2 (a), and Prod-A3 (b).

with the CRR flag constrained geomodel, Fig. 13.

The geomodel with permeability distribution based on CRR map scenario-2 in which the creation of the map was constrained by additional geology information like channel width and orientation — from Fig. 7 — was also run in simulation. Figure 14 shows the quality of the match to the dynamic data compared to the CRR map scenario-1.

Figure 15 shows the pressure match comparison of the SGS model and scenarios 1 and 2 of the PCM model for all the wells. It can be seen that the PCM approach results in a geomodel that is better conditioned to the observed dynamic data. While significant time and effort would be required to history match the wells based on the SGS model, only limited fine-tuning would be required to history match the wells based on any of the PCM model scenarios.

CASE REVIEW

Figure 16 shows the observed drainage area pressure measurement from several wells in a carbonate reservoir, Res-Y, showing identifiable homogeneous groups within a global heterogeneous system. At least four distinct homogenous trends could be identified, Figs. 17a to 17d.

By using the SGS workflow, a heterogeneous permeability distribution was obtained, Fig. 18.

The deep-blue dots are CRR-1 wells, the green dots are CRR-2 wells, the light-blue dots are CRR-3 wells, and the yellow dots are the CRR-4 wells. Most of the field production has taken place in the CRR-1 wells, but unfortunately these wells

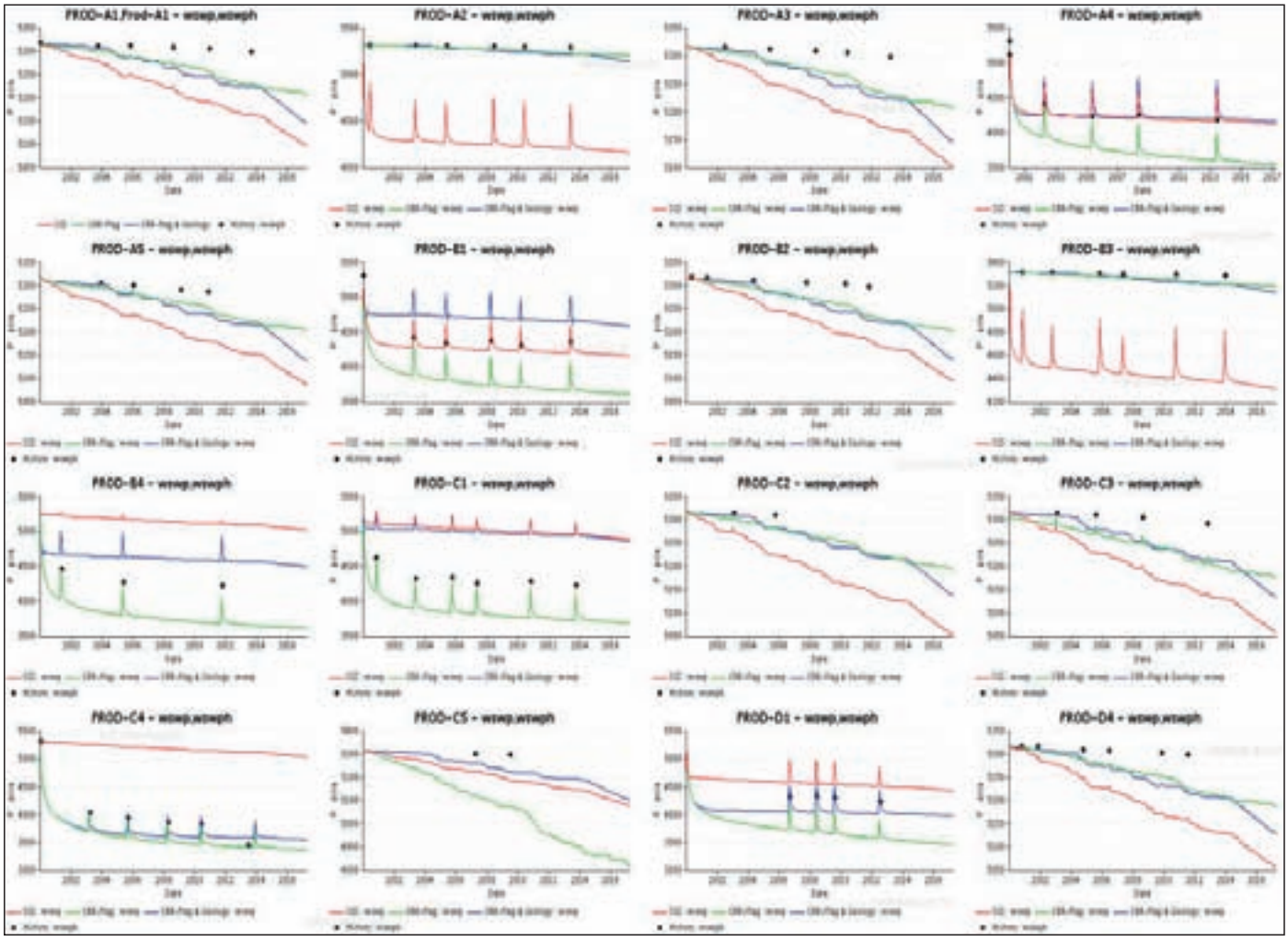

Fig. 15. Comparison of simulated pressure plots with observed pressure for the SGS and PCM geomodel scenarios.

are not cored. Therefore, the SGS approach has distributed predominantly low permeability into the CRR-1 region based on the low core permeability from nearby flankward wells.

It was also observed that the SGS workflow puts some CRR-1 wells in good permeability while others are placed in poor permeability. This is not consistent with the pressure data in Fig. 17a, which suggests that these wells are all within a single homogenous and hydraulically connected region. The same observation is also applicable to the wells shown in Fig. 17b.

Fig. 16. Time-lapse shut-in pressures for several wells in a carbonate reservoir, Res-Y, showing identifiable homogeneous groups within a global heterogeneous system.

Subsequently, using the PCM workflow, a CRR map was used as a constraint in the geomodel permeability distribution, and the resulting permeability distribution is shown in Fig. 19. The highest permeability is concentrated in CRR-1 and CRR-3, which are in the reservoir crest, as permeability degrades toward CRR-4, which is at the flank — this is why their pressures are almost at initial levels due to poor connectivity with the actively producing crestal wells. It is also observed that the PCM workflow ensures a better homogeneity of permeability around the wells within each CRR.

SUMMARY OF WORKFLOW

The implication of this modeling workflow is that the reservoir engineer no longer waits at the end of the modeling chain for the delivery of the static model, rather the modeling chain now begins with the reservoir engineer who is the custodian of the time-lapse pressure data and who should carry out the analysis of pressure trends and define the wells to be included within each CRR, Fig. 20.

Fig. 17. Four homogeneous pressure groups: (a) CRR-1 wells, (b) CRR-2 wells, (c) CRR-3 wells, and (d) CRR-4 wells, extracted from the globally heterogeneous cloud of shut-in pressures in Res-Y.

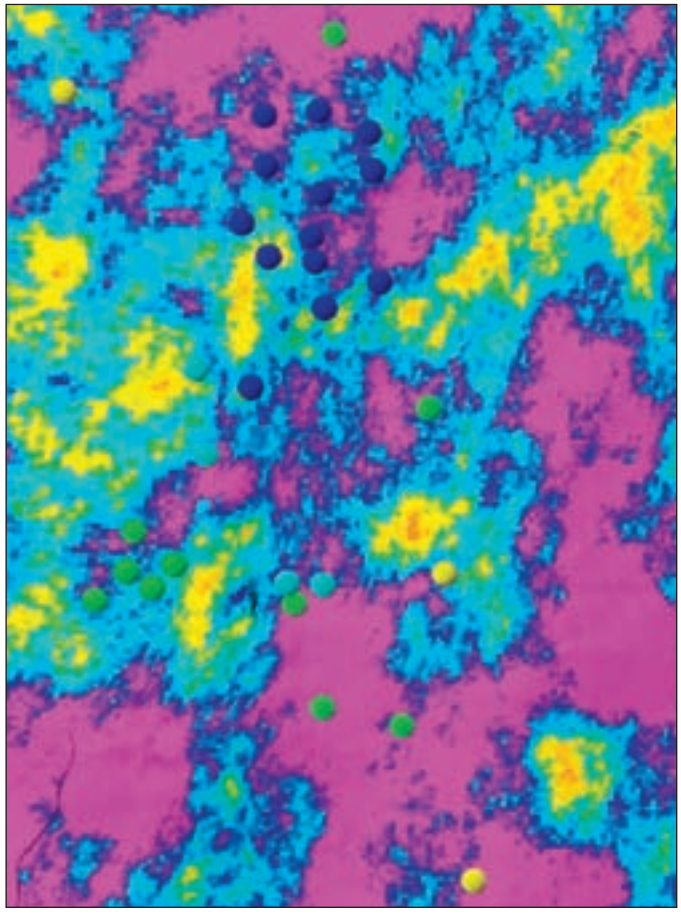

Fig. 18. Permeability model for Res-Y based on SGS modeling showing heterogeneous permeability distribution around the CRR-1 wells.

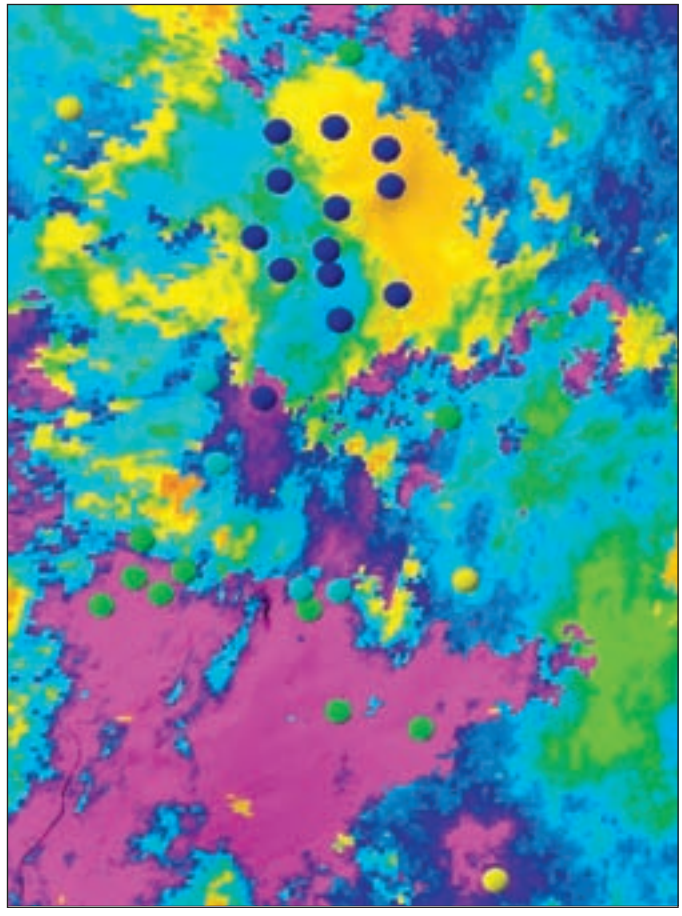

Fig. 19. Permeability model for Res-Y based on PCM showing good connectivity around the CRR-1 wells.

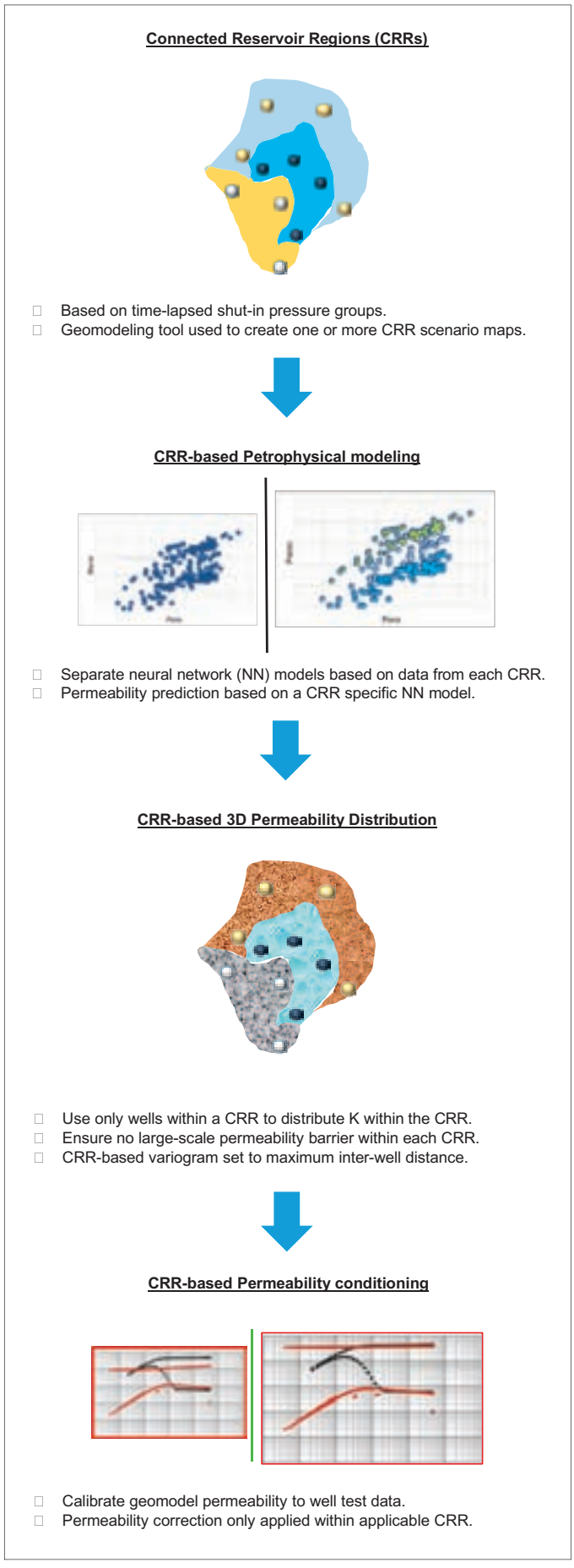

Fig. 20. Illustration of the PCM workflow.

CONCLUSIONS

Using time-lapse pressure data as a basis for determining CRRs and then using these CRR maps as variogram controls for core permeability distribution, leads to a geomodel that better represents reservoir dynamic behavior and could result in significant reduction in the time required for history matching.

ACKNOWLEDGMENTS

The authors would like to thank the management of Saudi Aramco for their support and permission to publish this article.

This article was presented at the SPE Kingdom of Saudi Arabia Annual Technical Symposium and Exhibition, Dammam, Saudi Arabia, April 23-26, 2018.

REFERENCES

1. Vaughan, R.D.: "Extending the Life of Brown Field Developments by Acoustic Impedance Conditioned 3D Reservoir Modeling: An Example from a Mature Gulf of Suez Carbonate Producing Asset (Ras Fanar Field), Egypt," IPTC paper 18126, presented at the International Petroleum Technology Conference, Kuala Lumpur, Malaysia, December 10-12, 2014.
2. Landa, J.L. and Horne, R.N.: "A Procedure to Integrate Well Test Data, Reservoir Performance History and 4D Seismic Information into a Reservoir Description," SPE paper 38653, presented at the SPE Annual Technical Conference and Exhibition, San Antonio, Texas, October 5-8, 1997.
3. Ceyhan, A.G.: "Generation of Porosity and Permeability Fields Conditioned to Geostatistical and Pressure Transient Data," SPE paper 52089, presented at the European Petroleum Conference, The Hague, the Netherlands, October 20-22, 1998.
4. Landa, J.L., Kamal, M.M., Jenkins, C.D. and Horne, R.N.: "Reservoir Characterization Constrained to Well Test Data: A Field Example," SPE paper 36511, presented at the SPE Annual Technical Conference and Exhibition, Denver, Colorado, October 6-9, 1996.
5. He, N., Oliver, D.S. and Reynolds, R.C.: "Conditioning Stochastic Reservoir Models to Well Test Data," SPE paper 38655, presented at the SPE Annual Technical Conference and Exhibition, San Antonio, Texas, October 5-8, 1997.
6. Bonet-Cunha, L., Oliver, D.S., Redner, R.A. and Reynolds, A.C.: "A Hybrid Markov Chain Monte Carlo Method for Generating Permeability Fields Conditioned to Multiwell Pressure Data and Prior Information," SPE paper 36566, presented at the SPE Annual Technical Conference and Exhibition, Denver, Colorado, October 6-9, 1996.
7. Reynolds, A.C., He, N., Chu, L. and Olivier, D.S.:

"Reparameterization Techniques for Generating Reservoir Descriptions Conditioned to Variograms and Well Test Pressure Data," SPE paper 30588, presented at the SPE Annual Technical Conference and Exhibition, Dallas, Texas, October 22-25, 1995.

8. Srinivasan, S. and Journel, A.G.: "Simulation of Permeability Field Conditioned to Well Test Data," SPE paper 49289, presented at the SPE Annual Technical Conference and Exhibition, New Orleans, Louisiana, September 27-30, 1998.
9. Alabert, F.G.: "Constraining Description of Randomly Heterogeneous Reservoirs to Pressure Test Data: A Monte Carlo Study," SPE paper 19600, presented at the SPE Annual Technical Conference and Exhibition, San Antonio, Texas, October 8-11, 1989.
10. Dake, L.P.: *Fundamentals of Reservoir Engineering, Volume 8 of Developments in Petroleum Science*, Amsterdam, Elsevier Science B.V., 1998, 462 p.

BIOGRAPHIES

Babatope O. Kayode joined Saudi Aramco in November 2014 as a Petroleum Engineer working with the Integrated Reservoir Studies Group in Saudi Aramco's Reservoir Description & Simulation Department.

His previous work experience with SOWSCO Well Services Nigeria Ltd. involved the planning, supervision, and analyses of pressure transient tests. Babatope also worked with Total Exploration and Production in Nigeria and in France, where he was involved in the construction and live updates of dynamic simulation models. Babatope has also worked extensively on fields in Africa and in Europe. He has 18 years of experience in the oil industry, and his research interest is in the area of developing workflows for faster and better history matching.

Babatope received his B.S. degree in Petroleum Engineering from the University of Ibadan, Oyo, Nigeria, and he is currently pursuing a master's degree in Petroleum Engineering at Heriot-Watt University, Edinburgh, U.K.

Mohammed A. Al-Saleh joined Saudi Aramco as a Field Geologist in 2007. He is currently the Team Leader of the Gas Modeling Unit within the Southern Area Reservoir Characterization Department. Mohammed has over 10 years of experience with Saudi Aramco, having been exposed to many different aspects of geology in the oil industry. His experience includes work in the Operations, Geosteering, and Wellsite divisions. Also, Mohammed has contributed to many studies in building sedimentary and structural, and integrated geological simulation models.

In 2007, he received his B.S. degree in Geology from King Fahd University of Petroleum and Minerals (KFUPM), Dhahran, Saudi Arabia.

Stig Lyngra works in Saudi Aramco's Southern Area Reservoir Management Department as a Senior Petroleum Engineering Consultant. Before joining Saudi Aramco in 2001, he worked for Danop in Copenhagen, Denmark, where he was Petroleum Engineering Discipline Leader. For the first 10 years of his career, Stig worked for Conoco as a Reservoir Engineer, a Supervising Reservoir Engineer, and a Commercial Coordinator, and he held different joint asset management positions in various offices in the U.S., Norway, and the U.K.

He is a member of the European Association of Geoscientists and Engineers (EAGE), the Society of Petroleum Engineers (SPE), and the Saudi Council of Engineers.

In 1987, he received his M.S. degree in Petroleum Engineering from the Norwegian Institute of Technology (NTH) in Trondheim, Norway. Stig also holds a degree in Business Administration from BI Norwegian Business School, Oslo, Norway.

Dr. Zeid M. Al-Ghareeb is a Petroleum Engineering Specialist working in Saudi Aramco's Reservoir Description and Simulation Department. He is currently leading the Event Solution Center for Integrated Reservoir Studies.

Zeid was the recipient of the Saudi Aramco Excellence Award in 2014. In addition, he was awarded a seed fund grant of $150,000 from MIT Energy Initiative (MITEI) in recognition of his doctoral research. Zeid is also the recipient of the 2014 Shoji Award for research and innovation at MIT.

He received his B.S. degree in Petroleum Engineering from the University of Tulsa, Tulsa, OK, an M.S. degree in Petroleum Engineering from Stanford University, Stanford, CA, and a Ph.D. degree in Computational Science for Energy Resources Engineering from Massachusetts Institute of Technology (MIT), Cambridge, MA.

Systematic Approach to Develop Colloidal Silica-based Gel System for Water Shut Off

Dr. Jin Huang, Dr. Ayman M. Al-Mohsin, Dr. Mohammed A. Bataweel, Prasad B. Karadkar, Dr. Wengang Li, and Abrar A. Alshaikh

ABSTRACT

Undesirable water production can significantly affect the economic life of producing wells. Excess water production results in loss of productivity, corrosion, and scaling. Also, the need for water handling facilities and reinjection of unwanted water can further add to the total cost of the project, which consequently increases the cost of production. In offshore operations, produced water can have an adverse impact on the environment.

The use of a colloidal silica (CS) based fluid system was developed for a water shut off application. A systematic experimental study was conducted to evaluate the effect of key parameters on the gelation properties of this system; that is: particle size, pH, temperature, and silica concentration. Also, the effect of different salts, as an activator agent, were tested to initiate in situ gelation of the CS. The performance of this system was evaluated by conducting static gelation tests as well as high-pressure, high temperature (HPHT) viscosity measurements up to 150 °C.

CS solutions exhibit low viscosity. Proper selection of a suitable activator can lead to the in situ gelation and formation of a high viscous gel to block the pore space. The permanent sealing of formation porosity can be achieved by building viscosity of the CS. The CS gelation time can be tailored by varying the activator type and concentration to match the field operation requirements. Kinetics of CS gelation at elevated temperatures showed quicker viscosity build up. The gelation time can be varied by controlling the initial pH of the system. A stable system and good dispersion was achieved for the CS solution without using an activator, as confirmed from the zeta potential value results. Increasing the salt concentration and temperature or lowering the pH of the system results in an unstable system that triggers the gelation process. The existence of more than one of the above factors, i.e., salt, temperature, and lower pH, results in a further reduction in gelation time.

CS has a low viscosity and can penetrate deeper into the formation matrix before transforming into a gel. The fluid system presented in this article was developed to address the needs of water shut off applications. The environmentally friendly system is comprised of two components, the CS and an activator.

INTRODUCTION

Excessive water production presents a major issue for field operations and the environment when it is discharged. Water production is either separated downhole and injected into a different formation, or brought together with oil to the surface for separation. Water production can limit the economic life of the oil and gas wells and can cause severe problems, including corrosion of the tubulars, fine migration, and hydrostatic loading. In addition, operational expenses, including lifting, separation, pumping, and reinjection, further add to the overall cost of the oil production. In 2002, produced water was estimated to cost the oil field industry approximately $50 billion per year[1].

One of the common reservoir problems is due to reservoir heterogeneities that can cause high permeability streaks[2]. These streaks include open fracture or fracture-like features. Reservoir heterogeneity is the most common reason for low hydrocarbon recovery and early water production[3].

Excessive water production can be reduced by recompleting the well or by placing mechanical devices to isolate the water formation zone. Yet, these solutions are expensive[4]. Chemical methods for conformance problems often represent a valid and cost-effective solution compared to mechanical isolation. Conventionally, in situ bulk gels have been used as a conformance control agent; however, a newer trend has been developed — particle gels — because they can overcome the problems associated with in situ gel systems, e.g., chromatographic separation of the gelant solution, and dilution and dispersion of the gelant, etc.[3, 5-7]. Several researchers proposed particle technologies that can be implemented to homogenize the reservoir and control excessive water production. These technologies include: preformed sized particle gels[8, 9], pH sensitive gels[10, 11], bright water[12, 13], and microgel and sub-microgels[14].

Recently, nanotechnology has gained great attention in the oil and gas industry for their potential applications. Nanotechnology offers the capability to enhance the industry when it comes to energy supply, via presenting technologies that are more effective, and more environmental friendly[15]. Several materials, devices, and tools with abilities that cannot be accorded by conventional methods can be urbanized using nanotechnology. Nanotechnology is well poised to dramatically influence all sectors of the industry[16]. For instance, in oil and

gas industry applications, nanotechnology could be used for the development of new resources by enhancing thermal conductivity and improving downhole separations[17].

Another emerging application of nanotechnology in the oil and gas industry includes the development of new types of smart fluids for improving oil recovery and drilling operations[18]. Such smart fluids will further enhance the rock properties by adding benefits such as wettability alteration, and advanced drag reduction[19]. Hendraningrat et al. (2010)[20] reported that nanosilica could significantly increase oil recovery by modifying surface tension. Shah (2009)[21] found that the viscosity of carbon dioxide (CO_2) mixed with 1% copper oxide nanoparticles and a small amount of dispersant is 140 times greater than the conventional CO_2. Almohsin et al. (2014)[22] used a nano gel-based polymer to study the transport properties of these nanoparticles through Berea sandstone cores. Moradi et al. (2015)[15] reported that the adsorption of silicon dioxide (SiO_2) nanoparticles with a size of 11 nm on the rock surface, altered the wettability of the rock from oil-wet to strongly water-wet; therefore, an incremental increase in the oil recovery of 20% was observed.

A previous study[23] used nanosilica and an activator chelating agent as a water sealant material where they investigated the effect of the activator concentration on gelation time. It was found that as the concentration of the activator increased from 2.5% to 7.5%, the gelation time decreased from 8 hours to 6 hours, respectively. Zeta potential are values, which can be used as an indicator of the stability of nanoparticles in a solution. Vryzas et al. (2015)[24] measured the zeta potential values at different concentrations (0.1% to 0.5%) and temperatures (78 °F and 100 °F) of iron oxide (Fe_2O_3) and silica nanoparticles, respectively. It was shown that Fe_2O_3 nanoparticles were stable in the colloidal suspension, however, SiO_2 nanoparticles were unstable under both temperatures.

Having a nanometric particle size (3 nm to 100 nm) and a low viscosity (usually < 10 centipoise (cP)), the nanosilica fluid could easily penetrate the pore matrix of the formation that is producing unwanted water, where they undergo physical transformation from a solids-free squeezable liquid to a highly viscous or rigid material that plugs the water zone.

The fluid system presented in this article is comprised of two components: modified nanosilica particles and an activator. Notably, it is easy to pump as a single phase, low viscosity solution, and upon placing it into the targeted zones the gelation process is activated/triggered by the formation temperature and time. By varying the concentration and the type of the activator, the gelation could be delayed to allow sufficient working time for placement operation. An experimental study was conducted to examine the effect of colloidal silica (CS) particle size, pH, temperature, particle concentration and different activator particles on gelation time. Zeta potential values were used as a tool in predicting the stability of the colloidal nanosilica fluid system.

Gelation Mechanism of a Nanosilica-based System

The majority of commercial CS species are anionic species. The silica nanoparticles carry a negative surface charge, and are stabilized in an alkaline pH solution in which the repulsion forces between the same charged particles prevents them from colliding with each other. Therefore, the initial colloidal system is stable and usually has a high negative zeta potential value as it directly measures the particle-particle repulsion forces in a colloidal suspension.

In the application of a colloidal nanosilica-based gel system for water shut off, it is expected that the gelation process starts once the colloidal system is destabilized from the initial state. To trigger the gelation, one way is to reduce the repulsion forces between negative charged silica nanoparticles by introducing the counter ions — cationic species. The addition of counter ions directly lowers the zeta potential value of the system. Consequently, the colloidal nanosilica system becomes unstable and the gelation process is initiated. At the first stage of gelation, the nanoparticles tend to just come into contact due to the reduction of repulsion, but there are no covalent bonds formed, and therefore, the system shows low viscosity. As the process continues, the interacting particles adhere to each other through the formation of covalent bonds leading to the formation of extended networks represented as aggregates and agglomerates. The system shows increased viscosity as more particles are linked together and the chemical bonds are stronger. At the third stage of gelation, the nanosilica gel is formed, but the strengthening of the gel is still ongoing, although the flowability of the system is totally lost. This final stage could be very slow when the temperature is low.

EXPERIMENTAL STUDIES

In this section, the equipment and chemicals that were used in this work is presented and measurement modes used are also briefly explained.

Materials

The nanofluid is comprised of colloidal nanosilica and an activator. General inorganic chlorides and salts such as sodium chloride (NaCl), potassium chloride (KCl), ammonium chloride (NH_4Cl), calcium chloride ($CaCl_2$), sodium nitrate ($NaNO_3$), and sodium sulfate (Na_2SO_4), were used as activating agents. Five commercial grades of modified CS were investigated in this work. All of them are alkaline, aqueous dispersions of silica nanoparticles with approximately 15 wt% to 40 wt% of silica content. The stabilized amorphous silica nanoparticles carry a negative surface charge. Table 1 lists the typical properties of these products.

	CS1	CS2	CS3	CS4	CS5
SiO_2 (wt%)	40%	30%	15%	15%	15%
pH	~9.5	~10.1	~10	~10.5	~9.5
Viscosity (cP)	< 15	< 10	< 5	< 20	< 5
Average Particle Size (nm)	17	7	5	3	5

Table 1. Typical properties of the five commercial grades of modified CS at 25 °C

Methodology

A systematic approach in this work was conducted to evaluate the nanofluid as follows.

Zeta Potential Value. The zeta potential value is an index of the magnitude of interactions between the colloidal particles, and so is an important indication of the fluid system's stability. The zeta potential value measurement gives us an understanding of colloidal system stability. This can be correlated to the gelation time, since gelation is triggered by destabilizing the colloidal system and further progressed by other chemical processes as previously explained. A typical range for zeta potential values is from -100 mV to +100 mV. Particles with zeta potential values more positive than +30 mV or more negative than -30 mV are normally considered stable.

Proper sample preparation is very critical in this type of measurements, due to its high sensitivity to several factors. In our tests, we first diluted the solutions to 3% SiO_2 to avoid concentrations that were too high, which may give poor quality results. Then, we loaded the testing cell with the chemical before exposing it to ultrasonic waves for 1 minute to ensure proper dispersion of the particles right before starting the test. After that, we prepared samples for the study of temperature effect on the zeta potential. We performed the zeta potential evaluation for each chemical at four different temperatures: 25 °C (77 °F), 38 °C (100.4 °F), 65 °C (149 °F), and 90 °C (194 °F), which is the maximum temperature of the instrument.

Next, for the salt concentration experiment, we tested the zeta potential of C36 at different NaCl concentrations: 0.05%, 0.10%, 0.15%, 0.20%, and 0.30%. The last experiment was studying the effect of pH on zeta potential, and so, we tested the zeta potential of CS2, which had an original pH of 10.2, at pH values of 8, 6, 4, and 2, by adding hydrochloric (HCl) acid, and at a pH of 12, by adding sodium hydroxide (NaOH).

Static Gelation (Test Tube) Method. In this study, we employed the test tube method to visually observe the gelation process and roughly estimate the gelation time under static conditions. Here we define the gelation time to be the initial gelling point in which the CS fluid's viscosity significantly increases. In this experiment, a glass test tube was filled with a fluid sample with a specified volume. The test tube was then placed at room temperature or in a preheated oven set at the testing temperature, and periodically taken out for observation. The gelation time was determined when the test tube could be turned upside down without any movement of the gel, meaning the flowability of the fluid is totally lost.

The test tube method could be a very useful tool for "screening" purposes when developing formulation for specific applications. Gelation time measurements were performed using this method for testing temperatures at 25 °C, 60 °C, and 80 °C.

Viscosity Method. The viscosity method allows us to gain more precise information about the gelation time and gelation behavior of the CS nanofluid under high-pressure, high temperature (HPHT). By using a rheometer, the fluid viscosity changes were monitored as a function of time at a given constant shear rate. Gelation time is the time required to begin a sharp change in viscosity, and this can be determined from the viscosity profile obtained. A rotational viscometer with standard coaxial cylinder geometry was used.

Viscosity tests were carried out at a constant shear rate of $10s^{-1}$ under 500 psi of nitrogen pressure applied to the system at a preset testing temperature range — 25 °C to 150 °C. A freshly prepared colloidal nanosilica fluid was placed in the cup and affixed to the rotor fixture on the rheometer.

	CS1	CS2	CS3	CS4	CS5
SiO_2 (wt%)	3	3	3	3	3
pH	9.9	10.5	10.5	10.9	10.2
Particle Size (nm)*	9 and 43	5	9	9	2 and 14
Zeta Potential ξ (mV)	-49.7	-45.9	-55.8	-32.0	-39.5

Table 2. The zeta potential value and size measurements on the five CS samples at 25 °C
* The samples with two numbers indicate the peaks in the particle size distribution curves.

RESULTS AND DISCUSSION

Zeta Potential Value

Size Measurements. Measurements of pH, particle size distribution and zeta potential at 25 °C were performed on all five CS products. To avoid obtaining poor quality data associated with high concentrations and also for good comparison, the CS samples were diluted to the same silica content of 3 wt% before the measurement. Proper sample preparation techniques, such as an ultrasonic bath, were used to ensure better sample dispersion and homogeneity for the particle size and zeta potential measurements. Table 2 lists the results of the five CS samples used.

The diluted CS samples show a pH from 9.9 to 10.9. All measured zeta potential values are more negative than -30 mV, indicating the colloidal nanoparticles are stabilized in an alkaline solution. The particle size measurement data shown in Table 2 suggests that most of the CS samples have a particle size value slightly higher, but are still close to that reported in their product data sheet. The slight increase in the samples' particle size can be attributed to aggregation or agglomeration of the particles during storage. It should be noted that unlike other CS, which shows a narrow particle size distribution, CS1 provides a broad particle size distribution exhibiting two separate nodes at ~9 nm and ~43 nm. This can be due to the fact CS1 — from Table 1 — has the highest SiO_2 content at 40%, and biggest average particle size, ~17 nm.

Temperature Effect on the Zeta Potential Value. The zeta potential value was measured for five CS species at 3% SiO_2 at four different temperatures, Fig. 1. Overall, it can be seen that as the temperature increases, the stability decreases until the solution gets to the point of least stability or as it is called, the isoelectric point, where the zeta potential value is zero in value. This happens around a temperature of 55 °C for almost all of the samples. After this point, we observe that the zeta potential value increases slightly before dropping once again. At temperatures closer to 90 °C, we reach the instrument's maximum limit

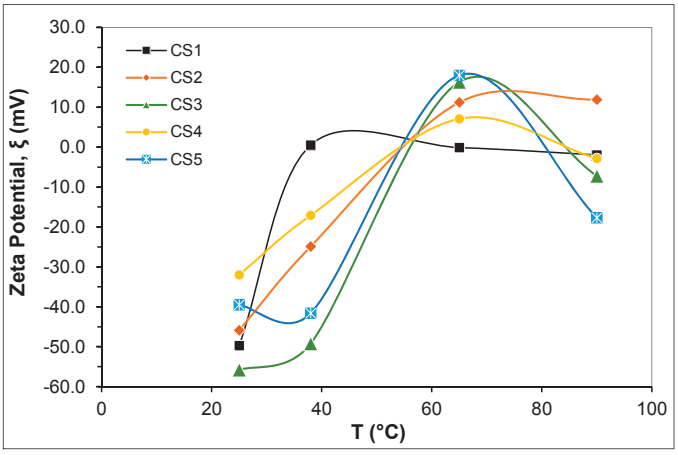

Fig. 1. Temperature effect at four different temperatures on the zeta potential value of the five CS species at 3% SiO_2.

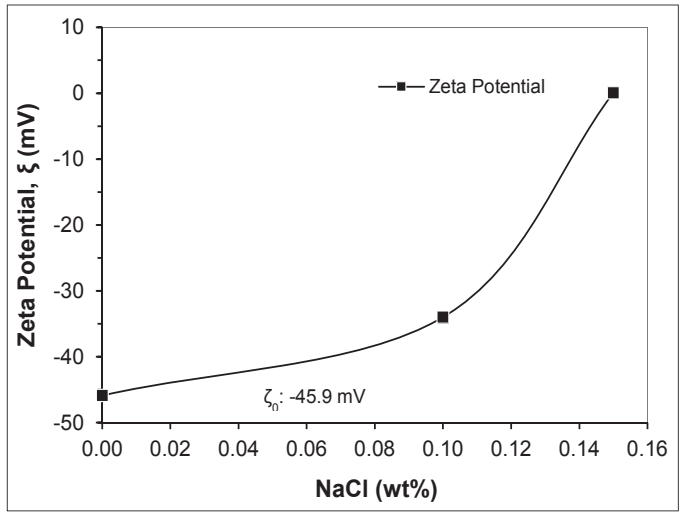

Fig. 2. Salt concentration effect on the zeta potential of CS2 at 3% SiO_2 and 25 °C.

and the results are of poor quality, which makes the interpretation of the result at high temperature meaningless.

Salt Concentration Effect on the Zeta Potential Value. The zeta potential value of the CS2 sample diluted to 3% of silica content with three different NaCl concentrations: 0.1%, 0.15%, and 0.3%, was determined. Figure 2 shows an overall decrease in the zeta potential magnitude as more salt was added. This can be justified with the Na^+ ions neutralizing the negative charge at the surface of the CS particles; thereby decreasing the potential at the boundary of the double layer, consequently decreasing the stability of the colloidal suspension of the system. It should be noted that no zeta potential data was reported with a NaCl concentration of 0.3% because of high sample conductivity, as the sample conductivity exceeded the instrument's limit and the data was not valid.

pH Effect on the Zeta Potential Value. In aqueous media, the pH of the sample is one of the most important factors that affects its zeta potential value. Being dispersed in an aqueous solution, the CS nanoparticles can carry a net positive or negative charge, or be neutral, all depending on the pH of the solution. This can be explained by the adsorption/interaction between the nanoparticle surface silanol group, –Si–OH, and the H^+ or OH^- in the solution:

$$\text{–Si–OH} + OH^- \leftrightarrow \text{-Si-O}^- + H_2O \quad (1)$$

$$\text{–Si–OH} + H^+ \leftrightarrow \text{-Si-OH}_2^+ \quad (2)$$

When the solution's pH is high, the surface silanol group adsorbs OH^- and produces –Si-O^-, resulting in a negative surface charge, Eqn. 1. When the solution's pH is low, the surface silanol group adsorbs H^+ and produces -Si-OH_2^+, resulting in a net positive charge, Eqn. 2. If the solution is pH neutral, the nanoparticles have a surface silanol group –Si–OH and carry no net charge. Therefore, it is important to understand how

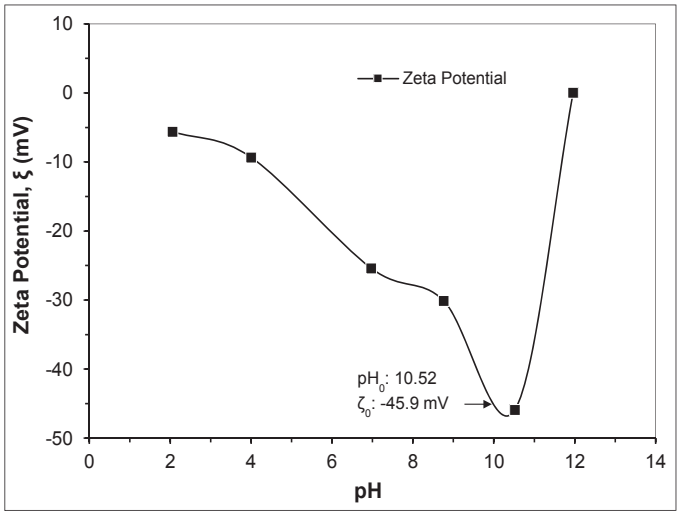

Fig. 3. The pH effect on the zeta potential of CS2 at 3% SiO_2 and 25 °C.

the pH will affect the zeta potential value of the CS nanoparticles. To study the pH zeta potential behavior, we tested sample CS2 at a 3 wt% nanosilica particle concentration. By adding HCl acid dropwise, we measured the change of the sample zeta potential value when the original pH sample was changed from 10.52 to 8.76, 6.97, 4.00, and 2.06. By adding NaOH dropwise, we measured the change of the sample's zeta potential value when the original sample's pH was increased from 10.52 to 11.96. Figure 3 shows the results of the pH effect on the zeta potential of CS2 at 3% SiO_2 and 25 °C.

The zeta potential value showed a steady decrease in value as we added more acid, meaning that the acid destabilized the colloidal system from -31.6 mV to -5.6 mV. This agrees with the expectations in theory; because the negative charges of the nanoparticle were neutralized by H^+ when acid is added, and the pH is reduced resulting in less stability. On the other hand, as we added more alkali, the zeta potential value also showed a decrease in the zeta potential value to the minimum of zero. Following the same logic, we would expect the stability of the colloidal system to increase as we add the OH^- to the negatively charged particles of the system. Consequently, the results show a decrease in stability instead, which can be due to the high concentration of ions, comprising the electrical double layer and destabilizing the colloidal system.

Gelation Time Study by Test Tube Method

Fig. 4. Picture of the test tube showing the gelled CS.

The gelation time was determined by visually observing the presence of flow in a test tube. Figure 4 shows the picture of CS-based fluid system after gelation. In tube tests with CS, CS1, and CS3 with an activator, NaCl was studied at three different temperatures — 25 °C, 60 °C, and 80 °C — by varying the activator's concentration, CS concentration and particle size to investigate the effect on the gelation time of the fluid system. Table 3 provides the test matrix and results of the tube tests.

Figure 5 is the graphical representation of gelation time vs. temperature of CS1 with NaCl as an activator. Some of the samples did not show gelation during the 24-hour observation period. The "no gelation" results are represented with a maximum scale of 2,000 minutes as gelation time.

Temperature	CS	Silica Content (%)	Gelation Time with Different Concentrations of NaCl			
			5%	2%	1%	0.5%
25 °C	CS1	40	Instantly	5 min	3 h	NG
		20	5 min	4.5 h	NG	NG
		15	15 min	13 h	NG	NG
	CS3	15	Instantly	30 min	20 h	NG
60 °C	CS1	40	Instantly	Instantly	30 min	7 h
		20	Instantly	1 h	16 h	NG
		15	3 min	2 h	23.5 h	NG
	CS3	15	Instantly	20 min	2 h	NG
80 °C	CS1	40	Instantly	Instantly	Instantly	3 h
		20	Instantly	15 min	4.5 h	NG
		15	Instantly	30 min	5.5 h	NG
	CS3	15	Instantly	Instantly	1 h	18 h

Table 3. Tube tests on gelation times of CS with NaCl as an activator
Note: NG — No gelation happened within the observation time window.

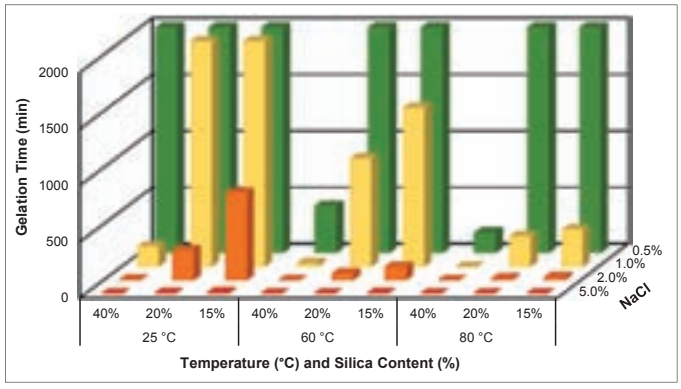

Fig. 5. A graphical representation of the results of the study of gelation time vs. temperature of CS1 with NaCl as an activator.

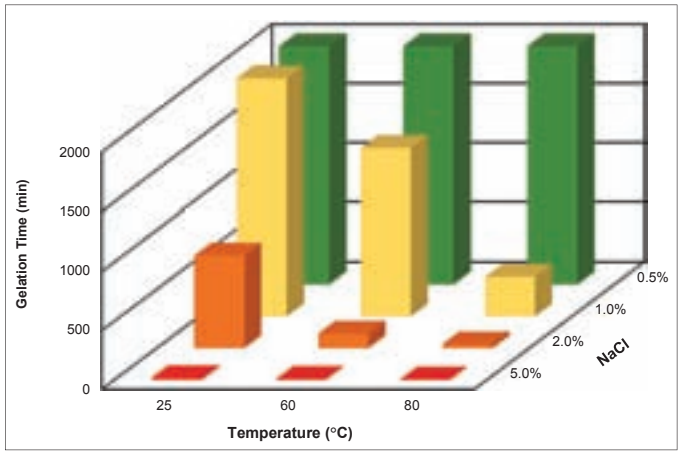

Fig. 6. Effect of temperature on gelation time with CS sample CS1 at 15% silica content, with varying activator concentrations.

Temperature Effect. As learned from the zeta potential value study, temperature has a significant impact on the gelation time of the colloidal nanosilica. The higher the temperature, the lower the zeta potential value of the system, therefore, the colloidal system becomes less stable and the gelation process is triggered. When analyzing the test tube results in Table 3, the gelation can be substantially reduced as temperature increases.

Figure 6 shows the effect of temperature on gelation time with CS sample CS1 having 15% silica content and varying activator concentrations. With 1% NaCl, at 25 °C, no gelation was seen, whereas at 60 °C the gelation time was decreased to 23.5 hours. At 80 °C, it further decreased to 5.5 hours. Similarly, with an increase in temperature, a reduction in gelation time was observed with 2% NaCl as an activator.

Silica and Salt Concentration Effect. One other factor of CS gelation is the silica, SiO_2 concentration. Figure 7 shows the effect of the silica and salt concentration on the gelation time with CS sample CS1 at 60 °C. At a certain temperature, the gelation time increases when the SiO_2 concentration decreases while the salt concentration is fixed. In this investigation, with 1% NaCl, the gelation time was decreased from 23.5 hours to 0.5 hours by increasing silica contact from 15% to 40%. It is obvious that the gelation time decreases when an activator concentration increases at a given temperature and fixed silica concentration. In the present study, with 20% silica content, instant gelation was seen when 5% NaCl was mixed with CS, while the gelation time was delayed to 1 hour by decreasing the NaCl concentration to 2%.

CS Particle Size Effect. It is interesting to note that when two different CS samples, with the same SiO_2 concentration, while other parameters such as temperature and salt concentration are kept constant, the particle size difference will cause a different gelation rate. This can be seen by comparing the data of CS1 with 15% SiO_2 and CS3 with 15% SiO_2, at different temperatures with a NaCl activator concentration of 2% and 1%.

Figure 8 shows the effect of the particle size on the gelation time of CS1 and CS3 at different conditions. CS1 has a larger silica particle size of ~43 nm, as compared to CS3 with a particle size of only 9 nm. At 60 °C, CS1 with 15% SiO_2 gelled after 23.5 hours with 1% NaCl, while CS3 with 15% SiO_2 gelled after 2 hours at the same activator concentration. This is probably due to the smaller particle size, which has a larger surface area and more active sites that contributes to the enhanced particle interaction, leading to a faster gelation. Similar gelation behavior was observed with a higher activator concentration of 2% NaCl.

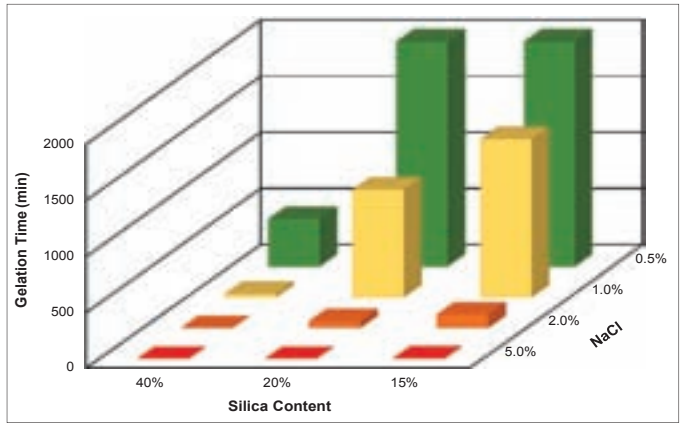

Fig. 7. Effect of the silica and salt concentration on the gelation time with CS sample CS1 at 60 °C.

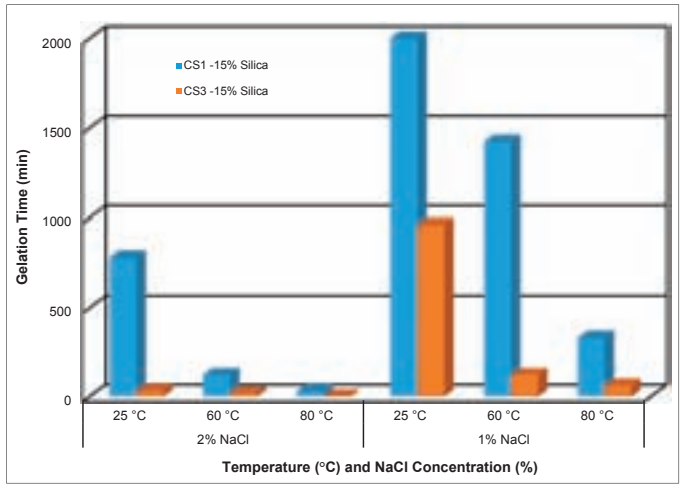

Fig. 8. Particle size effect on the gelation time of CS1 and CS3 with NaCl as an activator.

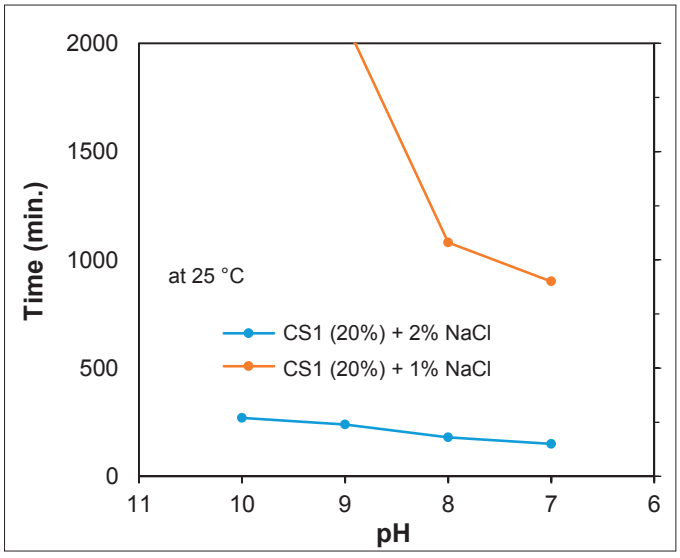

Fig. 9. The pH effect on gelation time of CS with NaCl.

pH Effect. Tube tests were also conducted to study the pH effect on gelation of the CS, Fig. 9. The test of CS1, with 20% SiO_2 + 2% NaCl was conducted to get a reasonable observation time. The original pH of this CS system is 10. Then, by adding acetic acid dropwise, the pH was lowered to 9, 8, and 7, respectively, and corresponding tube tests were carried out. From the results we see that when the pH goes lower, the gelation time was reduced. The same trend was observed for CS1 with 20% SiO_2 + 1% NaCl; however, we did not do tests in an acidic condition as CS suspension is unstable and tends to aggregate when the pH is lower than 7.

Cations Effect. Four different inorganic chlorides were studied to analyze the cation effect on the gelation of the CS sample, CS1. Table 4 summarizes the test matrix and the effect of cations on gelation times of CS1.

All the chlorides were tested at four Cl^- mole concentration levels, respectively. At the fixed Cl^- concentration level, the fluids with different cations were prepared to have the equal ionic strength for good comparison showing only the cations effect. All four inorganic chlorides can gel the CS at 25 °C. For a specific chloride salt, the gelation time decreases as the concentration of chloride salt increases. Alkaline CS nanoparticles carry a negative surface charge, and the adding of inorganic chlorides introduces cations of Na^+, K^+, NH_4^+, and Ca^{2+}, which acts as counter ions and will enter into the electrical double layer of the nanoparticles. This will lower the zeta potential value of the nanoparticle, and therefore, destabilize the colloidal system and cause the gelation.

As the salt concentration increases, this effect will be more obvious. Different cations affect the gelation time of CS in different degrees. Divalent Ca^{2+} reduces the gelation time more than others. All the tests of the four $CaCl_2$ loadings show the "instant" gelation, which differentiates Ca^{2+} from other monovalent cations. This is because cations with higher valence and a larger size, such as divalent Ca^{2+}, will more easily precipitate the surface SiO_3^{2-}, thereby decreasing the zeta potential value and promoting the gelation more easily. Also, high valent cations could react with OH^- forming insoluble spices, which consumes OH^- in the solution. The repulsive forces between OH^- and the same negatively charged silica nanoparticles, which help stabilize the colloidal system will be less. In other words, the nanoparticles have less "protection" and more chance to collide, meaning the gelation time will be shortened. Other observations with different monovalent cations have shown that larger cations, i.e., potassium (K), will have the capability to shorten the gelation time compared to Na.

CS	Silica Content (%)	Inorganic Chlorides	Cl^- Concentration (mol/L)			
			0.85	0.34	0.17	0.09
CS1	20	NaCl	5 min	4 h	> 24 h	> 24 h
CS1	20	KCl	Instantly	10 min	9 h	> 24 h
CS1	20	NH_4Cl	Instantly	15 min	5 h	> 24 h
CS1	20	$CaCl_2$	Instantly	Instantly	Instantly	Instantly

Table 4. The effect of cations on gelation times of CS1 at 25 °C

CS	Silica Content (%)	Inorganic Chlorides	Na^+ Concentration (mol/L)			
			0.85	0.34	0.17	0.09
CS1	40	NaCl	Instantly	5 min	3 h	> 24 h
CS1	40	$NaNO_3$	Instantly	10 min	4 h	> 24 h
CS1	40	Na_2SO_4	15 min	1.5 h	18 h	> 24 h
CS3	15	NaCl	Instantly	30 min	13 to 20 h	> 24 h
CS3	15	$NaNO_3$	1 min	1 h	> 24 h	> 24 h
CS3	15	Na_2SO_4	20 min	6 h	> 24 h	> 24 h

Table 5. The effect of anions on gelation times of CS1 and CS3 at 25 °C

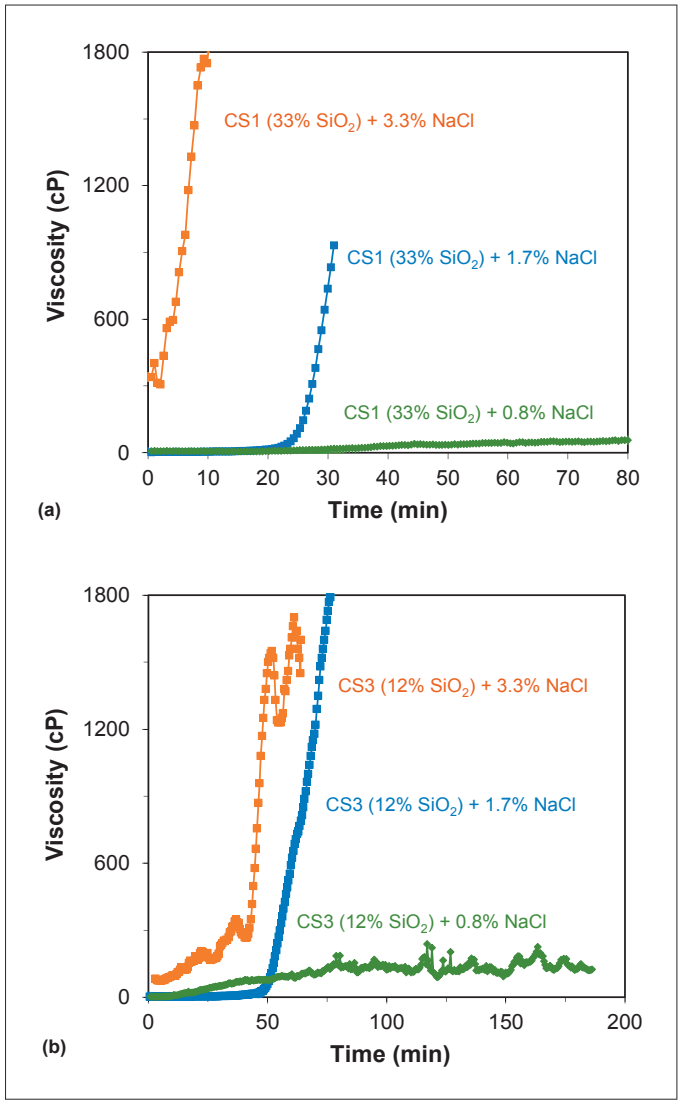

Fig. 10. The NaCl concentration effect on gelation time of CS1 (a), and CS3 (b) at 25 °C.

Anions Effect. The effect of anions on the CS gelation process were studied in a similar way. Table 5 shows the test matrix and the results of the tube tests concerning the effect of anions on gelation times of CS1 and CS3. Three inorganic sodium salts, NaCl, $NaNO_3$, and Na_2SO_4, were selected for the tests at four different Na^+ mole concentrations. At the same Na^+ concentration, the fluids have equal ionic strength. The tests were performed on two CS samples at 25 °C. All three inorganic Na salts cause the gelation of the CS. For a specific sodium salt, the gelation time increases as the concentration of Na salt decreases. This observation is the same as shown in the cations' effect study as the adding of salts in general will change the zeta potential value of the nanoparticle and affect the colloidal system stability.

The gelation time has a positive correlation with salt concentration. It seems that different anions affect the gelation time of the colloidal fluid in different degrees. By comparing the gelation time test results of CS1 and CS3, it suggested that Cl^- and NO_3^- affect the gelation time of CS in the same scale; however, SO_4^{2-} has a bigger impact on affecting the gelation time. As can be seen in Table 5, when using Na_2SO_4, the gelation time was decreased significantly by increasing the concentration of Na salt compared to the other two. This could be explained that although anions such as Cl^-, NO_3^-, and SO_4^{2-} play the same role to stabilize the colloidal nanoparticles due to the same negative charge repulsion, but divalent SO_4^{2-} has a larger size and functions more effectively.

Gelation Time Study by Viscosity Method

Gelation time of the CS fluid system was also measured using a rheometer to simulate bottom-hole HPHT conditions. CS samples CS1 and CS3 were studied with NaCl as an activator up to 150 °C.

Salt Concentration Effect. Figures 10a and 10b show that the change in activator, NaCl concentration, greatly affects the gelation time. As can be seen from Fig. 10a, for CS1 — at 25 °C — with 33% SiO_2, as the NaCl concentration decreased from 3.3% to 1.7% and 0.8%, the gelation time increased from ~5 minutes to 25 minutes and > 80 minutes, respectively. Figure 10b shows a similar behavior that was observed for CS3. These results again confirm our findings by using the zeta potential value study and tube tests.

Temperature Effect. The effect of temperature on the gelation time has been investigated using rheometer tests. Figure 11 shows the gelation behavior for CS3 at two different temperatures. We observed the delayed gelation at 25 °C, while at 60 °C, the gelation rate rapidly increased.

High Temperature Study on Gelation Time. The main objective of this work was to develop a colloidal nanosilica-based fluid system for high temperature water shut off applications. As previously discussed, the temperature is found to be the key factor affecting the gelation time of the CS. In analyzing the

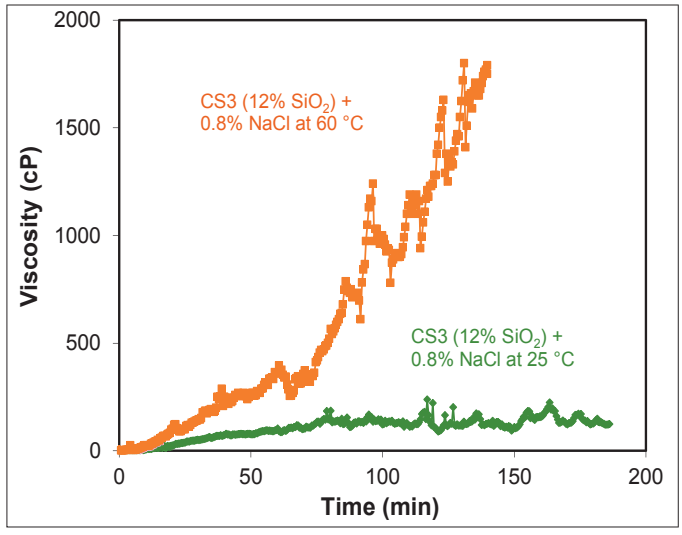

Fig. 11. Temperature effect on the gelation time of CS3 with NaCl.

CS	Silica Content (%)	NaCl				Temperature
		5%	2%	1%	0.5%	
CS3	15	Instantly	0.5 h	16 h	> 24 h	25 °C
CS3	15	Instantly	Instantly	1 h	18 h	80 °C

Table 6. Sensitivity of CS with small variations of NaCl concentrations (derived from Table 3)

test tube results, it was noticed that in one case, upon increasing the temperature by 55 °C (25 °C to 80 °C) the gelation time was reduced approximately 15 times. Another important factor affecting the gelation rate of the CS is an activator concentration. Colloidal nanosilica showed that it is very sensitive to small variations to salt concentration at given temperatures. This can be seen from Table 6 (derived from Table 3).

For example, at 25 °C, for CS3 (15% SiO_2), while decreasing the NaCl concentration from 2% to 1%, the gelation time increased from 0.5 hour to 16 hours, showing the sensitivity of the CS to salt concentration. At elevated temperatures, it was observed that this sensitivity was magnified.

For high temperature water shut off, the sensitivity can be an issue since the Na concentration is difficult to be controlled at reservoir conditions, based on the contaminations from rocks or groundwater. To meet the high temperature (> 120 °C) water shut off materials requirement and also study this sensitivity phenomenon, rheometer tests on CS3 was performed with NaCl as an activator at 150 °C. The preliminary results are shown in Fig. 12.

At high temperatures, i.e., 150 °C, the CS system is very sensitive, even a very small variation of NaCl concentration — 0.1% — could make a significant difference in gelation time. When mixing fluid formulations in the field, more attention should be provided while adding an activator. Based on the rheology study, it is advised to search for alternative activators, which will provide better control of the gelation time.

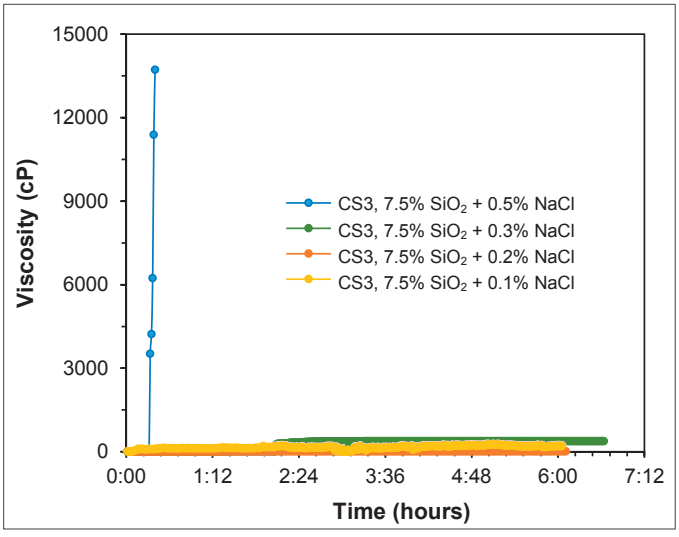

Fig. 12. Gelation time study on CS3 with NaCl at 150 °C.

CONCLUSIONS

A CS-based fluid system was investigated for use in a high temperature water shut off application. Low viscosity of the CS-based fluid system can assist in depth penetration to maximize treatment coverage. The fluid system investigated in this article is composed of simply two components, CS, and a salt as an activator. Based on the experimental work, the following conclusions were drawn:

- The zeta potential value is used as a tool to predict conditions that can destabilize the colloidal suspension and trigger the gelation process in this system.
- Values of zeta potential are affected by the temperature, Na concentration and pH. Increasing the temperature and Na concentration and reducing the pH results in reduction of the zeta potential value, rendering the system unstable.
- Static test tube methods can be used as a screening tool to estimate the gelation time, while the viscosity method will provide more accurate information about the gelation behavior of the system.
- The temperature plays a key role in determining the gelation time of the system. High temperature substantially speeds up the gelation. The pH alternation of the fluid system affects the gelation time.
- A higher activator concentration accelerates the gelation at a fixed temperature and silica concentration, and the gelation time will decrease when the Na concentration increases.
- Different cations or anions in the activator impact the gelation differently, which is mainly dependent on the charge density and size of the ion species.
- Silica content and the particle size also influence the gelation time. A shorter gelation time was measured when increasing the particle's concentration in the solution with smaller particle sizes.
- The study has shown that the gelation time of the CS fluid system is sensitive to small variations of Na concentration. This sensitivity was magnified at elevated temperatures. At 150 °C, even a change of the NaCl concentration in 0.1% increments will make a significant difference in gelation time.

ACKNOWLEDGMENTS

The authors would like to thank the management of Saudi Aramco for their support and permission to publish this article. The authors would also like to acknowledge the efforts of Ahmad Busaleh and Ali Hussain for helping with the experimental work.

This article was presented at the SPE Middle East Oil and Gas Show and Conference, Manama, Kingdom of Bahrain, March 6-9, 2017.

REFERENCES

1. Hill, F.L., Monroe, S. and Mohanan, R.: "Water Management — An Increasing Trend in the Oil and Gas Industry," SPE paper 154720, presented at the SPE/EAGE European Unconventional Resources Conference and Exhibition, Vienna, Austria, March 20-22, 2012.
2. Thomas, F.B., Bennion, D.B., Anderson, G.E., Meldrum, B., et al.: "Water Shut Off Treatments — Reduce Water and Accelerate Oil Production," *Journal of Canadian Petroleum Technology*, Vol. 39, Issue 4, April 2000, pp. 25-29.
3. Bai, B., Li, L., Liu, Y., Liu, H., et al.: "Preformed Particle Gel for Conformance Control: Factors Affecting Its Properties and Applications," *SPE Reservoir Evaluation & Engineering*, Vol. 10, Issue 4, August 2007, pp. 415-422.
4. Mennella, A., Chiappa, L., Lockhart, T.P. and Burrafato, G.: "Candidate and Chemical Selection Guidelines for Relative Permeability Modification (RPM) Treatments," *SPE Production & Facilities*, Vol. 16, Issue 3, August 2001, pp. 181-188.
5. Coste, J-P., Liu, Y., Bai, B., Li, Y., et al.: "In-Depth Fluid Diversion by Pre-Gelled Particles: Laboratory Study and Pilot Testing," SPE paper 59362, presented at the SPE/DOE Improved Oil Recovery Symposium, Tulsa, Oklahoma, April 3-5, 2000.
6. Chauveteau, G., Omari, A., Tabary, R., Renard, M., et al.: "New Size Controlled Microgels for Oil Production," SPE paper 64988, presented at the SPE International Symposium on Oil Field Chemistry, Houston, Texas, February 13-16, 2001.
7. Chauveteau, G., Tabary, R., Le Bon, C., Renard, M., et al.: "In-Depth Permeability Control by Adsorption of Soft Size Controlled Microgels," SPE paper 82228, presented at the SPE European Formation Damage Conference, The Hague, the Netherlands, May 13-14, 2003.
8. Bai, B., Liu, Y., Coste, J-P. and Li, L.: "Preformed Particle Gel for Conformance Control: Transport Mechanism Through Porous Media," SPE paper 89468, presented at the SPE/DOE Symposium on Improved Oil Recovery, Tulsa, Oklahoma, April 17-21, 2004.
9. Bai, B., Wei, M. and Liu, Y.: "Field and Lab Experience with a Successful Preformed Particle Gel Conformance Control Technology," SPE paper 164511, presented at the SPE Production and Operations Symposium, Oklahoma City, Oklahoma, March 23-26, 2013.
10. Al-Anazi, H.A. and Sharma, M.M.: "Use of a pH Sensitive Polymer for Conformance Control," SPE paper 73782, presented at the International Symposium and Exhibition on Formation Damage Control, Lafayette, Louisiana, February 20-21, 2002.
11. Huh, C., Choi, S.K. and Sharma, M.M.: "A Rheological Model for pH Sensitive Ionic Polymer Solutions for Optimal Mobility Control Applications," SPE paper 96914, presented at the SPE Annual Technical Conference and Exhibition, Dallas, Texas, October 9-12, 2005.
12. Pritchett, J., Frampton, H., Brinkman, J., Cheung, S., et al.: "Field Application of a New in-Depth Waterflood Conformance Improvement Tool," SPE paper 84897, presented at the SPE International Improved Oil Recovery Conference in Asia Pacific, Kuala Lumpur, Malaysia, October 20-21, 2003.
13. Frampton, H., Morgan, J.C., Cheung, S.K., Munson, L., et al.: "Development of a Novel Waterflood Conformance Control System," SPE paper 89391, presented at the SPE/DOE Symposium on Improved Oil Recovery, Tulsa, Oklahoma, April 17-21, 2004.
14. Zaitoun, A., Tabary, R., Rousseau, D., Pichery, T.R., et al.: "Using Microgels to Shut off Water in a Gas Storage Well," SPE paper 106042, presented at the International Symposium on Oil Field Chemistry, Houston, Texas, February 28-March 2, 2007.
15. Moradi, B., Pourafshary, P., Farahani, F.J., Mohammadi, M., et al.: "Application of SiO_2 Nano Particles to Improve the Performance of Water Alternating Gas EOR Process," SPE paper 178040, presented at the SPE Oil and Gas India Conference and Exhibition, Mumbai, India, November 24-26, 2015.
16. Mokhatab, S., Fresky, M.A. and Rafiqul Islam, M.: "Applications of Nanotechnology in Oil and Gas E&P," *Journal of Petroleum Technology*, Vol. 58, Issue 4, April 2006, pp. 48-51.
17. Esmaeili, A.: "Applications of Nanotechnology in the Oil and Gas Industry," *AIP Conference Proceedings*, Vol. 1414, Issue 1, 2011, pp. 133-136.
18. Evdokimov, I.N., Eliseev, N.Y., Losev, A.P. and Novikov, M.A.: "Emerging Petroleum Oriented Nanotechnologies for Reservoir Engineering (Russian)," SPE paper 102060, presented at the SPE Russian Oil and Gas Technical Conference and Exhibition, Moscow, Russia, October

3-6, 2006.

19. Chaudhury, M.K.: "Complex Fluid: Spread the World about Nanofluids," *Nature*, Vol. 423, Issue 6936, May 2003, pp. 131-132.
20. Hendraningrat, L., Li, S. and Torsater, O.: "Effect of Some Parameters Influencing Enhanced Oil Recovery Process Using Silica Nanoparticles: An Experimental Investigation," SPE paper 165955, presented at the SPE Reservoir Characterization and Simulation Conference and Exhibition, Abu Dhabi, UAE, September 16-18, 2013.
21. Shah, R.D.: "Application of Nanoparticle Saturated Injectant Gases for EOR of Heavy Oils," SPE paper 129539, presented at the SPE Annual Technical Conference and Exhibition, New Orleans, Louisiana, October 4-7, 2009.
22. Almohsin, A.M., Bai, B., Imqam, A.H., Wei, M., et al.: "Transport of Nanogel through Porous Media and Its Resistance to Water Flow," SPE paper 169078, presented at the SPE Improved Oil Recovery Symposium, Tulsa, Oklahoma, April 12-16, 2014.
23. Patil, P.R. and Kalgaonkar, R.: "Environmentally Acceptable Compositions Comprising Nanomaterials for Plugging and Sealing Subterranean Formations," SPE paper 154917, presented at the SPE International Oil Field Nanotechnology Conference, Noordwijk, the Netherlands, June 12-14, 2012.
24. Vryzas, Z., Mahmoud, O., Nasr-El-Din, H.A. and Kelessidis, V.C.: "Development and Testing of Novel Drilling Fluids Using Fe_2O_3 and SiO_2 Nanoparticles for Enhanced Drilling Operations," IPTC paper 18381, presented at the International Petroleum Technology Conference, Doha, Qatar, December 6-9, 2015.

BIOGRAPHIES

Dr. Jin Huang is a Petroleum Scientist working with the Production Technology Division of Saudi Aramco's Exploration and Petroleum Engineering Center – Advanced Research Center (EXPEC ARC). Her current research interests are water management related oil field chemistry.

Prior to joining Saudi Aramco in 2015, Jin worked as with Weatherford Laboratories Inc. and Intertek Westport Technology Center in Houston, Texas. She was intensively involved in reservoir fluids analysis, drilling fluid analysis and water chemistry. Jin also worked at GTC Technology Inc. in Houston as a Process Chemist, and worked as a postdoctoral researcher at Texas A&M University, College Station, Texas.

In 1994, Jin received her B.S. degree in Polymer Chemistry from Tianjin University, Tianjin, China; and in 2004, she received her Ph.D. degree in Inorganic Chemistry from the University of Houston, Houston, Texas.

Dr. Ayman M. Al-Mohsin has worked with Saudi Aramco since 2014 as a Research Engineer. His research focuses on developing materials to prevent/reduce excess water and gas production during oil recovery.

Ayman received his B.S. degree in Mechanical Engineering from the University of New Haven, West Haven, CT; his M.S. degree in Petroleum Engineering from New Mexico Tech, Socorro, NM; and his Ph.D. degree in Petroleum Engineering from Missouri University of Science and Technology, Rolla, MO.

Dr. Mohammed A. Bataweel is a Champion for the Smart Fluid focus area in the Production Technology Division of Saudi Aramco's Exploration and Petroleum Engineering Center – Advanced Research Center (EXPEC ARC). He has led his team in the development and deployment of several in-house technologies in Saudi Aramco fields. Throughout his career, Mohammed has represented his department on several field development, asset, and multidisciplinary teams. His research interests include formation damage due to drilling and completion fluids, investigation and mitigation of injectivity decline, conformance control, sand production prediction, special core analysis, chemical enhanced oil recovery, productivity enhancement technologies, visualization of fluid flow in porous media, and oil field chemicals.

Mohammed is an active member of the Society of Petroleum Engineers (SPE) where he has served on several conferences. He initiated and co-chaired several SPE advanced technical workshop series in the region. Mohammed has published more than 40 SPE papers in local and international conferences and refereed journals.

He received his B.S. degree in Mechanical Engineering from King Fahd University of Petroleum and Minerals (KFUPM), Dhahran, Saudi Arabia, and his M.S. degree in Petroleum Engineering from Harriot-Watt University, Edinburgh, U.K. Mohammed received his Ph.D. degree in Petroleum Engineering from Texas A&M University, College Station, TX.

Prasad B. Karadkar is a Petroleum Engineer with the Production Technology Team of Saudi Aramco's Exploration and Petroleum Engineering Center – Advanced Research Center (EXPEC ARC). Prior to joining Saudi Aramco in April 2016, he worked as a Senior Technical Professional for Halliburton for 9 years. Prasad's areas of expertise include developing new fluid systems in the area of hydraulic fracturing, acidizing, diversion, and water shutoff.

He has authored and coauthored 16 papers, published one patent, and has several patent applications in process.

In 2003, Prasad received his B.S. degree in Chemical Engineering from Shivaji University, Kolhapur, India, and in 2007, he received his M.S. degree in Chemical Engineering from Nagpur University, Nagpur, India.

Dr. Wengang Li joined Saudi Aramco in April 2016 as a Geologist, and works in the Production Technology Division of Saudi Aramco's Exploration and Petroleum Engineering Center – Advanced Research Center (EXPEC ARC). He is currently working in the smart fluids focus area.

Wengang's research area is to develop advanced materials for production enhancement technologies such as hydraulic fracturing, water shut-off, and wettability alteration. He is the lead for the Saudi sand-hydraulic fracturing proppant project.

Before joining Saudi Aramco, Wengang worked as postdoctoral researcher in Tianjin University with Nobel Prize Laureate (2016) Sir J. Fraser Stoddart in the area of supramolecular chemistry and cyclodextrin-based metal organic frameworks.

In 2009, he received his B.S. degree in Applied Chemistry from Tianjin University, Tianjin, China. In 2010, Wengang received his M.S. degree in Chemical Science, and in 2014, he received his Ph.D. degree in Chemical Science, both from King Abdullah University of Science and Technology (KAUST), Thuwal, Saudi Arabia.

Abrar A. Alshaikh is a Petroleum Engineer with Saudi Aramco's Drilling Technology Team of the Exploration and Petroleum Engineering Center – Advanced Research Center (EXPEC ARC). She has worked on several research and development projects, mainly in the area of drilling optimization and automation.

Abrar has filed one patent and published several technical papers. Currently, she is on an assignment working as a Drilling Engineer with the Exploration and Oil Drilling Engineering Department.

Abrar received her B.S. degree in Petroleum Engineering from Texas A&M University, College Station, TX.

Getting More Out of Your Multistage Fracturing Open Hole Completion

Kirk M. Bartko, Syed Muhammad, Maksim Oparin, Roberto Tineo, Fadhel A. Abu Al-Makarem, Ankur Desai, and Jasim Al Ulaiw

ABSTRACT

Saudi Aramco's Unconventional Production Engineering Division currently performs multistage propped fracturing operations using cemented plug-and-perf completions to target tight gas reservoirs requiring stimulation. To improve operational efficiency and eliminate wireline intervention and coiled tubing milling operations, the decision was made to test an open hole multistage fracture (MSF) system. This came with the challenge of ensuring adequate reservoir contact, comparable to the cemented plug-and-perf operations, where 21 perforation clusters, on average, are targeted.

The open hole MSF technology chosen consists of multiple fracturing ports per stage with high-pressure mechanical packers to isolate each stage and slip-on oil swell packers to isolate the individual fracturing port within a stage. This new method of diversion within the compartment itself helps to ensure that small variances in pressure between nozzle ports are isolated, thereby preventing the fracture operation within a stage from consolidating to a single entry point. Like standard ball drop sleeve systems, the open hole multiple entry fracturing sleeve system uses progressively increasing diameter balls to open each stage. A single ball will open all the ports in one stage, simulating multiple clusters per stage. This allows for an increase in reservoir contact when stimulating large open hole lengths.

Case study Well-A was completed with six multiple entry stages, three entry points per stage, and one toe stage utilizing a hydraulic port resulting in a total of seven stages and 19 fracturing sleeves. The isolation plan for this well consisted of mechanical packers between the six main stages and the slip-on constrictors between the individual ports within each stage. Each fracture port was engineered with three jets — of 0.563" hole diameter — as part of the limited entry design. All the fracture stages were performed as per design. The initial production response was better than offset wells completed with the plug-and-perf technique. A production log suggests contribution from 75% of each individual jet, indicating the proper diversion was achieved. Using a seven-stage open hole system yielded 17 effective fractures contributing to production. By utilizing open hole multiple entry MSF system technology for limited entry fracturing, Saudi Aramco has improved reservoir productivity and operation efficiency.

This is the first time an open hole MSF system combining mechanical and slip-on oil swell packers has been deployed to promote limited entry diversion. This qualified and field tested novel completion methodology ensures proper fracturing diversion between frac ports located within the same stage. The benefits of this technology include improved reservoir contact, operation efficiency, cost reduction, and placement improvement.

INTRODUCTION

Open hole multistage fracturing (MSF) completions have been deployed in tight and unconventional plays to effectively place multistage fractures along the horizontal lateral. This completion competes directly with the more widespread use of plug-and-perf technology and is not always considered due to stage limitations, number of clusters per stage, and the economics of running the completion.

The advantages and disadvantages of an open hole MSF system were discussed by Appleton and Rivenbark (2013)[1] and Casero (2013)[2], which indicated the open hole system advantages are as follows:

- Elimination of the cementing operation.
- No wireline or coiled tubing operations.
- No explosive handling.
- Lower breakdown pressures.
- Reduction in operation time to complete the stages.
- Less equipment on-site.
- The ability to capture hydrocarbons from the matrix as well as natural fractures.

The disadvantages of running an open hole completion are as follows:

- Difficulty in achieving proper landing of the completion.
- Packer failing to hold the required differential pressure.
- No control of fracture placement.
- Proppant flow back.

- Limited number of stages.

The operational disadvantages can be controlled by using best practices developed for running open hole MSF completions for each specific field. Best practices for Saudi Aramco require the following:

- Open hole caliper for placement of the packers.
- Packer differential pressures calculated for each individual packer based on required expansion of the packer.
- Dogleg severity of less than 10°/100 ft.
- No open hole section in the curved section of the lateral.
- Perform a required dummy reamer run to calculate the final torque and drag, and eliminate all tight spots in the lateral.

Performance of the open hole MSF systems were evaluated by Rahim (2011)[3]; the results indicated the open hole MSF completions when properly placed and stimulated outperformed wells that were stimulated using the conventional systems. Later work indicated plug-and-perf completions performed better than open hole MSF due to the risks in not generating independent fractures due to packer failures and the limited fracturing sleeve points of the current systems[4]. The study also indicated the open hole MSF completions have an advantage in tight reservoirs where matrix permeability and natural fractures can provide additional inflow into the lateral. The authors recommended that each reservoir be evaluated separately based on reservoir and well conditions.

To overcome the limited fracturing sleeve entry points, a new open hole MSF system was developed that utilized an open hole multiple entry stage fracturing system combining mechanical and constrictor swell packers to foster limited entry diversion. This qualified and field tested novel completion methodology ensures proper fracturing diversion between fracturing ports located within the same stage. The benefits of this technology include improved reservoir contact, operation efficiency, cost reduction, and placement improvement.

COMPLETION

Limited Entry Multistage Sleeve (LEMSS)

Historically, single ports were opened by an actuation ball, and treatment of the entire stage was performed through a single entry point, where each stage is flanked by hydromechanical open hole packers, Fig. 1. This meant the whole stage was

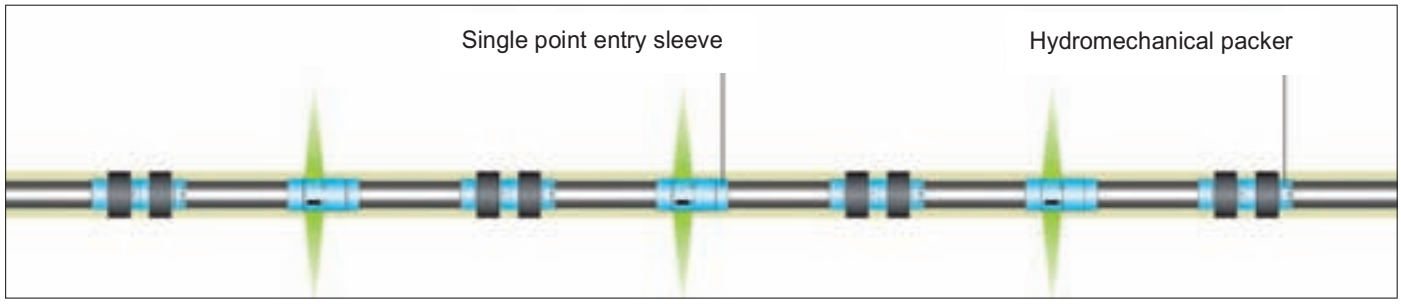

Fig. 1. Single-point entry system.

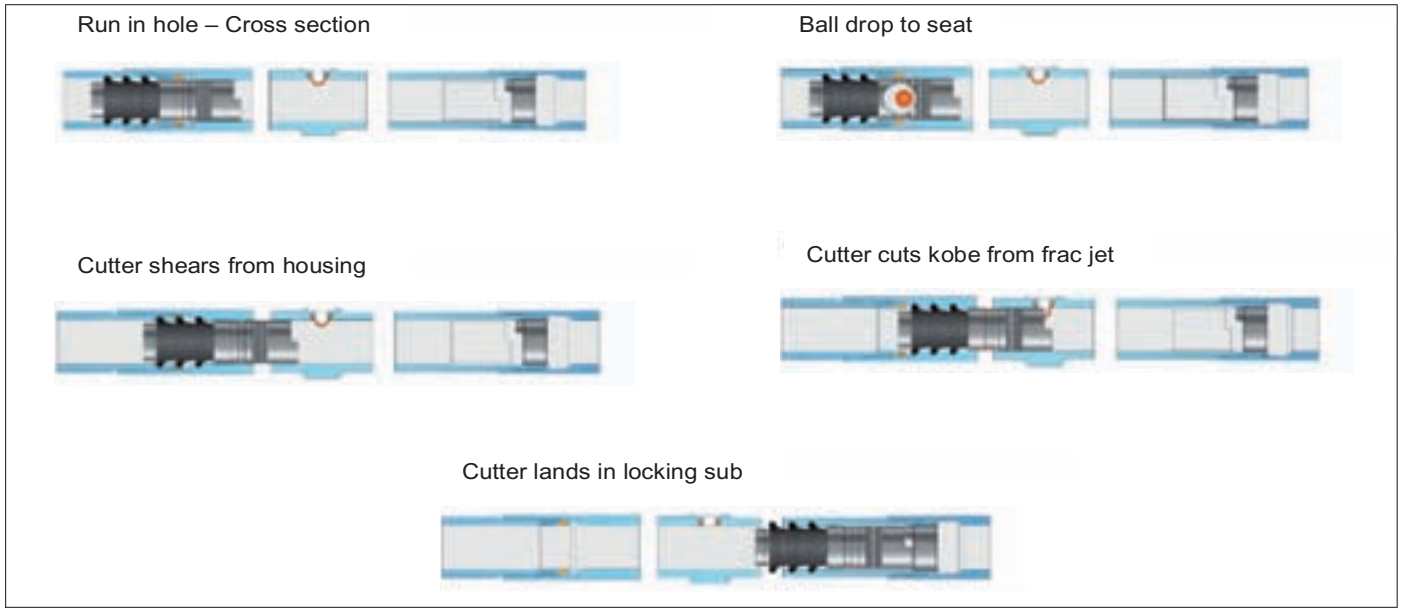

Fig. 2. The old LEMSS design with cutter sub.

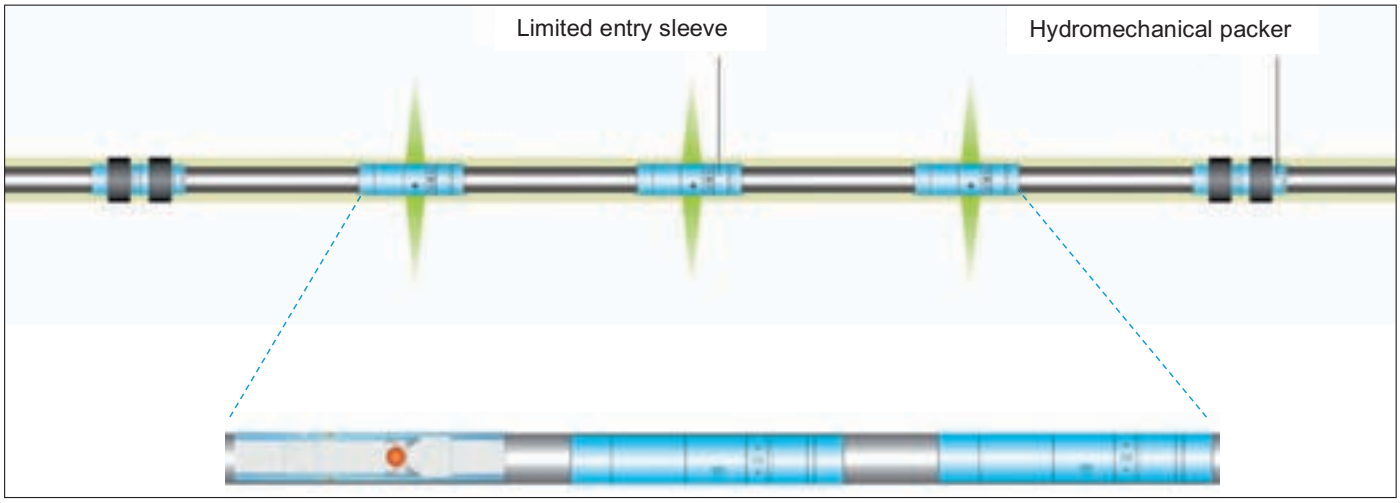

Fig. 3a. The new LEMSS design with a ball drop system.

treated via one entry point, which was simply not efficient in stimulating long fracturing stages, therefore, a new innovative technology was introduced.

The old limited entry multistage sleeve (LEMSS) design allowed for multiple entry points to be opened by a single pumped ball, which launched a cutter sub, which in turn, sheared off multiple stimulation jets, Fig. 2. This method proved successful but had limitations and drawbacks: it required a high pump rate, only allowed for one entry point for each sleeve, left debris in the well, required considerable milling, did not give clear signatures of all jet openings, and had a small internal diameter (ID).

Because of these limitations, a new design was conceived that relies solely on a single pumped ball to actuate multiple hydraulically activated injection/production ports, Fig. 3a. These ports allow for more than one sleeve to be activated with the same size actuation ball using minimal pump rates, and each sleeve has three exit points spaced 120° apart to enhance fluid distribution, as seen in Fig. 3a. The flow ports are available in a variety of sizes to optimize the limited entry stimulation treatment, and a clear signature can be obtained of each port opening. The innovative design allows all the balls to be either flowed back or dissolved after stimulation, and the well can be immediately put on production without any milling and/or intervention work because the ID has minimal restriction. Evolution of the LEMSS design and the single entry sleeve is shown in Fig. 3b. Table 1 lists some of the comparisons between the old and new LEMSS designs.

Modern LEMSS completion technology provides controlled injection and even distribution into the intervals by using limited entry nozzles, which are sized based on an application specific pumping pressure. The technology enables controlled injection and leakoff for an even distribution of acid into each isolated stage.

Nozzle Design

The LEMSS system has a total of five nozzles per fracturing

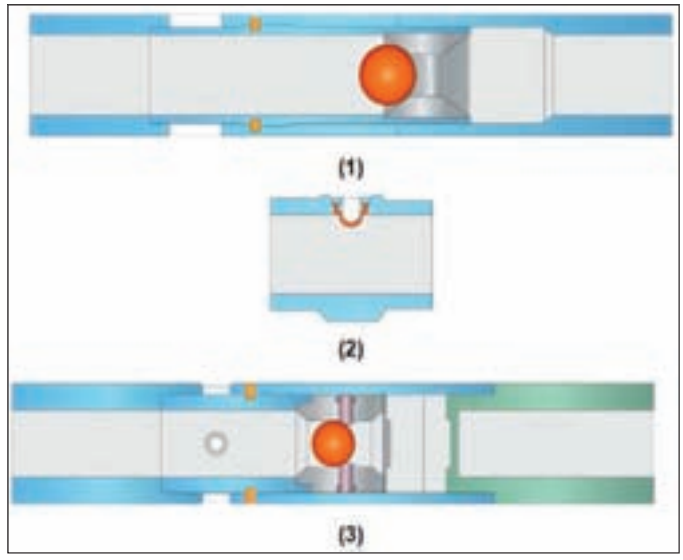

Fig. 3b. Evolution of sleeve design: (1) single-point entry sleeve, (2) limited entry one entry point per nozzle with restricted ID, and (3) limited entry with multiple nozzles per port with a large ID.

sleeve with each port having a 1.0" diameter nozzle. The ports can be configured to provide a limited entry stimulation, which ensures fluid entry at the top and bottom of the fracturing sleeve. For Well-A, based on the limited entry formula[5], the design called for 3 × 0.563" nozzles/sleeve. The nozzles are covered with aluminum jet covers with 0.325" hole, which erodes to 0.625". At 10 bbl/min while opening the sleeves, the nozzles will be 0.375" per nozzle = ±500 psi pressure drop, which is ideal for opening the ports. At 55 bbl/min during the planned stimulation rate for Well-A, the 3 × 0.563" per nozzle = ±800 psi pressure drop, which is, again, ideal for limited entry stimulation, as per Eqn. 1:

$$P_{fr} = 0.2369 \frac{q^2 \rho_s}{N_{\text{nozzle}}^2 D_{\text{nozzle}}^4 C_d^2} \quad (1)$$

where P_{fr} = friction pressure (psi), q = flow rate (bbl/min), P_s = slurry density (lbm/gal), N_{nozzle} = number of nozzles, D_{nozzle} = diameter of nozzle (in.), and C_d = coefficient of discharge (0.95).

Old Design	New Design
Mechanical cutter through kobes In this system, the ball is dropped onto a cutter sub and is displaced down to knock off kobes. The kobes are the internal covers of the stimulation jet.	**Collapsible ball seat** No cutter required. The ball is displaced from one port to the next.
Debris Introduces small pieces of the kobes (debris) into the system.	**Debris** No internal debris.
Number of sleeves in a single stage Up to six sleeves per stage maximum.	**Number of sleeves in a single stage** Only limited by surface pressure.
Injection nozzles in a single sleeve One nozzle per port.	**Injection nozzles in a single sleeve** Up to five nozzles per port.
Maximum ball seat 2.625", limited number of stages.	**Maximum ball seat** Up to 3.625".
Port opening signatures One signature while shearing the cutter sub.	**Port opening signatures** An independent signature of each port as it opens.
Pumping rate Up to 25 bbl/min to 30 bbl/min typically required for the pumping operation.	**Pumping rate** Ball can be seated and can the activate sleeves at approximately 5 bbl/min to 15 bbl/min.
Milling Milling through the cutter sub with rubber and the knocked off kobes.	**Milling** Milling only the seats and one ball/stage if required.

Table 1. Some of the comparisons between the old and new LEMSS designs

Constrictor

The constrictor is a slip-on swellable elastomer isolation system with a pressure rating of < 1,000 psi across a 5⅞" gauged hole. The swelling mechanism uses thermodynamic adsorption where the hydrocarbon is absorbed into the element, and then bonds with it on a molecular level. The element requires no mechanical, hydraulic, or setting tool forces to activate; it only requires contact with hydrocarbon fluids, Fig. 4.

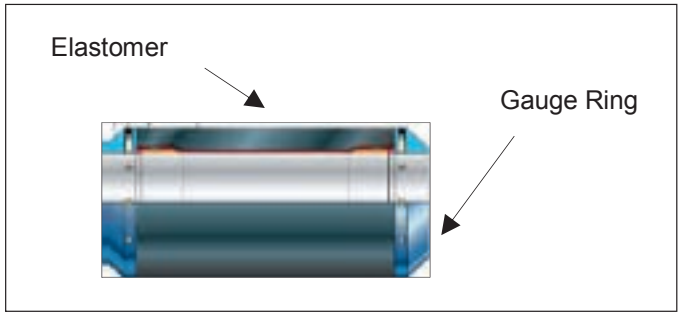

Fig. 4. The constrictor is a slip-on swellable elastomer isolation system.

Stage Design

The completion plan for Well-A included one pressure activated sleeve at the toe and six fracturing stages with three LEMSSs per stage. Each open hole stage included two 1,000 psi pressure differential swellable constrictors with three sleeves separated by a constrictor, Fig. 5. Each stage has approximately 300 ft to 400 ft of open hole section. As a result, Well-A has seven stages for placing 19 fractures.

The focus of the limited entry sleeve and the constrictors was to focus each individual fracture within its respective compartment. The constrictor's low delta pressure (dp) rating of < 1,000 psi is sufficient if each compartment has a similar rate at pressure. If the completion is not balanced, then the constrictors would fail, and the fractures would initiate at the least path of resistance, as seen in the single-stage completions.

CASE STUDY

Horizontal cemented liner completions combined with

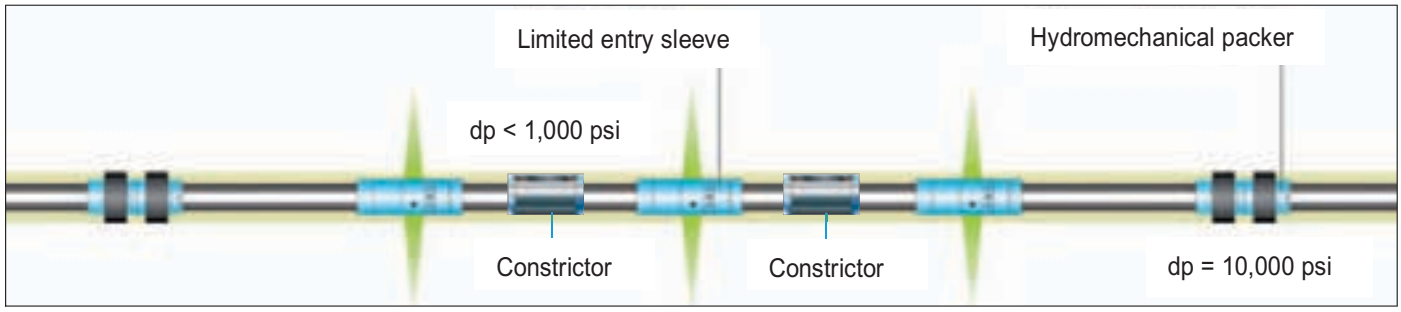

Fig. 5. Final completion design showing two constrictors in place.

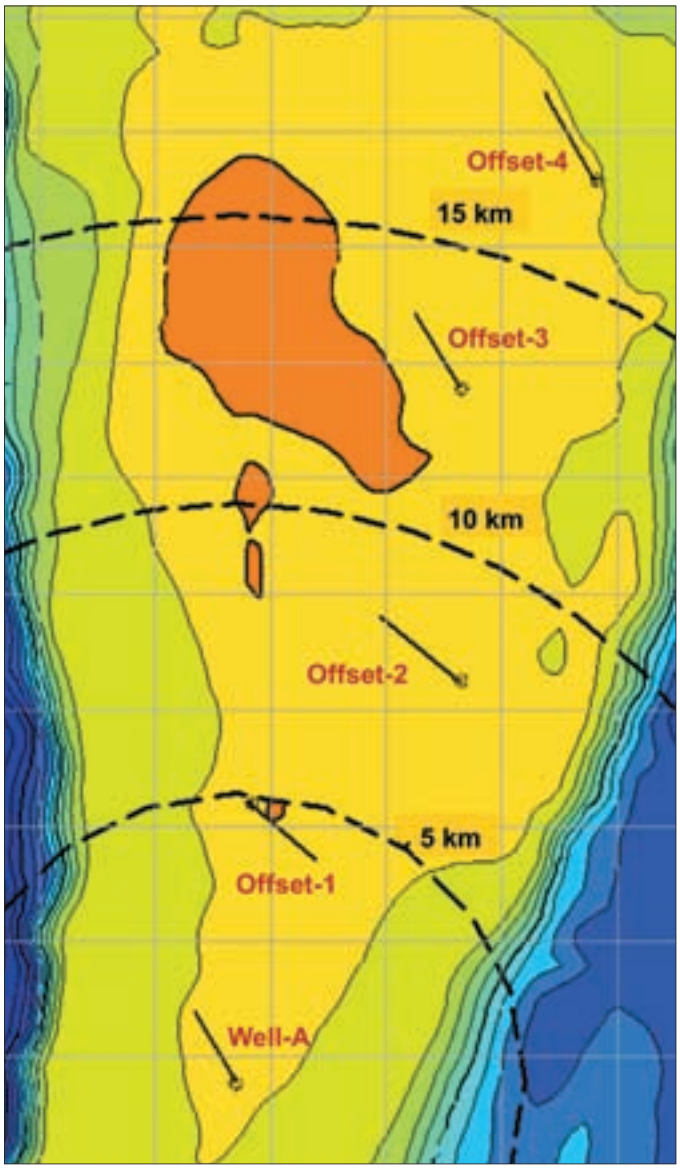

Fig. 6. Horizontal wells located near Well-A.

plug-and-perf stimulations have been traditionally used to develop the Q formation located in the Mazalij basin of Saudi Arabia. A typical completion consists of seven to 17 stages with three clusters per stage to cover a lateral length from 2,000 ft to 4,700 ft.

Well-A was selected to deploy the novel open hole MSF system as previously described, including seven stages and a total of 19 fracture initiation ports. All the horizontal wells located near Well-A, Fig. 6, were completed in the same Q formation using similar stimulation pumping schedules. They were used to compare the well productivity, cluster efficiency, and operation efficiency of the cemented liner against the open hole MSF system in this area. The well labeled offset 1 is the closest to Well-A, located at 5 km, and the well labeled offset 3, located approximately 12.6 km from Well-A, is currently the best producing well in the basin.

The Q formation is a clean, tight gas sandstone with porosity up to 8% and net thickness between 100 ft and 200 ft. Well-A did not have a pilot hole available; therefore, the offset

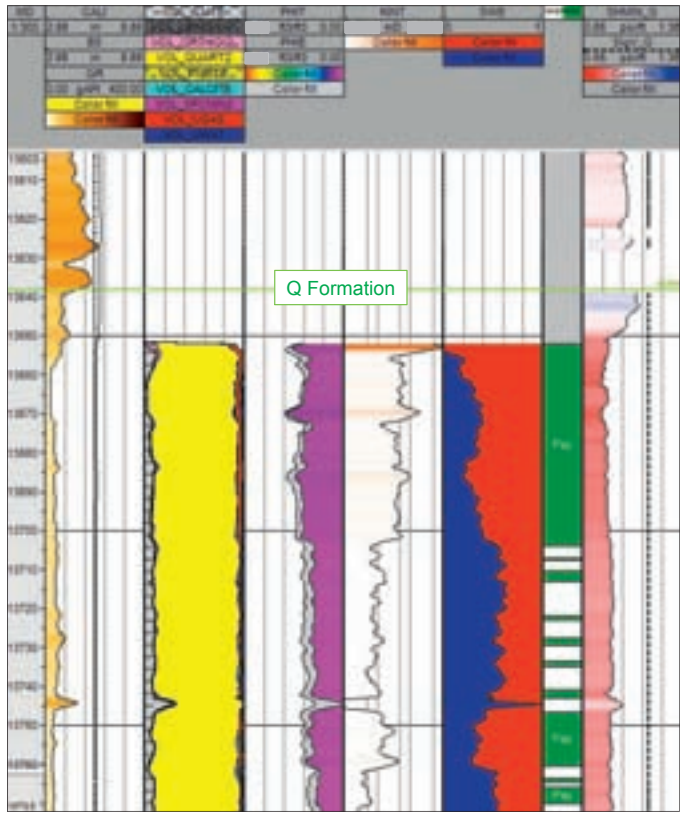

Fig. 7. Offset 1 well pilot open hole logs.

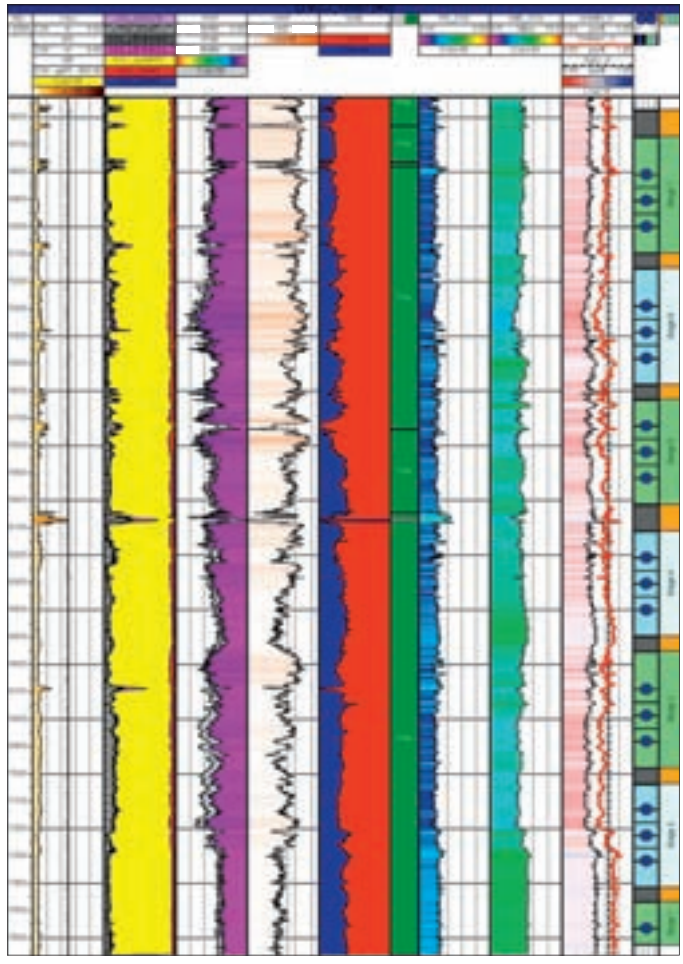

Fig. 8. Well-A lateral log montage.

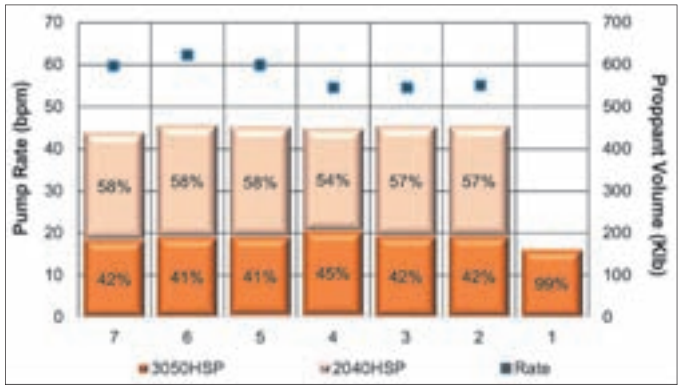

Fig. 9. Well-A proppant placement.

1 pilot well was used as a reference to build the petrophysical and geomechanical models. Figure 7 shows the pilot open hole logs from the offset 1 well for the zone of interest.

Well-A lateral measurements were available to compute reservoir and completion quality indicators and drive the location of the open hole MSF system. Figure 8 illustrates the Well-A lateral log montage, including the petrophysical and geomechanical properties along with the ports, packer, and constrictor locations.

TREATMENT

The fracture treatment was designed using a total of 150,000 lbm of proppant per fracturing port, with a split of 40% 30/50 high-strength proppant (HSP) and 60% 20/40 HSP and proppant concentration from 0.5 to 5 pounds per proppant added. The only exception was stage 1, which was designed using 100% 30/50 HSP as a precaution to understand proppant admittance before moving to a larger proppant size. The pumping rate was designed at 55 bbl/min per stage, to promote a limited entry diversion with a pressure gain of approximately 814 psi as indicated in the nozzle design.

All seven stages were pumped as per design without any proppant placement issue, Fig. 9. The average proppant volume per stage was 450,000 lbm, except for stage 1 where 150,000 lbm was placed. The pumping rate for the slurry was 55 bbl/min, which was increased for the last three stages, up to 60 bbl/min.

The total near wellbore friction was estimated at the end of

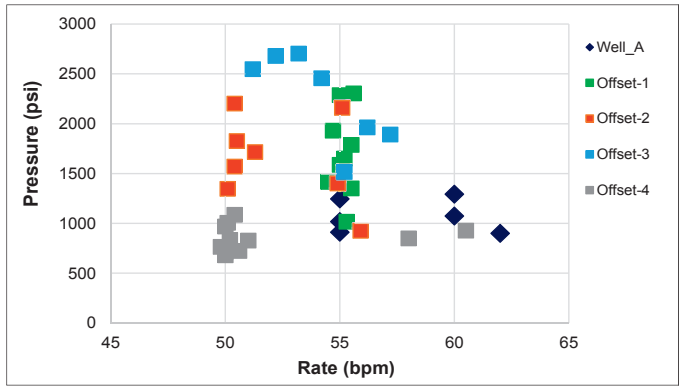

Fig. 10. End of job total near wellbore friction.

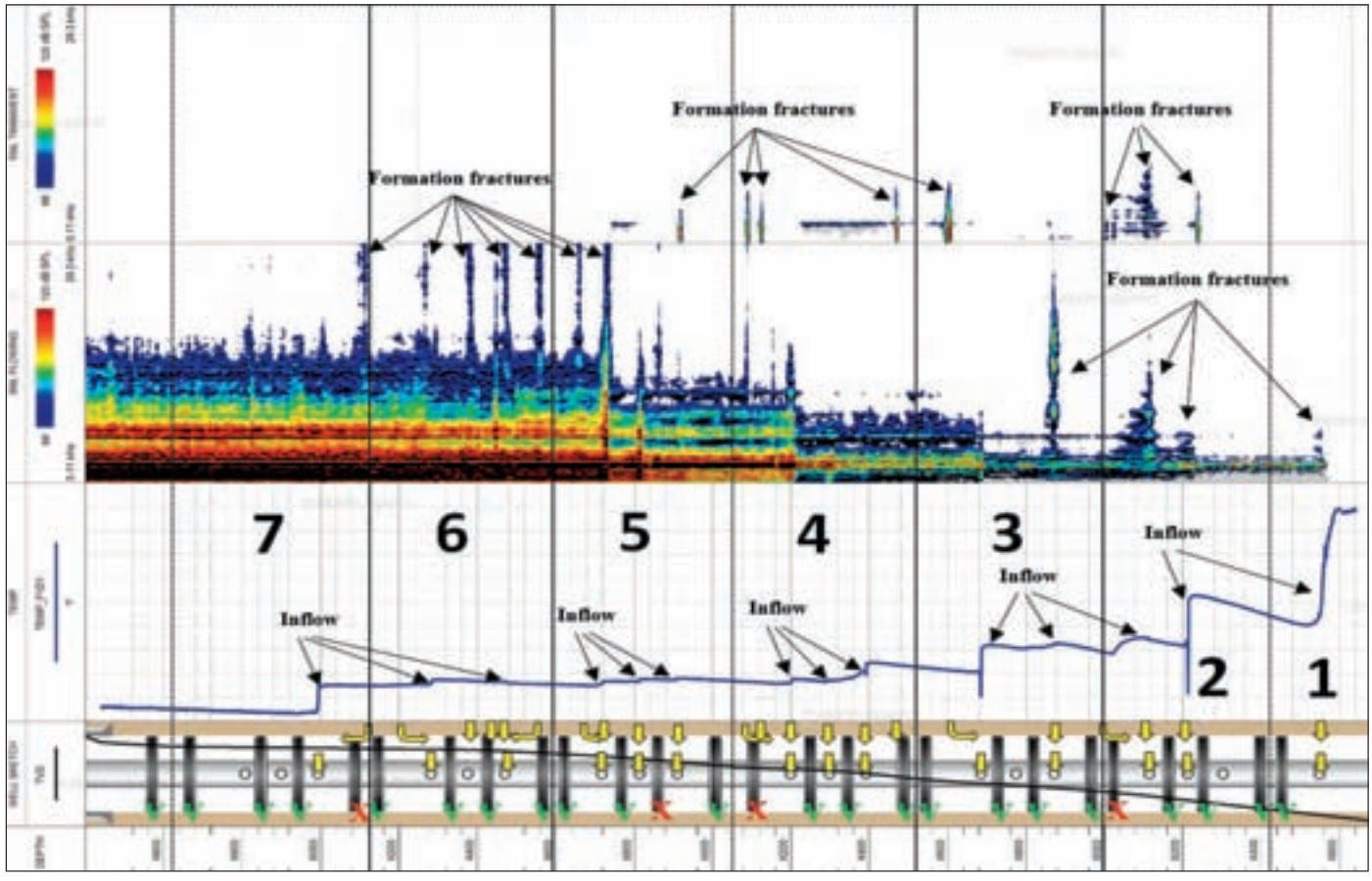

Fig. 11. Survey summary, fracture contributions, and assessment of bypass packers and active ports[8].

each fracture stage subtracting the initial shut-in pressure (ISIP) value from the calculated bottom pressure before shut-in. No step-down was conducted. Therefore, we were unable to discriminate between tortuosity and orifice friction, and only the total near wellbore friction with its associated pumping rate was reported, Fig. 10. The pressure drop calculated for Well-A is consistently between 900 psi and 1,300 psi, very close to the designed pressure required for limited entry diversion purposes previously discussed. Excluding the offset 4 well, all the other offset wells completed with cemented liners show a very variable near wellbore pressure, ranging from 900 psi up to 2,700 psi. Many stages showed a pressure drop above 1,500 psi, which is considered excessive for this application; we think this is related to a combination of cement quality and breakdown pressure variations along the lateral.

RESULTS

Several tools were evaluated to determine the most effective diagnostic tool for determining fracture initiation points behind an open hole completion. Conventional logging tools were considered; however, the interpretation of flow geometry behind the pipe was considered too complex, especially when considering flow rates below the threshold of the spinner. Radioactive tracers were also considered; however, they were dismissed due to the possibility of the radioactive tracers communicating around the swellable constrictors even if they held during the fracture treatment. High precision temperature logging was a viable alternative to the above diagnostics because the survey can provide a dynamic picture of the inflow by comparing time-lapse static surveys.

The preferred method, which proved to show the fracture initiation locations, was utilization of the spectral noise logging (SNL) tool, and the high precision temperature survey. The tool is designed to record acoustic noise generated by the inflow of liquid and gas at different frequency ranges[6, 7]. The SNL can identify active flow below the threshold of a spinner and can even hear behind multiple barriers.

The interpretation of spectral noise logging and high precision temperature identified the presence of 22 active fractures; 17 were offset from flow ports, and five might be aligned with the flow ports with a unique signature covering a wide frequency range. The fracture distribution varied between stages with an average of three active fractures per stage, with exceptions of stage 7, near the heel with only one induced active fracture, and stage 6 with almost six contributing active fractures. Logging results show overall good completion integrity with only three bypassed hydraulic packers and one bypassed swellable constrictor, Fig. 11; with no major influence on the total stage contribution[8].

The results confirm the success of the fracturing operation and confirms the suitability to the field and formation type.

The productivity index (PI) normalized by the number of clusters or fracture sleeves was calculated during the initial production to compare the productivity of Well-A against the offset wells, Fig. 12. Well-A showed a 32% higher normalized PI compared to the best well in the area completed with a cemented liner, identified as offset 3. Compared to the closest offset well, Well-A showed a 76% higher PI.

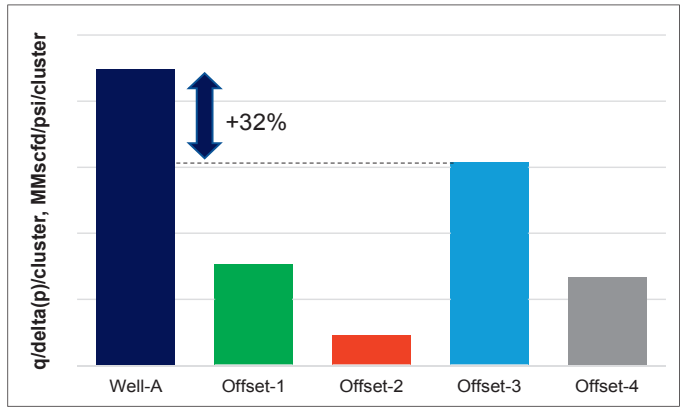

Fig. 12. Normalized PI comparison between Well-A and the offset wells.

CONCLUSIONS

1. The new completion effectively initiated separate fractures per compartment.
2. Low-pressure constrictors successfully contained the fractures within the compartments; an average of three active fractures per stage was achieved.
3. The combination of the SNL and high precision temperature logging successfully identified fracture locations and mechanical integrity of the completion.
4. The new completion shows a 32% to 76% higher initial normalized PI compared to offset wells.
5. The new completion shows more consistent and lower total near wellbore friction compared to the offset wells.

ACKNOWLEDGMENTS

The authors would like to thank the management of Saudi Aramco, Schlumberger, and Packers Plus for their support and permission to publish this article. The authors would also like to thank all the support and operation people that were involved in making this a successful completion.

This article was presented at the SPE International Hydraulic Fracturing Technology Conference and Exhibition, Muscat, Oman, October 16-18, 2018.

REFERENCES

1. Appleton, J. and Rivenbark, M.: "Cemented vs. Open Hole Completions: What is best for Your Well?" SPE paper 163946, presented at the SPE Unconventional Gas Conference and Exhibition, Muscat, Oman, January 28-30, 2013.

2. Casero, A., Adefashe, H.A. and Phelan, K.M.: "Open Hole Multistage Completion System in Unconventional Plays: Efficiency, Effectiveness and Economics," SPE paper 164009, presented at the SPE Unconventional Gas Conference and Exhibition, Muscat, Oman, January 28-30, 2013.
3. Rahim, Z., Al-Kanaan, A.A., Johnson, B., Wilson, S., et al.: "Success Criteria for Multistage Fracturing of Tight Gas in Saudi Arabia," SPE paper 149064, presented at the SPE/DGS Saudi Arabia Section Technical Symposium and Exhibition, al-Khobar, Saudi Arabia, May 15-18, 2011.
4. Rahim, Z., Al-Kanaan, A.A., Al-Anazi, H., Kayumov, R., et al.: "Comparing Effectiveness between Cemented Plug and Perf and Open Hole Ball Drop Completion Assemblies to Ensure Optimal Multistage Fracturing Treatment and Well Performance — Field Examples," SPE paper 177511, presented at the Abu Dhabi International Petroleum Exhibition and Conference, Abu Dhabi, UAE, November 9-12, 2015.
5. Willingham, J.D., Tan, H.C. and Norman, L.R.: "Perforation Friction Pressure of Fracturing Fluid Slurries," SPE paper 25891, presented at the SPE Low Permeability Reservoirs Symposium, Denver, Colorado, April 26-28, 1993.
6. Ghalen, S., Serry, A.M., Al-Falasi, A., Berrim, A., et al.: "Innovative Logging Tool Using Noise Log and High Precision Temperature Help Diagnosis Complex Problems," SPE paper 161712, presented at the Abu Dhabi International Petroleum Conference and Exhibition, Abu Dhabi, UAE, November 11-14, 2012.
7. Suarez, N., Otubaga, A., Mehrotra, N., Aslanyan, A., et al.: "Complementing Production Logging with Spectral Noise Analysis to Improve Reservoir Characterization and Surveillance," paper presented at the Society of Petrophysicists and Well Log Analysts 54th Annual Logging Symposium, New Orleans, Louisiana, June 22-26, 2013.
8. Oparin, M., Al-Tayyar, T., Al-Otaibi, N., Sheshtawy, M., et al.: "Complete Assessment of Complex Unconventional Saudi Arabian Producer Using High Definition Spectral Noise Logging and Numerical Temperature Modeling," SPE paper 191735, presented at the SPE Annual Technical Conference and Exhibition, Dallas, Texas, September 24-26, 2018.

BIOGRAPHIES

Kirk M. Bartko is a Senior Petroleum Engineering Consultant with Saudi Aramco's Well Completion Operations & Production Engineering Department, where he is currently in the Technical Support Unit on stimulation and completion development for unconventional gas operations. Kirk joined Saudi Aramco in 2000, where he worked to support hydraulic fracturing and completion technologies across all Saudi Arabia operations. Kirk's experience includes 19 years with ARCO with various global assignments in locations including Texas, Alaska, Algeria, and the Research Technology Center supporting U.S. and international operations.

He has authored and coauthored more than 50 technical papers on well stimulation and is a recipient of four U.S. granted patents. Kirk has been actively involved in the Society of Petroleum Engineers (SPE) since 1977.

He received his B.S. degree in Petroleum Engineering from the University of Wyoming, Laramie, WY.

Syed Muhammad is a Petroleum (Completion) Engineering Specialist with Saudi Aramco's Well Completion Operations & Production Engineering Department. He joined Saudi Aramco in 2015, and is currently a part of the Technical Support Unit, providing completion hardware engineering support for all unconventional resources completion engineering initiatives. Syed has 20 years of experience in completion engineering, having working extensively in the Asia Pacific, the continental United States, and Alaska, working for both Baker Hughes and ConocoPhillips.

He received his B.Eng. degree (Mechanical) from the University of Aberdeen, Aberdeen, Scotland.

Maksim Oparin is a Production Engineer with Saudi Aramco's Well Completion Operations & Production Engineering Department. He has 16 years of experience in the oil and gas industry. Maksim worked at Schlumberger as a Stimulation Engineer in various areas of Russia before joining Saudi Aramco as a Production Engineer in 2013.

He has authored and coauthored 11 technical publications and completed the Engineering certification program of the Society of Petroleum Engineers (SPE).

Maksim received his M.S. degree in Petroleum Engineering from Gubkin Russian State University of Oil and Gas, Moscow, Russia.

Roberto Tineo is currently a Stimulation Lead Engineer for Schlumberger working in Neugen, Argentina. He has been with Schlumberger for 17 years, occupying several technical roles related to unconventional reservoirs, reservoir simulation, hydraulic fracturing, sand control, and matrix acidizing. Roberto's experience includes work in different basins across Venezuela, the United States, Saudi Arabia, and Argentina.

He is an active member of the Society of Petroleum Engineers (SPE). Roberto has coauthored several publications, and participated in numerous workshops.

He received his B.S. degree in Electronic Engineering from Simón Bolivar University, Caracas, Venezuela.

Fadhel A. Abu Al-Makarem is a Technical Support Engineer with Schlumberger Wireline. He has been with Schlumberger for 12 years. Fadhel started as a Wireline Field Engineer, then held a position of a Field Services Manager for the Wireline Special Services. He then moved to Schlumberger Completions to work as a Technical Support Engineer for multistage stimulation and unconventional resources. Fadhel later moved back to Wireline as a Technical Support Engineer to work on workover and production services.

He received his B.S. degree in Applied Electrical Engineering from King Fahd University of Petroleum and Minerals (KFUPM), Dhahran, Saudi Arabia.

Ankur Desai is Completion Project Manager for Schlumberger in Dhahran, Saudi Arabia. He has been with Schlumberger for 13 years, having both operational and technical experience in a wide variety of completion product lines, including multistage fracturing, sand control tools, liner hangers, intelligent completions, high-pressure, high temperature completions, and more. Ankur's experience includes work in several locations in the United States, Bahrain, Kuwait, Canada, Mexico, Indonesia, and Saudi Arabia.

He is an active member of the Society of Petroleum Engineers (SPE).

Ankur received his B.S. degree in Mechanical Engineering from the Georgia Institute of Technology, Atlanta, GA.

Jasim Al Ulaiw is a Senior Technical Sales Representative with Packers Plus Energy Services Inc., where he is currently managing sales and introducing new technology solutions to Saudi Aramco's Conventional and Unconventional Gas Operations Department. Jasim joined Packers Plus in 2015 working to support the multistage fracture technology for technical sales and operations. He has 15 years of experience in the oil and gas industry, working for several world leading oil and gas service companies, focusing on open and cased hole completion solutions in Saudi Arabia and Qatar.

Jasim is an active member of the Society of Petroleum Engineers (SPE), and this is his first paper as a coauthor.

He received his B.S. degree in Mechanical Engineering from King Fahd University of Petroleum and Minerals (KFUPM), Dhahran, Saudi Arabia.

Structural and Quantitative Phase Analysis of XRD Data of Sludge Deposits from Refineries and Gas Plants by Using the Rietveld Method

Rasha Abdullah Al-Ghamdi and Dr. Husin Sitepu

ABSTRACT

In this article, the structure, texture and phase composition of the X-ray powder diffraction (XRD) data — generated from scale deposits from boiler equipment at a gas plant — was conducted using the Rietveld method, with the generalized spherical harmonics description for preferred orientation correction[1]. Subsequently, the sample preparation methods — developed by the authors — to separate the inorganic materials from the hydrocarbon of the sludge deposits and the other materials, were extended to perform quantitative phase analysis of XRD data, generated from deposits collected from: (1) the external surface of the boiler tubes in a refinery, (2) the inside screen cutout and the inside section of the boiler tube in a refinery, (3) the screen tube of a boiler and condenser at a gas plant, and (4) a condenser at a gas plant.

The results revealed good agreement between the measured and calculated XRD patterns of scale deposits, in the form of calcium carbonate (calcite-$CaCO_3$) formed on the boiler equipment at a gas plant; when the generalized spherical harmonics description was used to correct the intensities due to the effects of preferred orientation, and the refined structural parameters agreed well with the XRD single crystal. Additionally, the Rietveld phase analysis yields the reproducibility of the results for the deposits built up in the affected refinery and gas plant equipment. Therefore, the findings suggest that the fuel is poor if the vanadium oxide (V_2O_5), sodium vanadium oxide (NaV_2O_5), and sodium vanadium sulfate hydrate ($Na_2V(SO_4)_2$) phases appear in the examined ash deposits. Furthermore, the boiler feedwater contains dissolved oxygen — if the corrosion product is in the form of hematite (Fe_2O_3) and is present in the boiler deposits. Moreover, the presence of metallic copper (Cu) in the deposits suggests erosion in the boiler tubes. Therefore, precautions must be taken to prevent the plating out of Cu during cleaning operations.

INTRODUCTION

The sludge deposits that frequently accumulate inside oil industry equipment can cause failures and temporarily shut down operations. Sitepu et al. (2018)[2] described the new methods in sample preparation to identify the accumulated deposits from refineries and gas plants, and assessed these methods for each of the as-received sludge samples. These methods include:

1. For the water-based sludge deposits, a known quantity of deposits were taken in a beaker and dried in a fume hood for 2 to 3 days.
2. For the unknown materials produced with a sulfur product, deposits must be analyzed without pretreatment.
3. For oil-based sludge, it was treated with dichloromethane and then filtered in the filtration assembly, and therefore, the (a) dichloromethane insoluble part, i.e., inorganic materials or non-hydrocarbon, was investigated by X-ray powder diffraction (XRD) data and the Rietveld method, and (b) the dichloromethane soluble part, i.e., hydrocarbon, was analyzed by gas chromatography mass spectrometry.

Sitepu et al. (2018)[2] and Al-Ghamdi and Sitepu (2018)[3] indicated that the XRD data of a small amount of the unknown inorganic materials were successfully and accurately identified. Sitepu et al. (2018)[2] and Al-Ghamdi and Sitepu (2018)[3] pointed out that the method is quick and can accurately identify very small quantities of inorganic materials present in the sludge deposits. Moreover, they refined all the XRD data of the identified phases by using the Rietveld method quantitatively, and then calculated the weight percentage (wt%) for each of the identified phases. When all the phases of XRD data of the inorganic materials' part are identified accurately, Sitepu et al. (2018)[2] subsequently used the Rietveld method, which adjusts the refinable parameters until the best fit of the entire calculated pattern to the entire measured XRD pattern is achieved. To determine the phase composition (or wt%), W_p, i.e., the quantitative phase analysis, for each of these identified phases: p is proportional to the product of the scale factor, s, and is derived in the Rietveld phase analysis, with the mass and volume of the unit cell, and is given as:

$$W_p = s_p(ZMV)_p / \sum_{i=1}^{n} s_i(ZMV)_i \quad (1)$$

where Z, M, and V are the number of formula units per unit cell, the mass of the formula unit, and the unit-cell volume (in

Å^3), respectively[4-7]. The advantages of the Rietveld method are:

- The calibration constants are computed from simple literature data, i.e., *Z*, *M*, and *V* values, rather than by laborious experimentation.
- All reflections in the pattern are explicitly included, irrespective of overlap.
- The background is better defined since a continuous function is fitted to the whole powder diffraction pattern.
- The preferred orientation effects can be corrected and determined[1, 8].
- The crystal structural and peak profile parameter scan can be refined as part of the same analysis.

In this article, the method developed by Sitepu et al. (2018)[2] and Al-Ghamdi and Sitepu (2018)[3] was extended to the deposits collected from the boiler equipment, which consists of a furnace, boiler tubes, steam drum, mud drum, and the boiler, and therefore when the furnace produces heat for the boiler, the water in it changes into steam. The failure of boiler tubes mainly occurred due to the accumulated deposits in the equipment in refineries and gas plants, and ultimately slowed down the production. Therefore, the field engineers requested the authors to identify the nature and source of the XRD data of deposits by using the High Score Plus software (X'Pert High Score Plus Version 3.0e PANalytical Inc.)[9], combined with the International Powder Diffraction Data (ICDD) of the powder diffraction file (PDF-4+) database of the standard reference materials. Additionally, the authors provide the findings and support to the plant engineers, to take proper action to prevent future occurrences, thereby avoiding a plant slowdown that could result in loss of production.

The main objective of the present study was to extend the new method developed[2, 3, 10] to particularly and accurately examine the phase identification of inorganic materials (non-soluble or non-hydrocarbon) — found in different pieces of equipment at refineries and gas plants — using the High Score Plus software. Additionally, the authors determined the nature, source and formation mechanism of deposits formed in the boilers of refineries and gas plants. Once all the phases for each of the unknown inorganic deposits' XRD data had successfully been identified using the High Score Plus software, then the quantitative phase analysis of XRD data for each phase was determined using the Rietveld method with the generalized spherical harmonic description[1, 8]. The findings will help refinery and gas plant employees take proper action to prevent future occurrences.

EXPERIMENTAL PROCEDURE

The limitation of the method[2] of sample preparation procedures was extended to characterize the inorganic materials present in the sludge deposit samples, received from many different equipment items, located in refineries and gas plants. Table 1 shows the description of the samples investigated in this study. A prerequisite is the accurate phase identification and quantification results of inorganic materials or the insoluble parts. The phase composition is required to facilitate chemical cleaning of the particular failed equipment, and to prevent reoccurrence.

The very tiny amount of the inorganic materials (i.e., non-hydrocarbon part) were manually ground by an agate mortar and a pestle for several minutes to achieve a fine particle size[10], and mounted into the XRD sample holders by front pressing. Subsequently, high-resolution XRD data of the inorganic

Sample	Sludge Deposits Collected from	Use of Sitepu et al. (2018)[2] Method of Sample Preparation Procedures	Why are the Phase Compositions Required?
RAG-HS-1	Scale deposits in the form of natural carbonate scale (calcite-$CaCO_3$) from a gas plant	The starting scale and corrosion deposits were manually ground in an agate mortar and a pestle for several minutes to achieve fine particle size. Then, the fine scale and corrosion deposits were mounted into the XRD sample holder by front pressing.	Knowing which phases were involved in the deposits, can guide the field engineers to determine the source of materials found in the suction strainer, and identify the root cause of repetitive pump trips.
RAG-HS-2	• External surface of the boiler tubes at gas plant	The deposits were treated with dichloromethane, and then filtered in the filtration assembly. The insoluble part, i.e., inorganic materials or non-hydrocarbon, was analyzed by advanced XRD and the Rietveld method.	
RAG-HS-3	• Inside screen of section of boiler tube in refinery		
RAG-HS-4	• Screen tube and a condenser at gas plant		
RAG-HS-5	• A condenser at a gas plant		

Table 1. The description of the deposits investigated in this study

materials were measured using the Rigaku ULTIMA-IV X-ray powder diffractometer, with a copper (Cu) X-ray tube, from 10° to 120° 2Θ Bragg angles, with a step size of 0.04°, and a counting time of 1° per minute. Moreover, all of the XRD data sets of the inorganic materials — Table 1 — were then identified by the High Score Plus software combined with the ICDD of the PDF-4+ database of the standard reference materials. The Rietveld method was used to accurately determine the phase composition (wt%) for each of the identified phases according to Eqn. 1.

RESULTS AND DISCUSSIONS

Crystal Structures and Preferred Orientations Refinement of XRD Data of Carbonate Scale Deposits

The refined structural parameters obtained from the Rietveld refinement agreed well with the single crystal XRD data results and powder XRD results for calcite-$CaCO_3$. The space group used was R-3c (No. 167). Wyckoff coordinates: 6(c) are 0,0,0, and 0,0,½; 6(a) are 0,0,¾; and 18(e) are x,0,¼; -x,-x,¼; -x,0,¾; 0,-x,¾, and x,x,¾. Cell formula unit Z = 6 and formula weight = 100.09. Details of the referenced cell parameters are given.

Table 2 depicts the unit-cell parameters of the carbonate scale, in the form of calcium carbonate (calcite-$CaCO_3$), obtained from the Rietveld refinement with the generalized spherical harmonics description. The number parentheses give the estimated standard uncertainty for the least significant figure of the parameter. The refined structural parameters, including the unit-cell, agreed well with the corresponding single crystal XRD and powder XRD results for calcite-$CaCO_3$[11, 13], which indicates that the Rietveld refinement yields the reproducibility of the structural and quantitative analysis results. Therefore, the generalized spherical harmonics description[15-20] is recommended for the preferred orientation correction in XRD analysis, for both crystal structure refinement and phase composition analysis.

Figure 1 shows the agreement between the calculated and measured XRD pattern for the carbonate scale, in the form of calcite-$CaCO_3$, following Rietveld refinement with the generalized spherical harmonic description. Figure 2 shows the plots of the pole density distribution function, with an orientation angle derived from the Rietveld refinement with the generalized spherical harmonic description[15-20], where the pole density distribution function for <104> calcite data was derived from the Rietveld refinement. In the case of an ideal random orientation, the pole density distribution function is unity. As expected for the XRD data for the carbonate scale deposits with the refined texture index, J = 1.0854(7), which is not randomly oriented, the pole density distribution function is maximum at the orientation angle Ψ = 0° and minimum at Ψ = 90°. Shown in Table 3 are the refined parameters figures-of-merit (R_P, R_{WP}, $R(F^2)$, and goodness-of-fit index (χ^2)) obtained from the Rietveld refinement, with the generalized spherical harmonic description, which are R_P = 9.75, R_{WP} = 13.30, $R(F^2)$ = 10.15, χ^2 = 1.32; and the texture index is 1.0854(7).

Knowing accurate quantitative analysis results for each phase

Parameters	This Study	Maslen et al. (1995)[11]	Sitepu et al. (2005)[8]	Markgraf and Reeder (1985)[13]	Antao et al. (2008)[12]	Balirano et al. (1995)[14]
a (Å)	4.97630(15)	4.988(2)	4.991(1)	4.988(1)	4.9877648(1)	4.98879(7)
c (Å)	17.0904(9)	17.068(2)	17.068(2)	17.061(1)	17.05242(2)	17.0649(4)
V (Å)^3	366.520(31)	367.8(3)	368.204(2)	367.6(1)	367.3911(4)	367.81(1)

Table 2. Summary of the refined cell parameters of carbonate scale in the form of $CaCO_3$ obtained from the Rietveld refinement with a generalized spherical harmonics description for preferred orientation correction. The reference cell parameters are included.

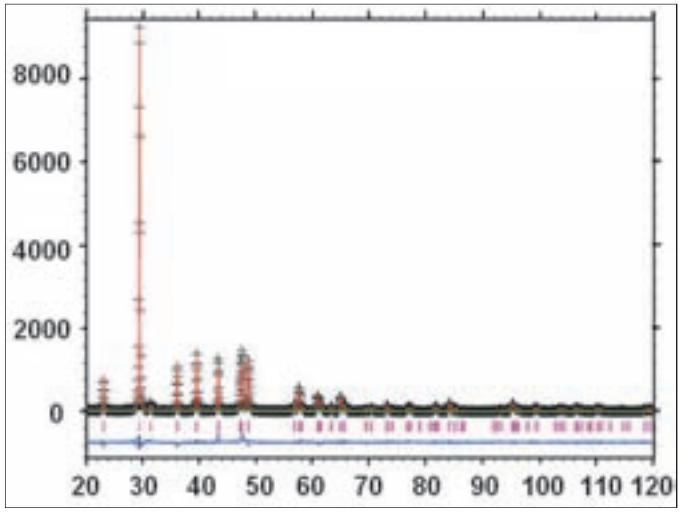

Fig. 1. The agreement between the calculated and measured XRD patterns for the carbonate scale deposits following the Rietveld refinement, with the generalized spherical harmonics description for preferred orientation correction.

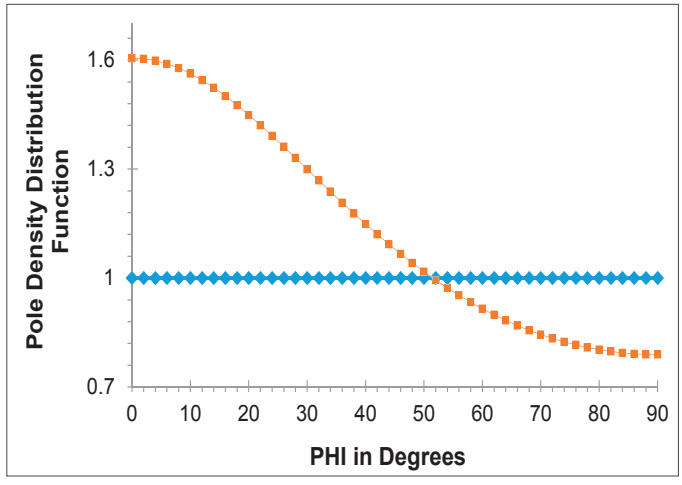

Fig. 2. The variation of the pole axial distribution function with the orientation angle. The assumed preferred orientation direction for calcite was <104>. The pole axial distribution plot for (104) calcite data derived from the Rietveld refinement with generalized spherical harmonic description.

Atomic Positions	This Study	Maslen et al. (1995)[11]	Sitepu et al. (2005)[8]	Markgraf and Reeder (1985)[13]	Antao et al. (2008)[12]	Balirano et al. (1995)[14]
Atomic Positions and Anisotropic Displacement Coefficients						
Ca(0,0,0) U_{iso}	0.0162(5)	0.00988(3)	0.232(2)	0.94(3)	0.80(4)	1.203(4)
C(0,0,¼) U_{iso}	0.0110(16)	00834(9)	0.232(2)	0.93(5)	0.76(6)	1.644(2)
O(x,0,¼) x U_{iso}	0.2544(4) 0.0247(9)	0.25700(6) 0.01129(7)	0.257(9) 0.309(8)	0.2567(2) 1.51(4)	0.250(1) 1.44(6)	0.2564(9) 1.644(2)
Bond Length						
Ca-O	—	—	2.379(1)	2.3595(5)	2.3574(2)	2.3608(7)
C-O	—	—	1.248(2)	1.280(1)	1.2836(3)	1.279(1)
Crystallographic Figures-of-Merit and Goodness-of-Fit Index						
R_P	9.75	—	12.13	—	—	—
R_{WP}	13.30	—	17.45	—	—	—
$R(F^2)$	10.15	—	—	—	—	—
χ^2	1.32	—	2.780	—	—	—
J	1.0854(7)	—	1.0531(4)	—	—	—

Table 3. Summary of the refined atomic positions of carbonate scale in the form of $CaCO_3$, obtained from Rietveld refinement with the generalized spherical harmonics description model

involved in the scale deposits, facilitates chemical cleaning and prevents reoccurrence by stopping the generation of those particular deposits.

Deposits Collected from the External Surface of the Boiler Tubes in a Refinery

The phase identification of the XRD data of deposits was conducted to determine the source and formation mechanism, and therefore, the phase composition for each of the identified phase results can be used by the engineers to take corrective measures, prevent scale build up, and avoid future tube failure.

Figure 3 shows the phase composition of the identified results obtained from the Rietveld refinement for each of the identified phases of XRD data of ash deposits from the external surface of the boiler tubes in a refinery, where the refinery boiler is an oil fired boiler. The quantitative phase analysis results showed that the sample contained 70 wt% of vanadium oxide (V_2O_5), 15 wt% of sodium vanadium oxide (NaV_2O_5), 13 wt% of sodium vanadium sulfate hydrate [$Na_2V(SO_4)_{2x}H_2O$], and 2 wt% mackinawite (FeS).

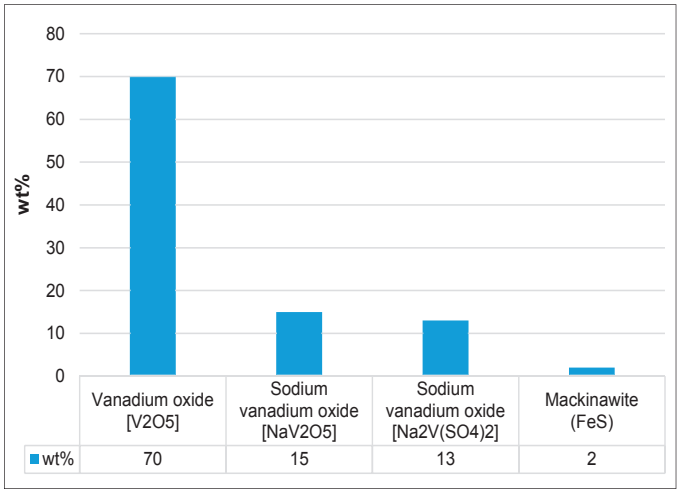

Fig. 3. Rietveld phase analysis of XRD data of ash deposits collected from the external surface of the boiler tubes in the refinery.

The findings suggest that when fuel oil is burned, approximately all of the vanadium and sodium compounds present in the fuel — in high quantities — react with oxygen to form V_2O_5 and Na_2O in the furnace and stick to the metal surface. When the two formed compounds react on the metal surface, it formed a low melting phase — sodium vanadate. Under the optimum conditions, both V_2O_5 and Na_2O can form a liquid that flux the protective oxide scale, exposing the underlying metal to oxidation, and therefore, the ash deposits build up in the boiler tubes in a refinery, and can pose potential corrosion problems.

Additionally, when the NaV_2O_5 appeared in the ash deposits in the boiler tubes of a refinery, fuel ash corrosion occurred. Fuel oils contain low quantities of vanadium, where sodium and sulfur was used to mitigate fuel ash corrosion. The other options to prevent the formation of a low melting point phase of the sodium vanadate complexes is by adopting a fuel additive treatment. The study suggests that in controlling fuel ash corrosion, additives containing magnesium and aluminum oxide have successfully been used.

Scale Deposits Collected from the Screen of a Section Cutout, and Inside a Large Boiler Tube from a Refinery

The phase composition analysis of the scale deposits from the inside screen of a section cutout and inside a large boiler tube from a refinery, which were observed in high-pressure boiler tubes at the refinery, was mainly required to identify the deposits present inside of the tube. The identification of the deposits helped to design a procedure for chemical cleaning without damaging the boiler tubes.

The Rietveld phase analysis of the scale deposits scraped from the insides of the tubes, mainly consisted of 75 wt% of iron oxide corrosion products, in the form of 41 wt% magnetite (Fe_3O_4) and 34 wt% hematite (Fe_2O_3), with an additional 13 wt% of calcium phosphate hydroxide (apatite), and 12 wt% of magnesium phosphate hydroxide for the scale deposits from the inside screen of the section cutout, Fig. 4a.

Additionally, the phase composition analysis of the scale deposits from inside a large boiler tube from a refinery, Fig. 4b, revealed that the sample contained 74 wt% of iron oxide corrosion products, in the form of 60 wt% of magnetite (Fe_3O_4) and 14 wt% of hematite (Fe_2O_3), with an additional 11 wt% of calcium phosphate hydroxide (apatite), and 15 wt% of magnesium phosphate hydroxide. Note that iron oxide corrosion products in the form of 34 wt% of Fe_2O_3 for scale deposits from inside a large boiler tube, and 14 wt% of Fe_2O_3 for the scale deposits from inside a large boiler tube, suggests the presence of dissolved oxygen in the boiler water.

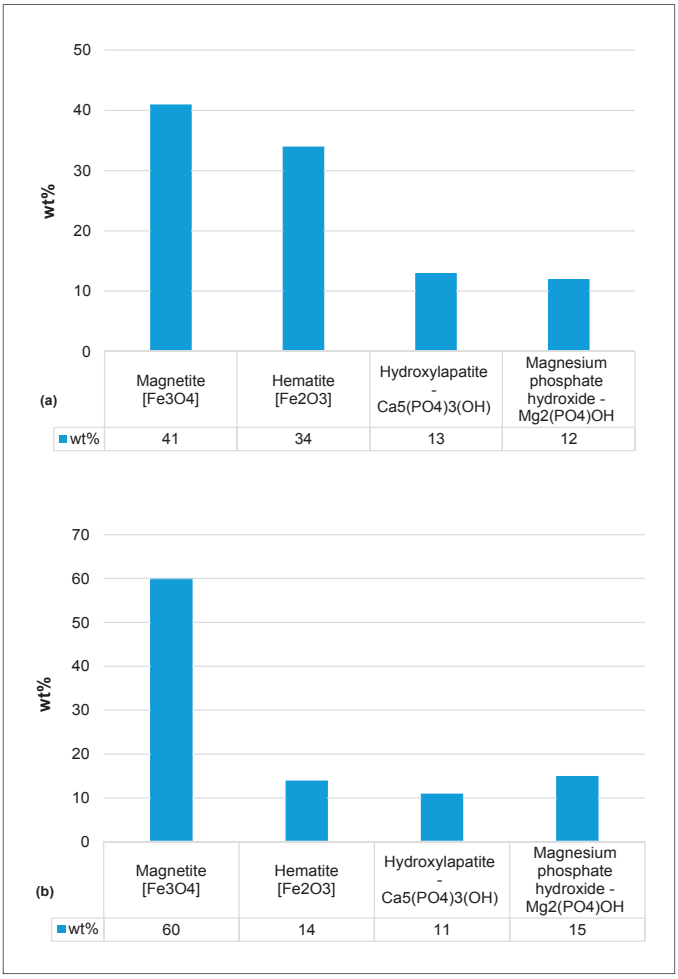

Fig. 4. Rietveld phase composition results of the scale deposits from: (a) inside the screen of a section cutout, and (b) inside a large boiler tube from a refinery.

Deposits Collected from Screen Tubes of the Boiler and Condenser at a Gas Plant

The boiler tube failed due to the built up deposits, and therefore, the phase composition results were required by the field engineers to support their failure analysis work. Figure 5 shows the phase composition results for each of the identified phases obtained from the Rietveld refinement. The Rietveld phase analysis revealed that the deposits from screen tubes of a boiler and a condenser at the gas plant, mainly consisted of 74 wt% of iron oxide corrosion products, in the form of magnetite (Fe_2O_3) and metallic hematite (Fe_2O_3), with the addition of 26 wt% of Cu. Note that the high wt% of Fe_2O_3 and Cu indicate the presence of dissolved oxygen in the boiler feedwater, and also erosion in the boiler tubes.

Scale Deposits Produced with a Sulfur Product from a Condenser at a Gas Plant

The main objective of the deposits investigated by XRD data and the Rietveld method, was to support the field engineers. Note that the field engineers were concerned that the unknown deposits produced with a sulfur product from a condenser at a gas plant might be coming from the alumina and silica of the super claus catalyst. If the XRD phase identification results showed the deposits consist of alumina and silica, it suggested that the mesh holding the catalyst has a pinhole, and therefore, the catalyst leaks will definitely require a total shut down of the gas plant, and the repair and removal of the catalysts.

Figure 6 shows the Rietveld phase analysis results for each of the identified phases, obtained from the Rietveld refinement of the XRD data of the unknown deposits, which were produced with a sulfur product from a condenser at a gas plant.

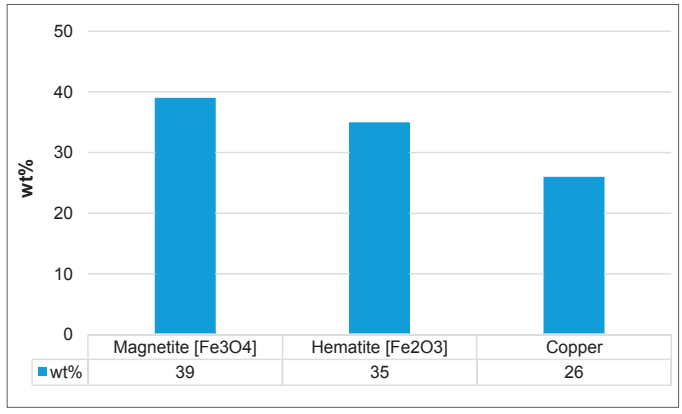

Fig. 5. Rietveld phase analysis results of the deposits from the screen tubes of a boiler and a condenser at the gas plant.

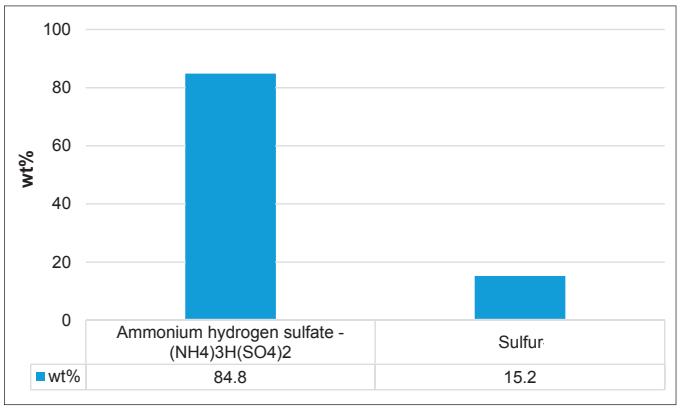

Fig. 6. Rietveld phase analysis results of the unknown deposits produced with a sulfur product from a condenser at a gas plant.

The results revealed that the deposits mainly consisted of 84.8 wt% of ammonium hydrogen sulfate [$(NH_4)_3H(SO_4)_2$] and 15.2 wt% of sulfur (S). The findings show that no alumina or silica appeared in the deposits, suggesting that the mesh holding the catalyst is good. Due to the treatment with chemical containing ammonia, the [$(NH_4)_3H(SO_4)_2$] could be formed in the boiler feedwater. The formation of [$(NH_4)_3H(SO_4)_2$] can be avoided by increasing the furnace temperature that will burn ammonia.

It can be summarized that phase identification of the XRD data of the deposits obtained from the High Score Plus software, and phase composition for each of the identified phases obtained from the Rietveld refinement are excellent tools to determine the nature, source, and formation mechanism of deposits formed by the processes in the various units of refineries and gas plants. Therefore, the results guided the engineers at the refineries and gas plants to overcome problems by designing the chemical cleaning procedures that will not damage the equipment and avoid future equipment failure.

CONCLUSIONS

Based on the structure, texture and phase composition of the XRD data of the deposits, obtained from the Rietveld method and generalized spherical harmonic description for crystallographic preferred orientation corrections, we found the following:

- Good agreement between the measured and calculated XRD patterns of scale deposits in the form of calcium carbonate (calcite-$CaCO_3$) from boiler equipment at a gas plant; and the refined structural parameters agreed well with the XRD single crystal.
- The Rietveld phase analysis yields the reproducibility of the results for the deposits built up in the affected equipment at the refinery and gas plants, and therefore, the findings suggest that the fuel is poor if the V_2O_5, NaV_2O_5, and $Na_2V(SO_4)_2$ phases appear in the examined ash deposits. Furthermore, the boiler feedwater contains dissolved oxygen, if the corrosion product in the form of hematite (Fe_2O_3) is present in the boiler deposits.
- The presence of metallic Cu in the deposits suggests erosion in the boiler tubes, and therefore, precautions must be taken to prevent the plating out of the Cu during cleaning operations.

Knowing accurately which phases and its concentrations were involved in the deposits, can guide the field engineers at the refinery and gas plants to facilitate efficient cleaning of the effected equipment by drawing up the right procedures and taking preventive action to stop the generation of those particular deposits.

ACKNOWLEDGMENTS

The authors would like to thank the management of Saudi Aramco for their support and permission to publish this article. Thanks are also due to Yazeed Al-Dukhayyil, Mossaed A. Al-Fahad, and the R&DC/TSD/AAU professionals and technicians for their help.

REFERENCES

1. Sitepu, H.: "Texture and Structural Refinement Using Neutron Diffraction Data from Molybdite (MoO_3) and Calcite ($CaCO_3$) Powders and a Ni-rich $Ni_{50.7}Ti_{49.30}$ Alloy," *Powder Diffraction*, Vol. 24, Issue 4, December 2009, pp. 315-326.
2. Sitepu, H., Al-Ghamdi, R.A. and Zaidi, S.R.: "Corrigendum to Application of a New Method in Identifying the Sludge Deposits from Refineries and Gas Plants: A Case of Laboratory-based Study," *International Journal of Corrosion*, Vol. 2018, Article ID 8646104, 2018, 1 p.
3. Al-Ghamdi, R.A. and Sitepu, H.: "Characterization of Sludge Deposits from Refineries and Gas Plants: Prerequisite Results Requirements to Facilitate Chemical Cleaning of the Particular Equipment," *International Journal of Corrosion*, Vol. 2018, Article ID 4121506, 2018, 8 p.
4. Bish, D.L. and Howard, S.A.: "Quantitative Phase Analysis Using the Rietveld Method," *Journal of Applied Crystallography*, Vol. 21, Issue 2, April 1988, pp. 86-91.
5. Hill, R.J.: "Expanded Use of the Rietveld Method in Studies of Phase Mixtures," *Powder Diffraction*, Vol. 6, Issue 2, June 1991, pp. 74-77.
6. Hill, R.J. and Howard, C.J.: "Quantitative Phase Analysis from Neutron Powder Diffraction Data Using the Rietveld Method," *Journal of Applied Crystallography*, Vol. 20, Issue 6, December 1987, pp. 467-474.
7. O'Connor, B.H. and Raven, M.D.: "Application of the

Rietveld Refinement Procedure in Assaying Powdered Mixtures," *Powder Diffraction*, Vol. 3, Issue 1, March 1988, pp. 2-6.

8. Sitepu, H., O'Connor, B.H. and Li, D.Y.: "Comparative Evaluation of the March and Generalized Spherical Harmonic Preferred Orientation Models Using X-ray Diffraction Data for Molybdite and Calcite Powders," *Journal of Applied Crystallography*, Vol. 38, Issue 1, February 2005, pp. 158-167.
9. Degen, T., Sadki, M., Bron, E., König, U., et al.: "The High Score Suite," *Powder Diffraction*, Vol. 29, Issue S2, October 2014, pp. S13-S18.
10. Sitepu, H. and Zaidi, S.R.: "Application of a New Method in Identifying the Sludge Deposits from Refineries and Gas Plants: A Case of Laboratory-based Study," *International Journal of Corrosion*, Vol. 2017, Article ID 9047545, 2017, 7 p.
11. Maslen, E.N., Streltsov, V.A., Streltsova, N.R. and Ishizawa, N.: "Electron Density and Optical Anisotropy in Rhombohedral Carbonates. III. Synchrotron X-ray Studies of $CaCO_3$, $MgCO_3$, and $MnCO_3$," *Acta Crystallographica, Section B, Structural Science,* Vol. 51, Issue 6, December 1995, pp. 929-939.
12. Antao, S.M., Hassan, I., Wang, J., Lee, L.P., et al.: "State-of-the-Art High-Resolution Powder X-ray Diffraction (HRPXRD) Illustrated with Rietveld Structure Refinement of Quartz, Sodalite, Tremolite, and Meionite," *The Canadian Mineralogist,* Vol. 46, Issue 6, December 2008, pp. 1501-1509.
13. Markgraf, S.A. and Reeder, R.J.: "High Temperature Structure Refinements of Calcite and Magnesite," *American Mineralogist*, Vol. 70, Issues 5-6, June 1985, pp. 590-600.
14. Ballirano, P., Maras, A., Caminiti, R. and Sadun, C.: "Carbonate-Cancrinite: In Situ Real-time Thermal Processes Studied by Means of Energy Dispersive X-ray Powder Diffractometry," *Powder Diffraction*, Vol. 10, Issue 3, September 1995, pp. 173-177.
15. Von Dreele, R.B.: "Quantitative Texture Analysis by Rietveld Refinement," *Journal of Applied Crystallography*, Vol. 30, Issue 4, August 1997, pp. 517-525.
16. Sitepu, H.: "Assessment of Preferred Orientation with Neutron Powder Diffraction Data," *Journal of Applied Crystallography*, Vol. 35, Issue 2, April 2002, pp. 274-277.
17. Larson, A.C. and Von Dreele, R.B.: "General Structure Analysis System (GSAS)," *Los Alamos National Laboratory Report LAUR 86-748*, 2004, 231 p.
18. Sitepu, H., Prask, H.J. and Vaudin, M.D.: "Texture Characterization in X-ray and Neutron Powder Diffraction Data Using the Generalized Spherical-Harmonic," *Advances in X-ray Analysis*, Vol. 44, January 2001, pp. 241-246.
19. Sitepu, H.: "Use of Synchrotron Diffraction Data for Describing Crystal Structure and Crystallographic Phase Analysis of R-Phase NiTi Shape Memory Alloy," *Textures and Microstructures*, Vol. 35, Issues 3-4, 2003, pp. 185-195.
20. Sitepu, H., Schmahl, W.W. and Von Dreele, R.B.: "Use of the Generalized Spherical Harmonic Model for Describing Crystallographic Texture in Polycrystalline NiTi Shape-Memory Alloy with Time-of-Flight Neutron Powder Diffraction Data," *Applied Physics A*, Vol. 74, Supplement 1, December 2002, pp. S1676-S1678.

BIOGRAPHIES

Rasha A. Al-Ghamdi joined the Technical Services Division of Saudi Aramco's Research and Development Center (R&DC) in July 2016. Since then, she has gained extensive experience in materials characterizations related to the company needs, i.e., materials characterization of nano-zeolite catalysts, nano-bentonites, cements, barite, corrosion products, and rocks using the X-ray fluorescence (XRF), X-ray powder diffraction (XRD), and Rietveld method. Rasha has developed five new methods to determine the Si/Al ratio, crystallinity percentage and crystallite size and microstrain of the synthesized zeolite-Y and zeolite-beta catalysts; which have successfully and continuously been used at the R&DC.

She recently filed a patent as co-inventor, on the Si/Al ratio of the synthesized zeolite catalysts, which aligns with the high throughput analysis.

Rasha has published two peer-reviewed articles in the *International Journal of Corrosion*, and two peer-reviewed articles in the *International Journal of Research in Engineering & Technology*, and in the *American Journal of Materials Synthesis and Processing*. Also, she has published more than 10 papers at the GCC conferences, and Denver X-ray Conference proceedings.

In 2010, Rasha received her B.S. degree in Chemistry from King Faisal University, Dammam, Saudi Arabia, and in 2014, she received her M.S. degree in Nanotechnology from Flinders University, Adelaide, South Australia.

Rasha is a member of the International Center for Diffraction Data (ICDD) organization.

Dr. Husin Sitepu joined the Technical Services Division of Saudi Aramco's Research and Development Center (R&DC) in late December 2008. Since then, he has contributed to six ongoing research projects by providing crystallographic information file (CIF) data on synthesized zeolite catalysts. Husin also analyzed the crystal structure and texture refinement of new materials by using the General Structure Analysis System (GSAS) Rietveld software. Before joining Saudi Aramco, Husin worked at national and international research laboratories in the U.S. (National Institute of Standards and Technology, and Virginia Tech), Germany (Ruhr-University Bochum), France (Institut Laue-Langevin), Canada (University of British Columbia), and Australia (Curtin University). Since 1989, he has gained extensive experience in the Rietveld refinement of polycrystalline structures using powder X-ray diffraction, synchrotron diffraction, and neutron diffraction data.

Since 1989, Husin has published 47 papers in peer-reviewed journals, including the International Union of Crystallography's *Journal of Applied Crystallography*, the *Powder Diffraction Journal*, and *American Mineralogist* with the Herfindahl Index of 12. Also, he has published nine papers in the *Saudi Aramco Journal of Technology*, six papers with the National Association of Corrosion Engineers, and presented 88 papers at various conferences. Husin has a very strong background in physics at a research level, and he is an expert in crystallography preferred orientation and diffraction science through his extensive experience in Rietveld refinement of polycrystalline structures using powder X-ray, synchrotron and neutron diffraction data.

Husin received his Postgraduate Diploma and his M.S. and Ph.D. degrees in Physics from Curtin University, Perth, Western Australia, in 1989, 1991, and 1998, respectively.

He is a member of the International Center for Diffraction Data (ICDD), the International Union of Crystallography (IUCr), and the Neutron Scattering Society of America (NSSA).

Optimization Study of Temperature Log for Fracture Height Evaluation and Field Application of Practical Examples after Pad Calibration

Adrian Buenrostro, Mohammed Al-Abdrabalnabi, Amro E. Mukhles, and Saad M. Al-Driweesh

ABSTRACT

This article describes the analysis of a high-resolution temperature (HRT) log study; after multiple field HRT logs were made to investigate fracture height development, the log analysis was made once crosslinked gel was pumped to calibrate injection of fluid in the formation under fracturing conditions. The study set the criteria to validate fracture height to avoid the necessity of temperature logs, based on data interpretation of the logs' and wells' correlations. This process is designed to be made prior to injection at the reservoir; if injection is found effective, the fracture design can be arranged with higher certainties on fracture height value. The cases of study were made at a conventional onshore sandstone reservoir.

INTRODUCTION

Fracturing is a complex technique utilized to stimulate hydrocarbon reservoirs to enhance their production. The theory, tools, and techniques utilized for fracturing are complex and very specific. With the demanding increase of hydrocarbon production, proppant and acid fracturing are widely implemented, and in some cases, is the unique solution to having commercial production, i.e., unconventional gas reservoirs.

The optimization of the fracturing process is important since this activity is complex, expensive, and in most of the cases, required for commercial production. Several parts of the process are known based on previous experiences. In other cases, complex studies still need to be done to better understand each case, to enable a more accurate propped fracturing execution. To be confident in the case of design, execution and evaluation of a proppant fracturing job, fracture geometry determination is very important, as this drives the adequate evaluation and job execution while also allowing for job optimization. One of the basic and most important values to estimate the fracture geometry is the fracture height; once this parameter is determined, fracture width and fracture length can be determined with less uncertainty, based on other parameters from log data, job execution, etc. The fracture geometry can be estimated more confidently if the fracture height value is set.

This article studied and compared multiple scenarios of sandstone reservoirs. The study was made for fracturing jobs focused on gas and hydrocarbon production. Tight conditions and unconsolidated sandstones were dominant scenarios of the fracture jobs. The parameters utilized for this study were focused on some log signatures, which were observed to drive the criteria of the fracture height growth. Based on those parameters, the project attempts to simplify the process of fracture height determination. The exercise was made for a group of wells in different areas of the reservoirs where some parameters prevail, and we are confident in the gathered information. The signatures observed proved helpful to confidently predict the expected fracture height. In the exercise of this project, all the examples were made with cases where the temperature log was made after reading the fracture data of the obtained fracture height by the temperature log criteria[1].

ANTECEDENTS

This project was made in wells that produced outstanding gas rates from its reservoirs over a period of decades. Stimulation by proppant fracturing at the sandstone reservoirs become a regular requirement to find commercial production after new areas were attempted for production. The process of proppant

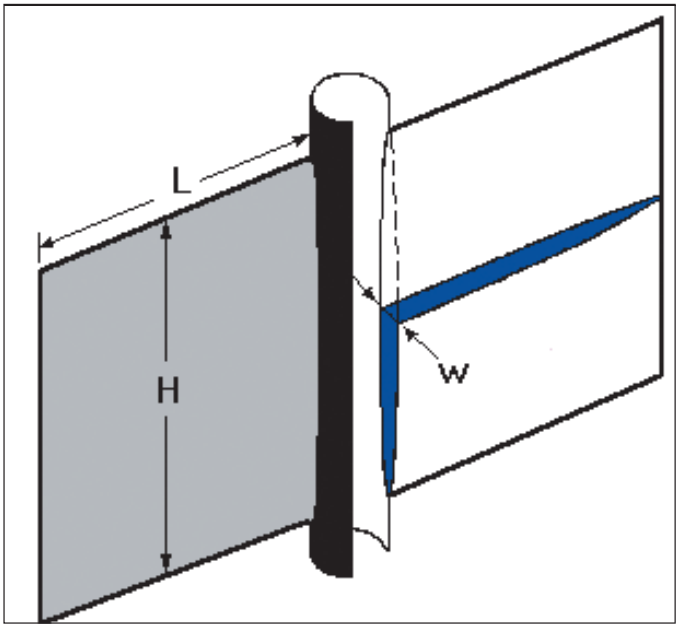

Fig. 1. General dimensions of a fracture geometry.

fracturing started with multiple uncertainties from the reservoir point of view, and also for the logistic part at the job execution as fracturing was not previously used.

The regular fracturing startup process involves reservoir logging evaluation, injection test, completion hardware setup, software simulations, and lab tests for compatibility, and forecast studies for production results, among other challenges. Specific studies and tests were conducted in preparation to the first field applications. During the startup process, it was observed that a wide range of parameters need to be clarified prior to deploying the stimulation in the field.

Figure 1 shows the parameters used for a fracture geometry in a generic way, simplified to have the total length, height, and width, represent a volume. In real cases, a fracture is not a geometrically perfect square or rectangle; but to simplify equations and analysis, computational models assume simplified shapes of fracture geometry for processing calculations.

In general, for a fracture geometry determination for the three main dimensions; the length (L in Fig. 1, or "d" in Table 1), width (W), and height (H), are based on:

- The amount of energy placed (pressure while pumping and pumping rate).
- The amount of mass used (fluids + proppant).
- The amount of energy dissipated (fluid efficiency and pressure variations).

	"d"	W (width)
Perkins and Kern	H	$(\mu QL/E')^{1/4}$
Radial	L	$(\mu QR/E')^{1/4}$
Gertsma deKlerk	R (radius)	$(\mu QL^2/E'H)^{1/4}$

Table 1. Fracture Geometry Model's to calculate the main dimensions

Fluid efficiency is related to the fluid amount pumped, the amount lost in fracture geometry to the formation due to leak-off, and the fluid effectively creating a fracture geometry.

Note that in Fig. 1, the length is only for one fracture wing, as the fracture is assumed to develop symmetrically — the same geometry on both sides from the wellbore to the formation. The fracture volume and geometry is standard, referring only to one wing or side of the fracture.

Width, according to fracture geometry calculation equations, is based in different models of the fracture, and is directly related to[2]:

$$E' = \frac{E}{1-\nu^2} \quad (1)$$

where H = frac height, L = frac length, R = radial growth, μ = viscosity of fluid, Q = pumping rate, E' = plain strain modulus, E = Young's modulus, and ν = Poison's ratio.

The fracture width can be calculated in general by:

$$w \propto \left[\frac{Q\mu L}{E'}\right]^{1/4} \quad (2)$$

Following Fig. 1 and Table 1, and Eqns. 1 and 2, it is observed that the width is driven by Q, μ, L, and formation mechanical parameters.

This concept is a simplified way to calculate the fracture

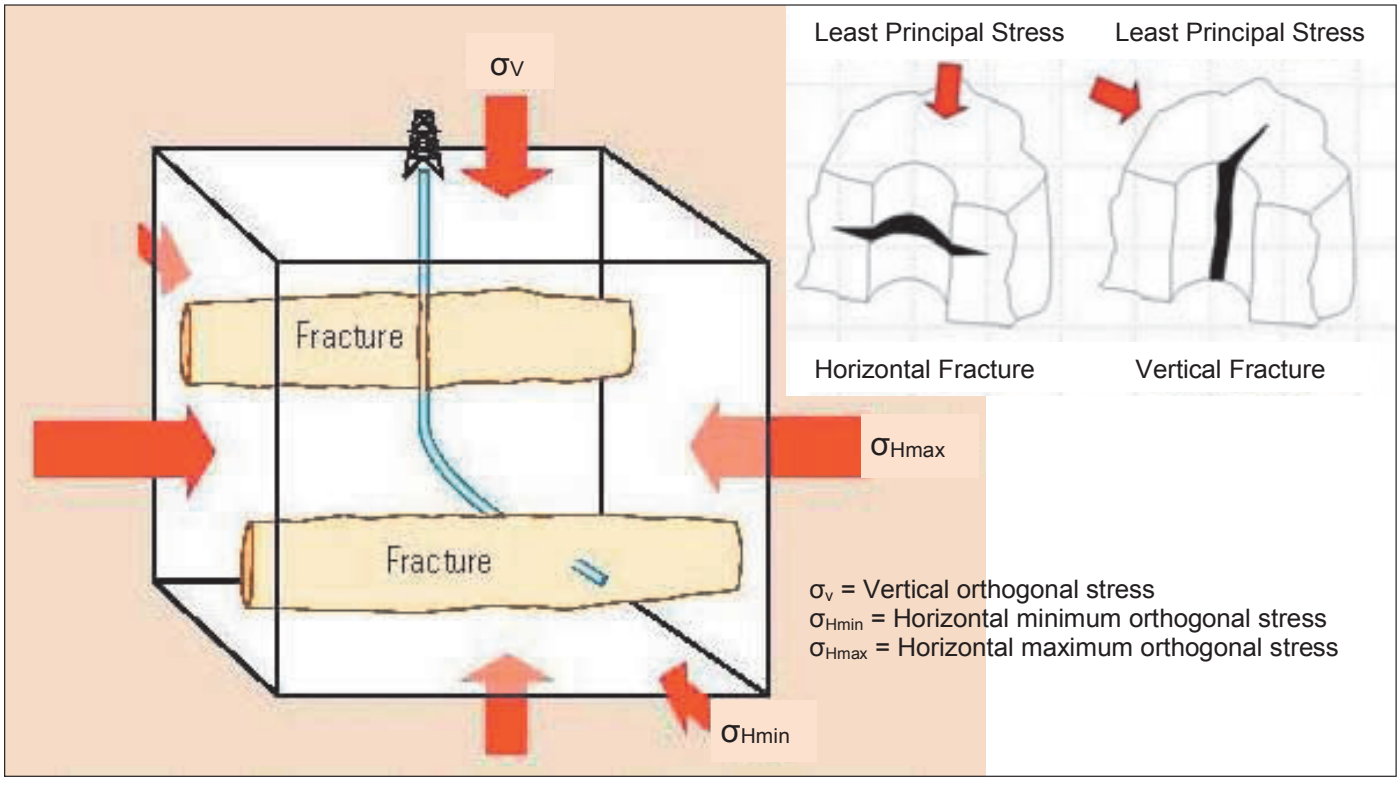

Fig. 2. Fracture geometry development from the wellbore related to the formation stress orientation, which can be either vertical or horizontal.

width in correlation to a general fracture model, whereas other parameters, i.e., pumping pressure, net developed pressure, and leakoff, among others, may affect the fracture's width.

As previously mentioned, the three main dimensions, length, width, and height, are simplified for the analysis made to calculate them to obtain the fracture geometry. Since there are three main variables for one model, the definition of any of those three values simplifies the calculation of the other two dimensions. Therefore, when there is a chance to measure any of those parameters, the fracture geometry can be determined more confidently.

It is possible for the fracture length and width to drastically vary, depending on the fracture height determination; whereas once one value is determined, fracture optimization is feasible. Additional technologies can be used to measure the width and fracture length. Those technologies are usually complex and present multiple concerns; as some can have limitations and logistic issues due to their particular requirements, which means that the implementation of them is then not always possible. Fracture height in another way is easy to measure when the fracture plane is collinear to the wellbore, which commonly is the case of vertical wells, where most of the geomechanical conditions of the reservoirs place the wellbore collinear with the fracture plane, Fig. 2. The natural arrangement of the main stress orientations in the reservoirs make a vertical wellbore suitable for developing a vertical fracture plan, thereby making the fracture height collinear with the wellbore[3].

The characteristic of a vertical well, being collinear with the minimum in situ stress of the rock, allows the fracture created to develop its height attached to the wellbore from the top to bottom height of the fracture. An important temperature contrast is generated from the fluid injected in the formation at the depth where the fracture is placed — at perforations made on the wellbore. The reservoir is usually dozens of degrees hotter than the injected fluids. The change in temperature is made by the fluids pumped into the formation, which starts cooling down the well from the surface, the wellbore completion, and finally reaching the reservoir.

Equation 3 describes the parameters used to analyze the temperature change according to thermodynamics by three ways: conduction, convection, and radiation, Fig. 3. Conduction is the most important for the case of heat exchange in the formation between the rock, completion tubulars, and fluid injected during a fracture job.

$$Q/t \propto kA(T_{Hot} - T_{Cold}) ; \quad (3)$$

where Q = energy (W), t = time(s), k = heat transfer coefficient [W/((m^2)(°C))], A = heat transfer area (m^2), T_{Hot} = temperature of the hot mass (°C), and T_{Cold} = temperature of the cold mass (°C).

FIELD CASE APPLICATION

For the case of a fracture geometry investigation, fluid is pumped from the surface (bullheading) through the wellbore completion to the formation. Fluid is pumped at surface temperature, around 20 °C to 25 °C. The formation rock where the fracture is being made is several degrees hotter, and dissipation of the temperature will be driven by reservoir conditions — depth, reservoir fluids, and rock type, among others. A reservoir at around 4,000 m deep will have approximate temperatures of 150 °C to 180 °C. The difference from the reservoir temperature with the injected fluid generates an important cool-down at the area of injection where the fracture is generated. This temperature contrast dissipates with time, and depends on formation properties to accelerate or restrict the temperature to cool-down or heat up. Usually, after several hours — 6 to 12 hours — a temperature contrast can be measured from the wellbore to the formation.

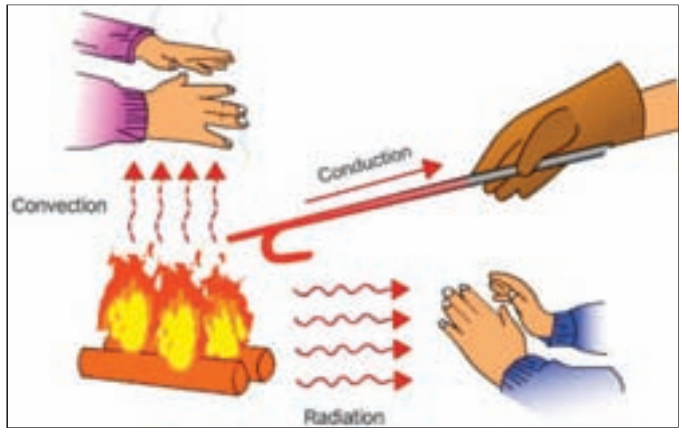

Fig. 3. General heat transfer paths by conduction, convection, and radiation.

During the process of a proppant fracture job for the study, injected cold fracturing fluid is usually no less than 50 m^3 of base water fluid, injected into the rock, which is a porous media filled with gas, oil and/or water. The process is made in as high a rate as possible to fracture the formation under controlled parameters. The pumping rate used is from 3 m^3/min to 7 m^3/min, therefore, the fluid is injected in 10 to 15 minutes. Quick injection allows for a higher temperature contrast at the core of the injection point, which decreases with distance from that point, until a distance where original reservoir conditions (temperature) are not disturbed because no fluid reaches that point. Figure 4 shows the reservoir depth, when the fracture plane is collinear with the wellbore, it can be interpreted based on the temperature profile contrast observed on the readings of a log made with high-resolution readings, i.e., a high-resolution temperature (HRT) log.

Figure 4 represents a logging job, where tools are placed into the wellbore by running in hole (RIH), and recording the temperature changes. As observed in the left log plotted lines, there are two continuous lines, thick and thin — each one close to a dashed line — the dashed line in each case is straight, and used as a reference to the perfect incremental profile of the temperature for this log case. The continuous lines are the real temperature readings by the log in the well. They are not straight

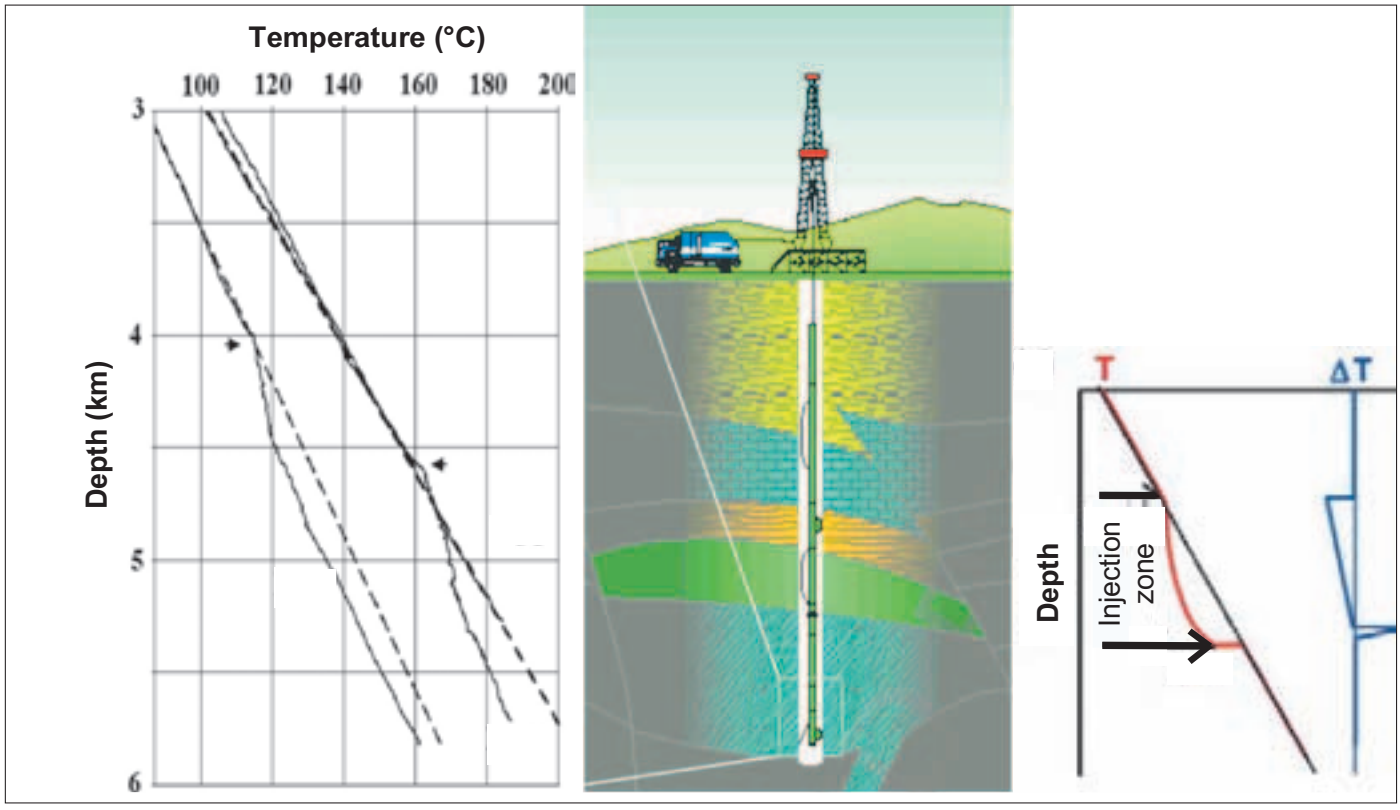

Fig. 4. Logging a well for temperature log.

as different layers on the reservoir commonly have small variations in temperature. Most of the time, temperature logs are repeated over periods of time; for particular objectives where changes on the temperature profile is expected to provide information to make decisions on well conditions.

To have a case by case reference about temperature profiles, the performance for each well was studied at initial temperature conditions. For this, an initial log was made when the well was undisturbed, at the startup of the well life; the initial log was then the base reference for comparison, so further temperature changes could be identified. Due to the disturbance of wellbore fluids, and the thermal hysteresis of the temperature log for the bottom-hole assembly, temperature readings differ if made RIH or pulling out of hole.

For a proppant fracture job, the temperature log when the well was undisturbed, is compared with the temperature log made after injection of the fluids, either for fracture evaluation or after the main fracture job, to document the final fracture height. This information was obtained by selecting the points where the temperature profile differs from the normal temperature — base line. The temperature increases as the depth increases, resulting in a deviation of temperature profile, where a cool-down is observed close to the injection point — at perforations — which suggests that the pumped fluid has invaded the reservoir at the perforation zone. The readings must be done above and below the disturbed zone of injection, where the temperature deviates from a normal trend above and below the perforations, suggesting fluid invasion related to height

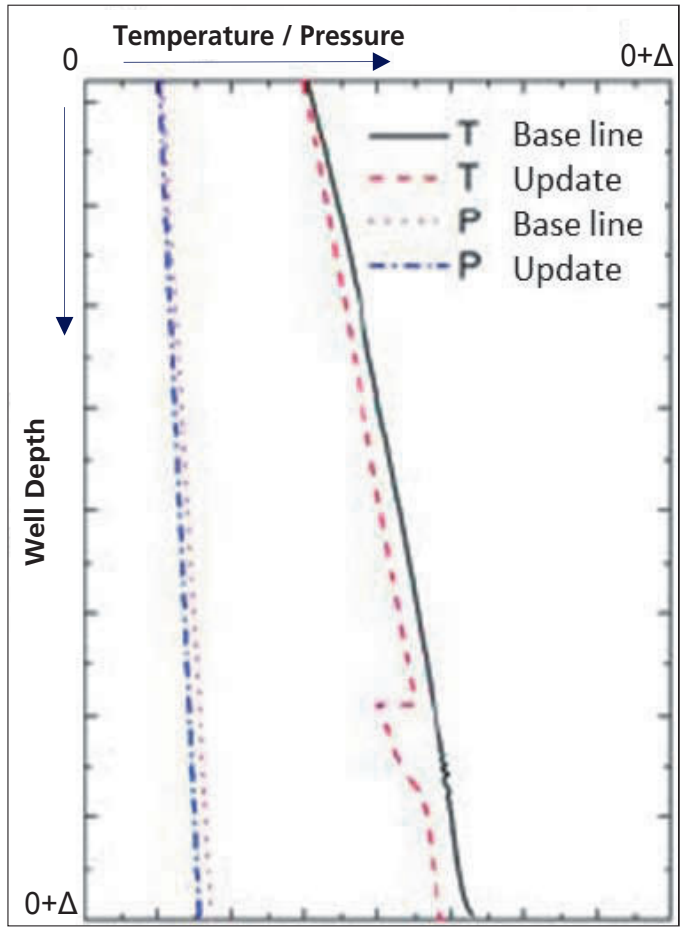

Fig. 5. Example of temperature drop at the injection zone; the temperature falls from expected undisturbed profile due to fluid recently injected.

measurement, Fig. 5. Above the perforations, the temperature has a similar slope to the original temperature log, but below the perforations where the fluid was not disturbed, only the area of fluid invasion shows a cool-down. Deeper points show undisturbed temperatures from the initial conditions. To verify the validation on readings as well as dissipation of a cool-down at the injection section, subsequent logs in specific time intervals are made. For this study, the standard time is 2 hours between readings.

The first reading should be done as soon as possible after injection. Due to logistics and the surface operation sequence of activities, usually the first temperature log is made from 4 to 6 hours after injection, Fig. 6.

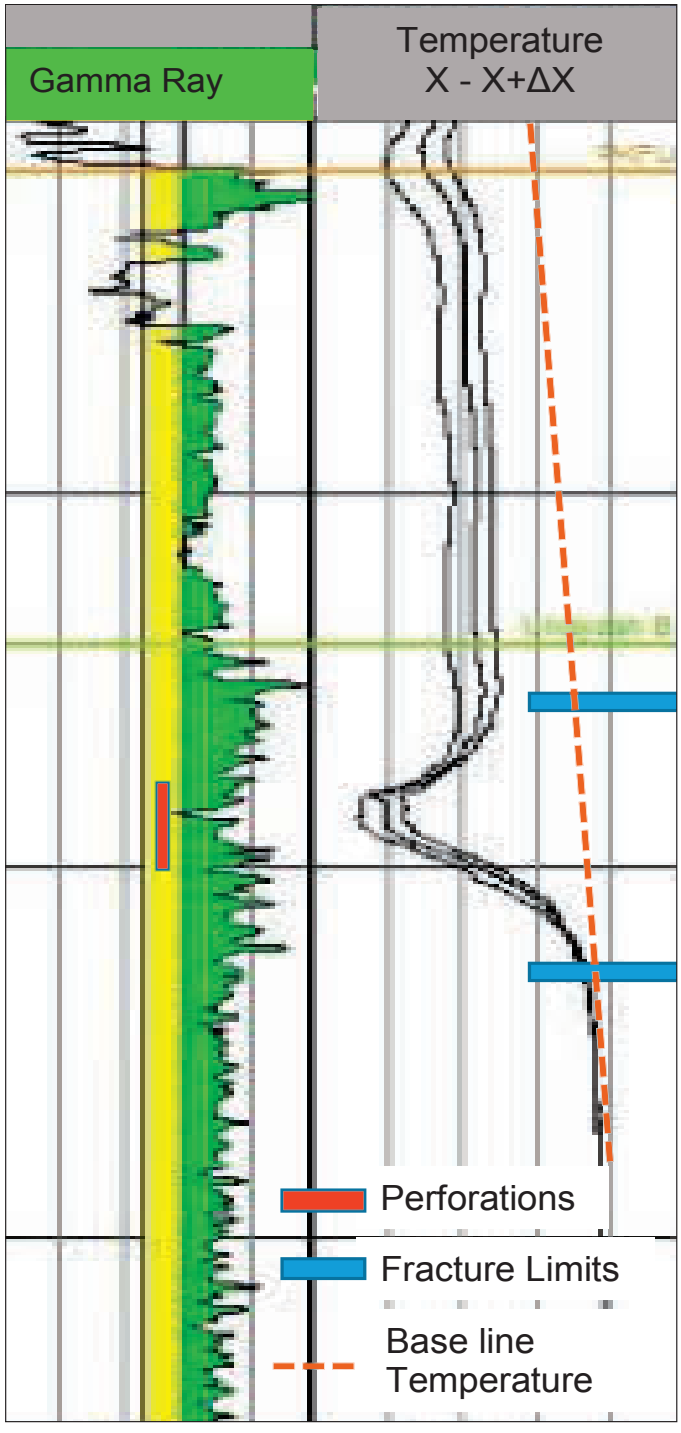

Fig. 6. Example of a temperature log after injection with time intervals for subsequent logs; base line temperature log as a reference.

Based on the temperature log, fracture height is determined and the temperature drop behavior can suggest whether or not the fracture is well contained. Some cases show the fracture height distribution to be higher above or below the perforations, or an extremely big fracture height, which usually shows a smaller temperature drop as the fluid mass is distributed over a longer area. The amount of hot rock from the reservoir in ratio to the liters of fluid injected is always major. In smaller zones where all injections are contained, more water is available to cool-down the formation rock per the height of the exposed rock; in those cases, the cool-down is more evident. When water is not well contained in the fracture, it grows or develops a larger height; as in the case where each volume of liquid is exposed to more area of contact with the formation rock, which is very hot compared to the injected fluid. Therefore, the energy of the fluid, which can influence a change in the temperature of the rock, is less than when it is exposed to a smaller rock section.

This criteria is utilized for the multiple (usually a total of three) temperature logs made to determine if with time, the rock tends to dissipate the fluid in the fracture created under a non-homogeneous profile — all lines on the temperature log becoming parallel to each other at any single depth. This case can be interpreted as the presence of a "dominant" fracture zone, which shall be considered for the fracture design and execution as the risk of fracture propagation could not be constant during the execution, increasing the chances of issues to complete the job as desired.

Note that trend variations among subsequent logs could indicate differential closure conditions at various reservoir layers related to the fracture. The interpretation of such cases is important, but is a particular topic to be covered by specific study, which is not the case for this article.

After several years and dozens of temperature logs made, the temperature logs showed mostly average behaviors on fracture geometry "height" description. So far, no more than 85 m (~275 ft) of fracture height has being identified, while also never finding a developed fracture of less than 21 m (70 ft) in height. The average fracture height in general is found to be around 33 m (120 ft), and it was observed that certain parameters on the log are usually related to the fracture height limits, suggesting those values are affecting or directly impacting the fracture height development. Based on those observations, a tracking data study over the recorded logs was made; it revealed a trend on the well logs compared to fracture geometry. The designed and post-job pressure matched fracture jobs were used and correlated to observe the trend of the fracture height, which was related to the most influential values on the logs. These values can be utilized to confidently predict the fracture height without needing a temperature log.

Among more than 20 values observed on the logs, e.g., gamma ray, porosity, Poison's ratio, Young's modulus, silts,

clays, saturations, rock quality by reservoir point of view, etc., the study was made to compare which parameters had a larger influence on the fracture height limitation. Based on the observations made, the logs compared all inputs with fracture geometry predicted by design, fracture geometry adjusted by pressure match of the job execution (with real measured values), and with well log interpretation (additional criteria over the basic logs, gamma ray, sonic traveltime, etc.). The jobs were visually arranged, with the observation and correlation of all data in images used to match the depth of the perforations, and to compare the log values with the fracture height obtained by design, and then compared with the real temperature log available after injection, Fig. 7.

The study was made over more than 50 wells, which at that moment had available all the information required. Several more wells were also studied, but some of the information was not available or was incomplete. To have the most complete examples of better discretization on the parameters for this study, only the cases with all information available were used. Table 2 shows the details of the first base line study made, which corresponds to 40% of the wells analyzed as those cases for which observations were made with complete confidence.

Note that some data was considered important for some experts, but was not mapped on the study, and is not shown in Table 2. This decision was made as those parameters were constant for all cases, and did not influence the fracture height interpretation, e.g., perforation gun type[4], base line frac fluid, and injection test fluid type, among others.

The normal sequence of every job was:

1. Do a small injection test with potassium chloride-based brine; in all cases the same fluid is used.
2. Perform a step rate test and/or step down test.
3. Calibrate the injection with cross-linked fluid as per the planned one for the main job.
4. Run a temperature log (HRT), and study the data from step 3.
5. Execute the main job proppant fracture execution (based on step 3).
6. Perform a pressure match of the job, to be adjusted as per the HRT.

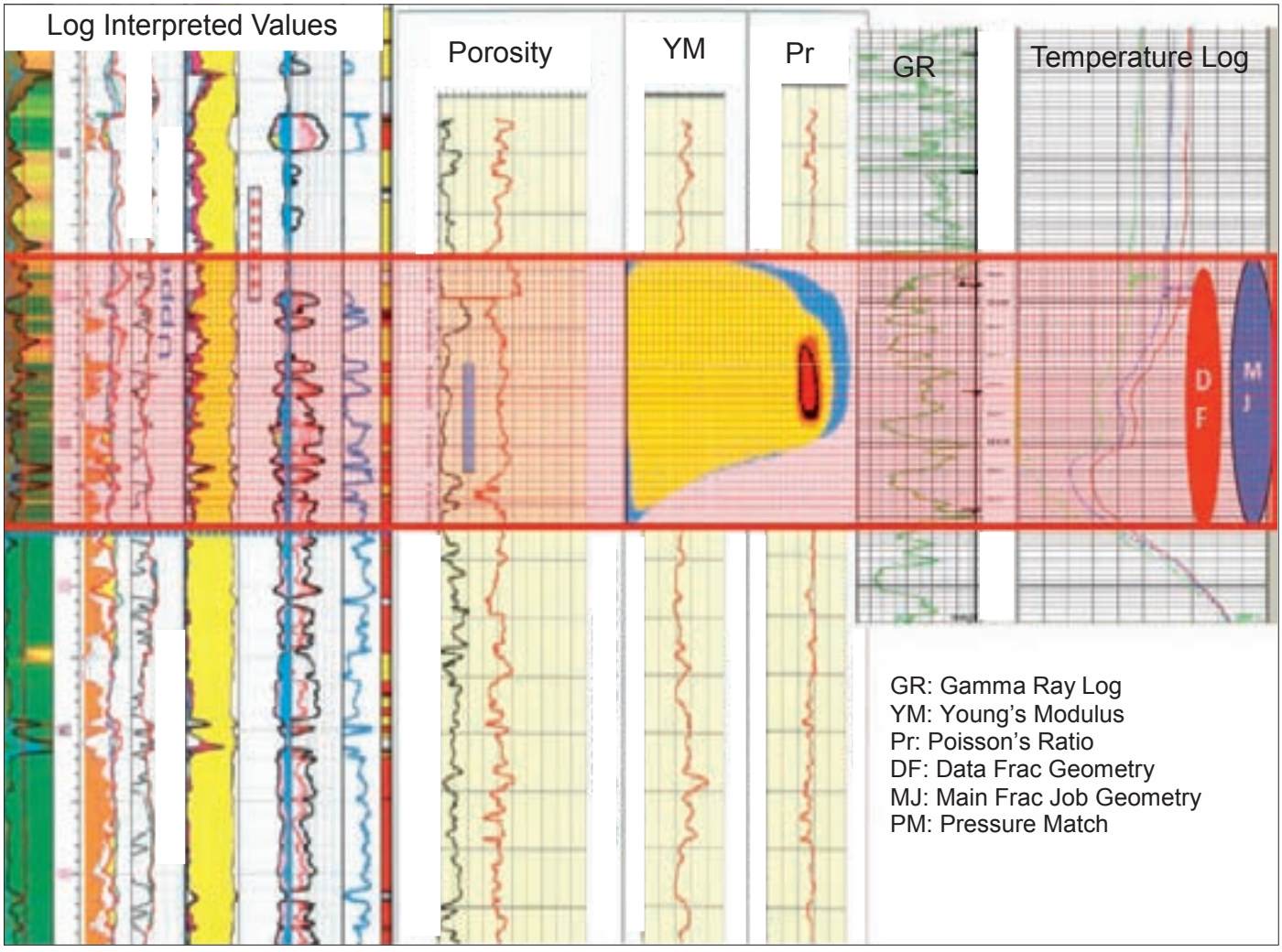

Fig. 7. Example of the exercise made on every case of the study to analyze logs vs. fracture geometry suggested by computational analysis. Fracture geometry generated by computer is the yellow oval shape over the Young's modulus (YM) and Poisson's ratio (Pr) logs. The red dash section represents the fracture height related to all other parameters related by depth.

Well Case	Field	Area	Formation	Fracture Height (ft)	Perforation (ft)	Stress	Porosity	Gamma Ray (GR)	Comments
1	A	S-E	X	140	30	Almost Constant	Drastically Changed	Certain Influence	Porosity is dominant
2	A	S-E	X	100	30	Constant	Dominant	High	Porosity is dominant
3	B	C-E	V	215	20	Dominant	Certain Influence	Dominant	Fracture geometry is dominated by stress and GR
4	B	C-E	V	102	30	Dominant	Dominant	Certain Influence	GR may have stopped the fracture at the top and bottom
5	A	N-E	X	100	30	Flat	Almost Flat at Fracture Ends	Dominant	GR is dominant
6	A	C-S	X	70	20	Low	Dominant	Dominant	Porosity drives the fracture growth along with GR
7	A	S-E	X	100	30	Dominant	More Dominant	No Influence	Stress (low) and porosity (more dominant) dominates the fracture growth
8	A	S-E	X	100	20	Certain Influence	Dominant	No Influence	Porosity dominant (most likely)
9	A	S-E	X	70	30	Dominant	No Influence	No Influence	Fracture was driven by stress contrast, help to restrict the fracture growth
10	A	C-E	X	220	30	Dominant	High Peaks	Certain Influence	Stress most likely dominates the fracture growth. Perforation dominates higher and drives the fracture
12	A	S-E	X	90	20	Dominant	Certain Influence	Certain Influence	Stress (contrast) dominates (most influence) the fracture growth
13	A	S-E	X	100	40	No Influence	Certain Influence	Certain Influence	GR and porosity have influence. Dramatic decrease in porosity.
14	A	S-E	X	70	40	Certain Influence	No Influence	Dominant	Fracture is almost flat. Porosity might have no influence.
15	A	C	X	75	20	Certain Influence	Dominant	No Influence	Porosity dominates the fracture
16	B	N-E	V	122	35	Certain Influence	Least Influence	Certain Influence	GR and stress have influence
17	A	S-E	X	75	40	Certain Influence	Dominant	Certain Influence	Porosity contrast has dominated the fracture growth. Stress has small effect.
18	A	C-E	X	80	30	Dominant	Dominant	Certain Influence	GR has certain influence and emulates stress and porosity

Well Case	Field	Area	Formation	Fracture Height (ft)	Perforation (ft)	Stress	Porosity	Gamma Ray (GR)	Comments
19	B	C-N	W	90	20	Dominant	Dominant	No Influence	Stress and porosity determine fracture height
20	B	S-E	X	110	30	Dominant	Dominant	Certain Influence	High contrast on stress, peaks, thin layers
21	B	C-E	X	83	40	Dominant	No Influence	Dominant	Temperature log may be off, case under concern
22	B	S-E	X	80	20	Certain Influence	Dominant	Certain Influence	Porosity dominates the fracture
27	B	C-E	X	275	25	Dominant	Dominant	Certain Influence	Indiscretional height growth
28	B	C	X	100	40	Dominant	Dominant	Certain Influence	Stress and porosity determine fracture height
30	B	C-E	X	200	20	Certain Influence	Dominant	Certain Influence	Porosity dominates the fracture
35	B	C	Z	120	30	Dominant	Dominant	Dominant	Stress and porosity determine fracture height
36	B	C-E	Z	180	40	Low	Dominant		Pr influence
37	B	C-E	V	150	95	Low	Low	Dominant	GR shows more influence followed by YM
38	B	C-E	V	70	62	Certain Influence	Certain Influence	Dominant	No HRT available
39	B	N-E	V	110	30	Dominant	Certain Influence	No Influence	Stress dominates the fracture
40	B	C-E	V	180	30	Dominant	Certain Influence	Dominant	Pr influence

Table 2. First base line study to set the criteria of fracture height prediction based on logs

This study allowed us to upgrade the operation by swapping the sequence as per the following steps:

1. Interpretation of the logs.
2. Comparison of correlated wells to match the criteria on possible fracture height by dominant parameters.
3. Compare with fracture simulation by fracture design computational software.
4. Execution of the job.
5. Pressure match to evaluate differences on geometry results by software analysis.

The main advantage of the upgraded steps is that no temperature log is required, DataFRAC is avoided, thereby saving no less than 24 hours while optimizing the fracture design based on previous experience.

OBSERVATIONS AND CONCLUSIONS

The study's conclusion was reviewed and utilized to set the forecasted or predicted fracture height in wells where the HRT was still required, to prove — with confidence — that the criteria found was reliable. So far, over 25 cases were observed to match the criteria of the fracture height prediction with less than a 15% error, which for the purpose of these main fracture job designs, the adjustments for time savings and cost optimization, and the impact on operations could be obtained.

The study set this criteria as reliable for application in field operations to confidently avoid the usage of a temperature log. The study continues to be fine-tuned as areas outside of the actual studied wells are still under development. It was found to have similar trends on criteria for those areas. Table 2 prevailed to be valid in terms of holding the most important criteria to confidently predict the fracture height based on log interpretation.

The trends for this criteria narrows more when the type of reservoir and average job profile is similar to the ones pumped

in the studied cases. Two job types, in terms of volume and rate, were used. When discretization is made at the same job approach, the fracture height can be predicted with minimal error.

OUTLOOK

1. The project proved to be valid based on previous data and a new test was made with the HRT to validate the prediction. More wells are being added to the study, and the addition of new cases is important when the well is drilled in areas where correlations are expected to be similar to studied scenarios. This will help to fine-tune the criteria to predict the fracture height with more confidence.

2. The study could be extended to other areas of application, i.e., prediction of fracture volume, fracture total geometry (length in particular, width as well), perforation enhancements[5] by fracture observations, the fluid success ratio on fracture execution, and conditions to evaluate potential screen outs, etc.

ACKNOWLEDGMENTS

The authors would like to thank the management of Saudi Aramco for their support and permission to publish this article. The authors would also like to thank Nahr Abulhamayel and Yousef Noaman, for this project execution and the continuation of it.

The article was presented at the SPE Kingdom of Saudi Arabia Annual Technical Symposium and Exhibition, Dammam, Saudi Arabia, April 23-26, 2018.

REFERENCES

1. Burra, A., Esterle, J.S. and Golding, S.D.: "Use of Temperature Logs in Coal Seam Gas Reservoirs: Application to the Sydney Basin," *International Journal of Coal Geology*, Vol. 143, April 2015, pp. 68-77.
2. Buenrostro, A., Abdulkareem, H.S., Noaman, Y.M., Al-Driweesh, S.M., et al.: "Controlled Breakdown Technique Enables Proppant Fracture Placement by Enhancing Fracture Initiation; Fracture Pressure is Reduced when Applied," SPE paper 187981, presented at the SPE Kingdom of Saudi Arabia Annual Technical Symposium and Exhibition, Dammam, Saudi Arabia, April 24-27, 2017.
3. Hamid, O., Buenrostro, A., Suzart, W., Zoghbi, B., et al.: "New Methodology to Calibrate Rock Mechanics Parameters via Tuned Geomechanics Technique after Falloff Matched Curve," paper presented at the 10th Edition of the Scientific and Technical Days, the 2nd Edition of the Scientific Exhibition, Oran, Algeria, October 5-8, 2015.
4. Behrmann, L.A. and Elbel, J.L.: "Effect of Perforations on Fracture Initiation," *Journal of Petroleum Technology*, Vol. 43, Issue 5, May 1991, pp. 608-615.
5. Jackson, R.A. and Craig, D.P.: "Depth-of-Investigation and Volume-of-Investigation Calculated from Fracture-Injection/Falloff Test DFIT Data," SPE paper 185029, presented at the SPE Unconventional Resources Conference, Calgary, Alberta, Canada, February 15-16, 2017.

BIOGRAPHIES

Adrian Buenrostro is a Senior Petroleum Engineer in the Gas Production Engineering Division of the Southern Area Production Engineering Department of Saudi Aramco. He has 16 years of experience in the oil and gas industry, which includes production and completion engineering, well management, training and mentoring, sales and marketing, particularly developed in the stimulation area in Latin-America, Europe, and Saudi Arabia.

Adrian has been a Society of Petroleum Engineers (SPE) certified Engineer since 2015. He has written multiple technical articles for international publications and coauthored several more. Adrian developed the concept of channel fracturing with resin coated natural sand, which is patented.

He received both his B.S. and M.S. degrees in Mechanical Engineering from the National Autonomous University of Mexico, Mexico City, Mexico. Adrian received the Mexican national Engineering Medal for his engineering work in 2001.

Mohammed Al-Abdrabalnabi is a Petroleum Engineering Scientist working with the Production Technology Division of Saudi Aramco's Exploration and Petroleum Engineering Center – Advanced Research Center (EXPEC ARC). The team targets well productivity enhancements such as laser oriented fracturing, optimized fracture conductivity, and water shut-off by chemical means.

In 2015, he received his B.S. degree with honors in Chemical Engineering from King Fahd University of Petroleum and Minerals (KFUPM), Dhahran, Saudi Arabia.

Amro E. Mukhles is a Petroleum Engineer supervisor in Saudi Aramco's Southern Ghawar Production Engineering Department. He has 12 years of experience in the oil and gas industry in areas like production optimization, well completion, stimulation, well intervention operations as well as scale and corrosion mitigation.

Amro received his B.S. degree in Petroleum Engineering from West Virginia University, Morgantown, WV, and his M.S. degree in Petroleum Engineering from the University of Texas at Austin, Austin, TX.

Saad M. Al-Driweesh is a General Supervisor in the Southern Area Production Engineering Department, where he is involved in gas production engineering, well completion, and fracturing and stimulation activities.

Saad is an active member of the Society of Petroleum Engineers (SPE), where he has chaired several technical sessions at local, regional and international conferences. He is also the 2013 recipient of the SPE Production and Operations Award for the Middle East, North Africa and India region. In addition, Saad chaired the first Unconventional Gas Technical Event and Exhibition in Saudi Arabia.

He has published several technical articles addressing innovations in science and technology. Saad's main interest is in the field of production engineering, including production optimization, fracturing and stimulation, and new well completion applications. He has 26 years of experience in areas related to gas and oil production engineering.

In 1988, he received his B.S. degree in Petroleum Engineering from King Fahd University of Petroleum and Minerals (KFUPM), Dhahran, Saudi Arabia.

Advanced Corrosion and Scale Monitoring under Downhole Conditions with Applied Corrosion Inhibitor Batch Treatment in Sour Gas Wells

Dr. Tao Chen, Dr. Feng Liang, Dr. Fakuen F. Chang, and Amro E. Mukhles

ABSTRACT

An advanced downhole corrosion and scale monitoring (DCSM) tool has been designed and developed to measure corrosion and scale in sour gas wells. It has been deployed at the desired depth in the sour gas well, along with the corrosion inhibitor batch treatment. The tool was retrieved after 5 months of exposure to the reservoir condition for post-laboratory analysis.

Advanced analytical techniques were carried out on retrieved coupons to understand the corrosion and scaling mechanism, and quantify the weight changes. X-ray diffraction (XRD) was used to analyze the scale composition of the coupon surface. A scanning electron microscope (SEM) and energy dispersive X-ray spectrometer (EDS) were used to investigate the morphology and mineralogical changes on the surface. A surface profilometer was used to analyze the thickness of scale surface deposition and localized corrosion.

The results showed that a thin layer — ~25 micron in thickness — of iron sulfide scale had formed on the surface of the metal coupon. It served as a protective layer, thereby preventing and reducing further corrosion and scale buildup. Localized pitting corrosion was found, which indicates that corrosion happened first followed by scale layer deposition on the surface of the metal coupon.

INTRODUCTION

Iron sulfide deposition is an exotic scale deposited during oil and gas production, especially for deep sour gas wells producing from high-pressure, high temperature (HPHT) reservoirs. It is a corrosion induced scale problem, which can cause flow assurance problems, such as restriction of downhole surveillance and intervention[1-4].

Iron sulfide deposition on the surface of downhole tubulars is not evenly distributed. It gets more severe as the well depth gets deeper. Scale deposition is often negligible, or only a very thin scale layer appears in the upper portion of the tubulars, while thick deposits have been observed at the bottom of the tubulars. Loss of tubular thickness due to general corrosion also increases with well depth[3].

Over the past few decades, great efforts have been made to understand the mechanisms and mitigation strategies of iron sulfide deposition in downhole tubulars. Our previous study concluded that tubing corrosion is one of the major sources of iron for iron sulfide surface deposition in downhole tubulars during production[3]. The iron released from the tubing due to acid corrosion during acidizing treatment is another major source of iron for iron sulfide deposition. Iron sulfide and iron carbonate are predicted to precipitate during acidizing treatment. Iron sulfide forms when the spent acid is saturated with sour gases, or mixes with formation water saturated with sour gases[5, 6]. Both chemical and mechanical methods have been used to remove downhole iron sulfide scale[7]. Hydrochloric acid based scale dissolvers were applied to chemically remove the deposits. Subsequently, heavy corrosion to the production string and casing, and the generation of hydrogen sulfide (H_2S) during descaling jobs, are major concerns and barriers to the application of this type of scale dissolver in these sour gas wells. Mechanical de-scaling can remove iron sulfide deposited in the tubing, but it is costly and time-consuming. Moreover, mechanical de-scaling cannot approach and remove the scale deposited in the near wellbore region[8].

Corrosion and scale monitoring has played a key role to develop effective prevention and mitigation strategies in a cost-effective and timely manner. One of the major challenges of corrosion and scaling management in a sour gas well is to effectively and closely monitor corrosion and scaling downhole under real flow regime conditions. It is very difficult to simulate the actual environment and flow conditions in a laboratory to study downhole corrosion and scale formation. Multiple ways of corrosion monitoring methods have been developed[9, 10], such as system component inspection, coupon testing, electrical resistance, ultrasonic measurement, etc.

Coupon testing is a simple and inexpensive way for corrosion monitoring; however, it may not be the best representative experiment due to multiple factors such as the difference of temperature, pressure, flow regime, flow media, and flow conditions. Electrical monitoring methods using electrical resistance and linear polarization resistance measurement allow for continuous and instantaneous corrosion rate monitoring. Consequently, the results do not always correlate directly to the real corrosion rate, and may not indicate pitting corrosion very precisely. Additionally, challenges still exist to deploy electrical monitoring tools to the downhole and generate a reliable

corrosion rate under a HPHT environment. Compared with the corrosion monitoring techniques, there are limited monitoring methods for detecting scaling. To do this, Emmons et al. (1999)[11] introduced an on-site real-time monitoring tool for scale tendency detection of produced water by adding additional scaling anions or cations. This method shows good potential as an online monitoring tool for conventional scales, such as calcium carbonate and barium sulfate, but not for iron sulfide, which is an exotic scale with different formation mechanisms. There is still a need to develop an effective tool to monitor iron sulfide deposition in sour gas wells under downhole conditions.

This article introduces a new developed downhole corrosion and scale monitoring (DCSM) tool to allow direct corrosion and scaling monitoring of the performance of a corrosion inhibitor batch treatment under real downhole conditions in a sour gas well.

EXPERIMENTAL PROCEDURE

A new developed DCSM tool has been designed and developed for measuring corrosion and scale formation under downhole conditions in sour gas wells.

The DCSM tool includes two body segments, Fig. 1. The upper body segment is a gauge hanger, an elongated member with an axial protrusion with a reduced outer diameter. It allows the downhole devices to be securely anchored in the wellbore while using conventional slick line methods for setting and retrieving. The lower body segment is composed of a coupon and coupon holder, which are sized for connecting with the upper body segment. Metal coupons are placed on the outside of the second body segment to simulate the corrosion and scaling conditions closely by exposing to similar flow regimes in sour gas wells. The sealing and isolation of parts are placed between the metal specimen and tool body as well as between the tool body parts. Several exchangeable metal coupons with identical metallurgy as the downhole completion tubing can be deployed on the tool to measure the rate of corrosion.

Fig. 1. The DCSM tool is made up of two parts.

This monitoring system represents significant improvements over the current industrial technology by directly measuring corrosion and scale deposition in real downhole conditions using coupons made of identical metallurgy as the production tubing. The concept of the development has been approved from the lab design, and manufactured to field application. The field application had been carried out in a typical sour gas well containing ~5% H_2S and 3% carbon dioxide gas stream at temperatures of ~125 °C and a pressure of ~5,000 psi. The well has experienced severe iron sulfide deposition in downhole tubulars. A slick line with a retrievable high expansion gauge hanger was used to deploy and anchor the DCSM downhole at the desired depth of ~12,000 ft. After the DCSM tool was set downhole, a corrosion inhibitor batch — 100 gallons — was injected into the well, which was diluted by formation water to reach 10% volume concentration. The test coupon was made with T-95 carbon steel, the same material as the downhole tubing. The coupon was retrieved after 5 months of field deployment for post-laboratory analysis.

To understand the corrosion and scaling mechanisms, advanced post-analyses were performed, including weight change measurement, scanning electron microscope (SEM), energy dispersive X-ray spectrometer (EDS), X-ray diffraction (XRD), and surface profile measurement.

A ZEISS SIGMA HD-VP SEM was used for analyzing the morphologies of inorganic scale deposition. An electron beam — about 15 kV — is scanned across a sample's surface. When the electrons strike the sample, a variety of signals, such as backscatter electrons, secondary electrons or X-rays from the interaction between the material and the electron beam, are generated. It is the detection of specific signals that produces an image or a sample's elemental composition. A Bruker EDS was used to collect X-rays generated by the interaction. All elements, above a certain detection threshold, on the surface of the DCSM test coupons, down to the atomic number of carbon, can be detected. The spectra are de-convolved in real-time and chemical compositions were acquired. Both qualitative and quantitative analyses were performed.

A Bruker D8 Advance X-ray diffractometer was used to study the mineral composition of scale deposited on the surface of the DCSM test coupon. The Cu Kα X-rays (1.5418 Angstrom) were diffracted by the crystalline phases in the specimen according to Bragg's law ($\lambda = 2d \sin \theta$, where λ is the wavelength of the X-rays, d is the spacing between atomic planes in the crystalline phase, and 2θ is the angle between the incident and diffracted X-rays), and the intensity of the diffracted X-rays was measured as a function of the diffraction angle and the specimen's orientation. The resulting diffraction pattern was loaded into the Bruker's Diffrac-Eva (analytical) software and the specimen's crystalline phases were identified against the International Center for Diffraction Data PDF-4 database.

The measurement of the peak-to-valley height for the surface profile of test coupons is an important parameter to understand the morphologies of scale surface. The surface of the coupon was scanned using a Nanovea PS50 profilometer, which was designed with leading edge chromatic confocal optical

technology (axial chromatism) both ISO and ASTM compliant. The technique measures a physical wavelength directly related to a specific height without using complex algorithms. After the scale, which was deposited on the surface of the test coupon, was removed by using a corrosion inhibited acidic solution, the same area of the surface was examined to study the under deposit corrosion condition.

RESULTS

The weight of the T-95 coupon before and after field application was recorded, Table 1. A slight weight increase of 0.049 g was calculated after the field application. The overall weight change may be due to two physical/chemical changes, the weight loss caused by corrosion and the weight gain caused by the scale formation on the coupon's surface.

Figure 2a shows the photograph of the T-95 carbon steel coupon before field application, and Fig. 2b shows the same T-95 coupon after being retrieved from 5 months of exposure in the field. Before field application, the coupon was shining without any deposition or corrosion. After a 5-month field application, a thin layer of black deposition was observed on the surface of the test T-95 coupon. Based on visual observation, there was a certain amount of corrosion byproduct or scale deposited on the surface of the coupon during the 5-month field application.

Figure 3a is the optical image of the surface of the T-95 carbon steel coupon before field application, and Fig. 3b is the optical image of the T-95 coupon after being retrieved from 5 months of exposure in the field. No obvious features besides the machining lines were observed on the surface before field application, while patched areas with a size of around a few hundred microns were observed from the surface coupon after it was retrieved from the field.

	Weight before Application (g)	Weight after Application (g)	Weight Change (g)
T-95 Coupon	117.821	117.880	0.049

Table 1. Weight change of a T-95 coupon before and after field application

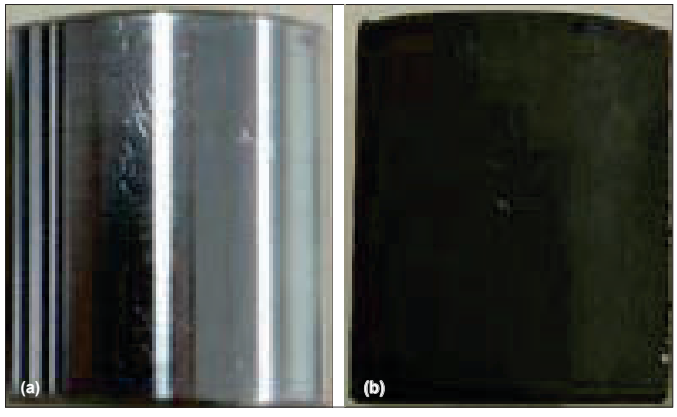

Fig. 2. Before and after photographs of the T-95 coupon; (a) before field application, and (b) after being retrieved from the field after 5 months.

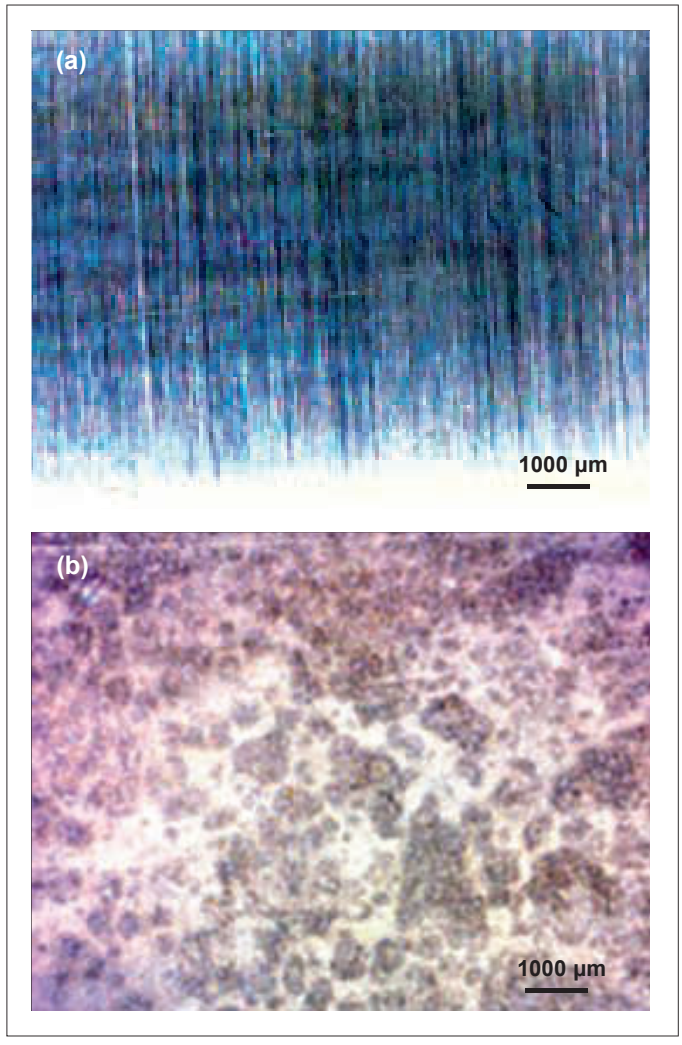

Fig. 3. Before and after optical images of the T-95 coupon; (a) before field application, and (b) after being retrieved from the field after 5 months.

High resolution SEM images were taken on the cross-section of the T-95 coupon sample after the field application to identify the thickness of the black deposit. Figure 4a is a backscatter image of the area. The scale layer was found to be about 25 µm. EDS was also performed for the elemental analysis of the thin layered black deposit, Figs. 4b to 4d, which was mainly composed of iron and sulfur, with some oxides. The weight percent ratio of the iron to sulfur is around 1.8 to 1.

XRD was carried out to further analyze the mineralogy of the thin layer of black deposit on the surface of the coupon after the 5-month field application. The surface deposit was composed of different types of iron sulfide crystals, including pyrrhotite, pyrite and marcasite, at a composition of 66% pyrrhotite, 24% pyrite, and 9% marcasite, respectively, Fig. 5.

The measurement of the peak-to-valley height for the surface profile of the test coupons is an important parameter to understand the under deposit corrosion. The surface profile of the test coupon after 5 months of exposure to the field application was measured, Figs. 6a and 6b. The surface scan showed

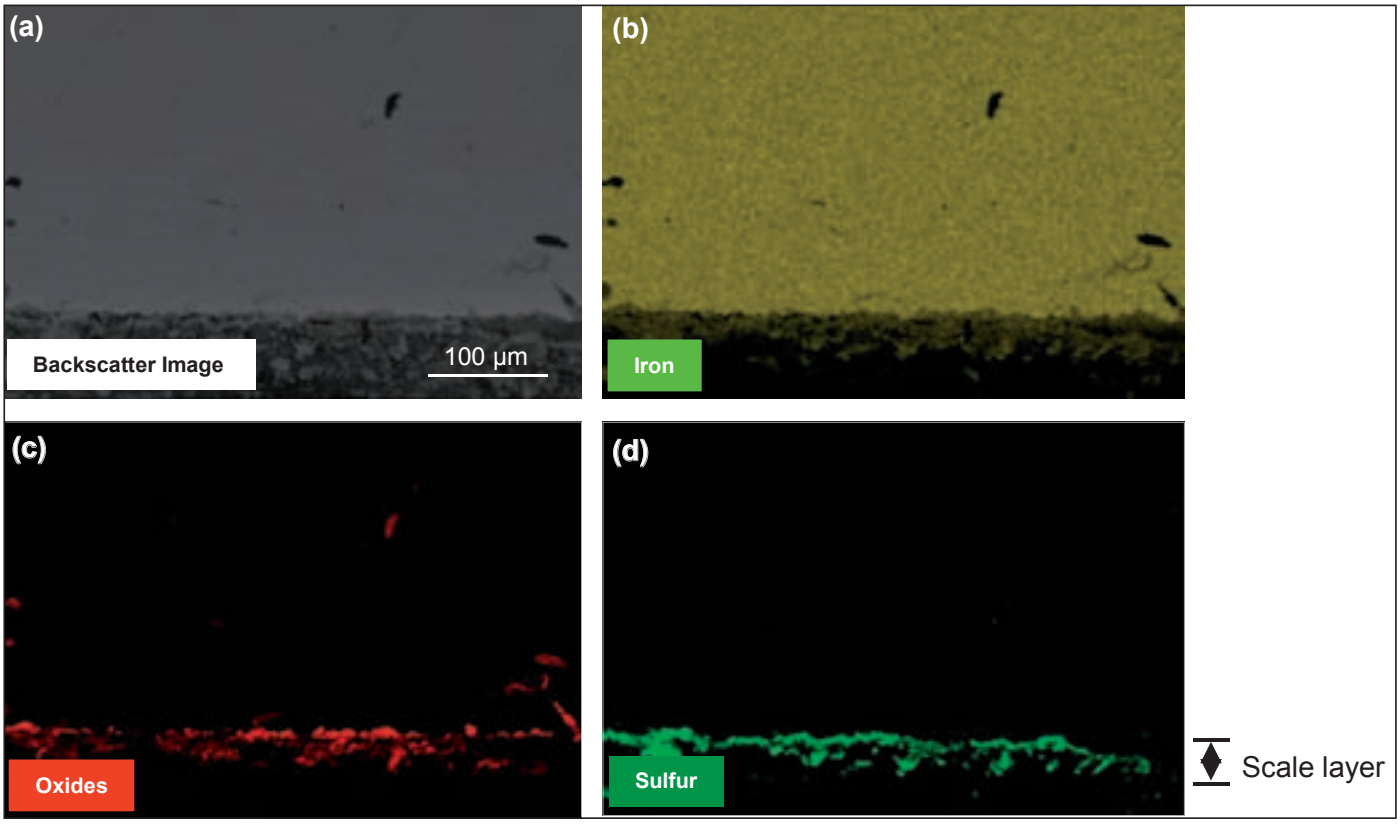

Fig. 4. SEM image and EDS analysis of cross-section of the T-95 coupon after the 5-month field application; (a) backscatter image, (b) EDS analysis of iron, (c) EDS analysis of oxides, and (d) EDS analysis of sulfur.

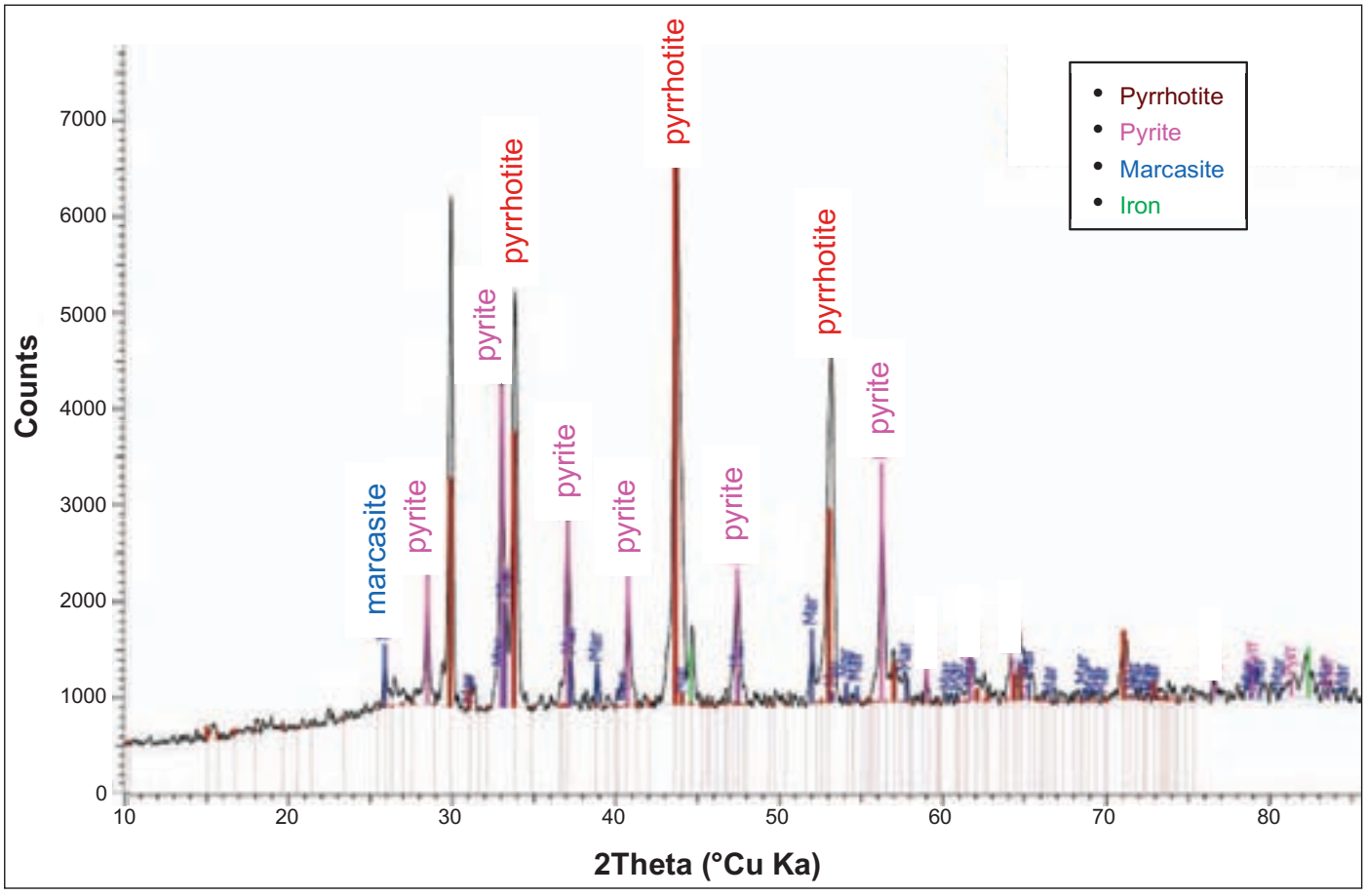

Fig. 5. XRD composition analysis of the T-95 coupon surface deposition after 5 months of exposure at reservoir condition.

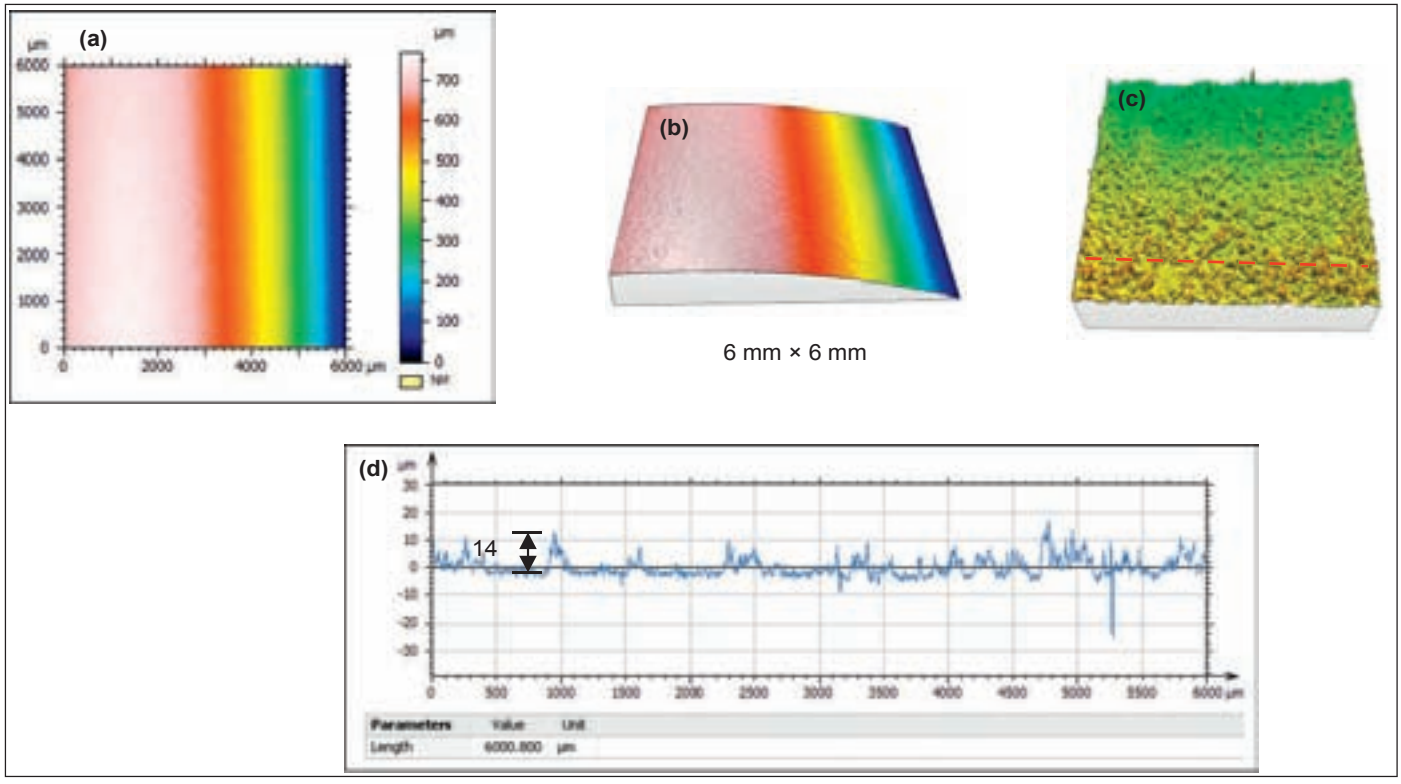

Fig. 6. Surface profile of the T-95 coupon after field trial, using a general scale surface morphology analysis; (a) surface scan 6 mm × 6 mm (scan step, 2.6 µm); (b) 3D surface profile, (c) fattened surface, and (d) height profile along the red line in Fig. 6c.

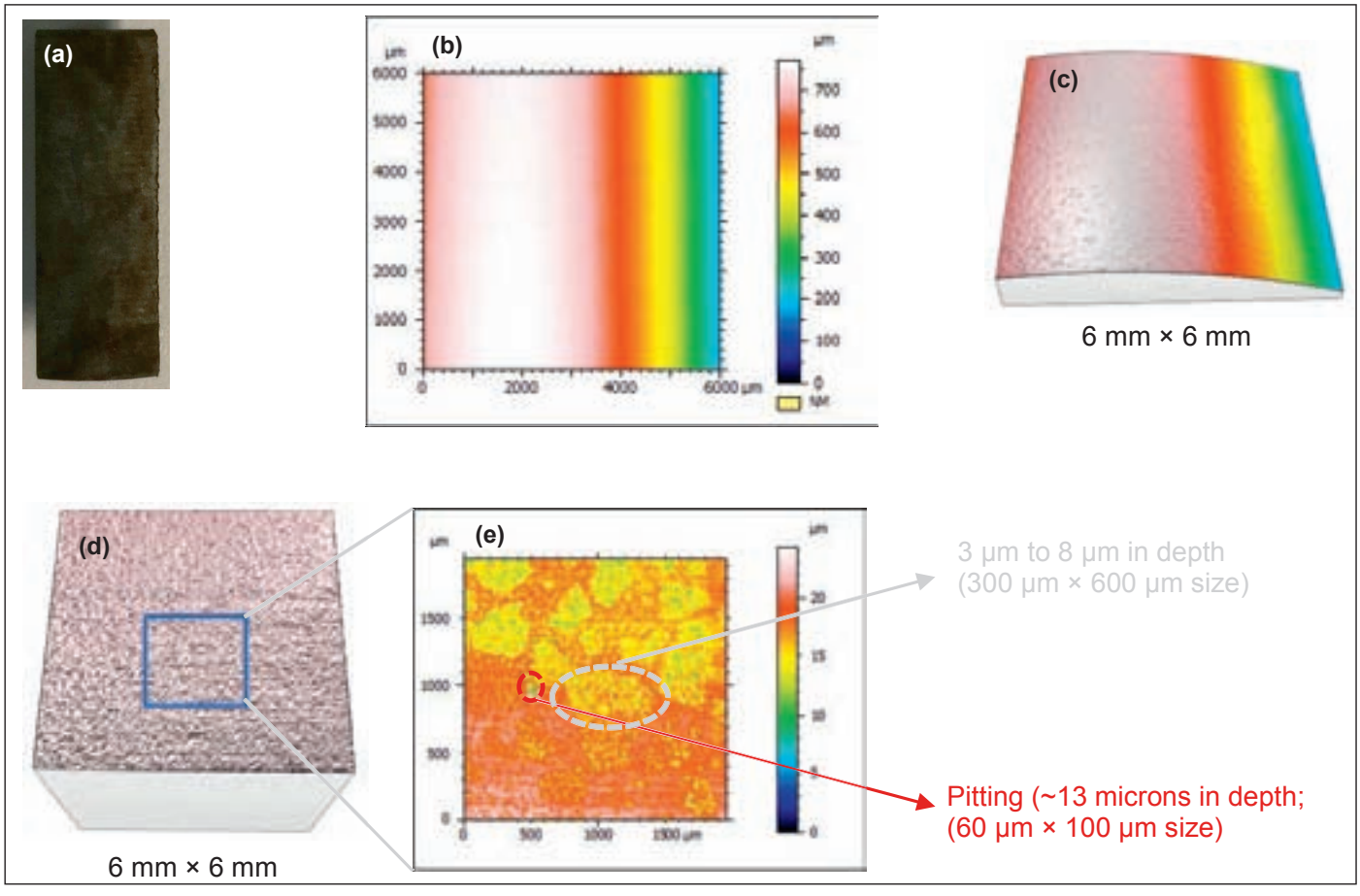

Fig. 7. Surface profile of the retrieved T-95 coupon after the scale layer was removed by general corrosion surface morphology analysis; (a) photograph of the retrieved coupon after corrosion inhibited fluid wash, (b) surface scan 6 mm × 6 mm (scan step, 2.6 µm), (c) 3D surface profile; (d) fattened surface (6 mm × 6 mm), and (e) zoomed in scan image of the blue-squared area in Fig. 7d.

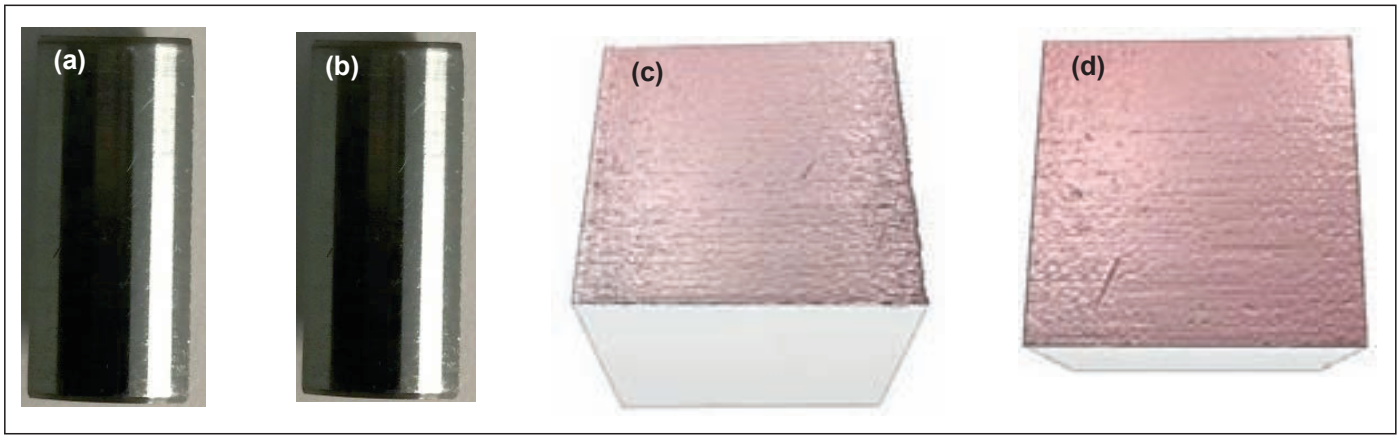

Fig. 8. Surface profile of the pristine T-95 coupon; (a) photograph of coupon before corrosion inhibited fluid treatment, (b) photograph of the coupon after corrosion inhibited fluid treatment, (c) flattened surface profile of the coupon before corrosion inhibited fluid treatment, and (d) flattened surface profile of the coupon after corrosion inhibited fluid treatment.

a thin layer of deposit formed on the coupon's surface, which agreed with the results analyzed by SEM, as previously seen in Fig. 4. The uneven scale surface was observed in Fig. 6c. Figure 6d shows the height profile along the red line in Fig. 6c. Surface height variations of around 5 µm to 15 µm were observed.

To understand the under deposit corrosion, the surface deposition of the test coupon was removed by corrosion inhibited acid, which was used to chemically remove scale deposition without causing additional corrosion to the metal surface. The under deposit corrosion of the same scanning area in Fig. 6 was investigated by surface scan, Figs. 7a to 7e. General corrosion was observed with a 3 µm to 8 µm deep spot. In addition, a localized corrosion spot with a depth of ~13 µm was observed.

To examine if the corrosion inhibited acid fluid will cause additional corrosion to the metal surface, a pristine T-95 metal coupon was treated with the same corrosion inhibited acid as the field retrieved coupon. The surface profile of the pristine T-95 metal coupon before and after inhibited acid treatment were conducted, Figs. 8a to 8d, respectively. Not much surface corrosion was observed for the T-95 metal coupon with the treatment fluid.

According to Chen's study[3], the iron released from the tubing due to tubing corrosion is one of the major iron sources for iron sulfide deposition on downhole tubulars. The iron released from the tubing and the test metal coupon reacted with H_2S and formed a thin layered iron sulfide surface deposition, which can cause a slight weight increase, as previously seen in Table 1. The scale deposition worked as a protective layer to reduce any further interactions between the metal tubulars and the produced gas and/or fluid media. In this way, further corrosion of the test coupon could be reduced.

This observation agrees with the findings from other studies, where iron sulfide films formed on carbon steel during sour oil and gas production, and they can be served as long-lasting protective layers[7, 12]. The thickness of the surface deposition was ~25 µm after the 5-month field application, as previously seen in Fig. 4. The rate of iron sulfide deposition was far less than the field observation, since up to ⅜" thick deposits have been observed at the bottom of the tubulars[3]. Other sources of iron sulfide scale deposition should be further investigated in sour gas wells.

The general and localized pitting corrosion found underneath the surface deposition indicates that corrosion happened first, followed by scale layer deposition on the metal coupon surface. Localized pitting corrosion is one of the major concerns for sour gas wells, which can cause significant production loss and costly workover to replace the damaged tubing downhole.

The newly developed DCSM tool has an advanced design allowing direct corrosion and scaling monitoring under downhole conditions in sour gas wells. In combination with the post-laboratory analysis on the retrieved coupons, the tool can provide a corrosion and scale mechanism for specific metallurgy in sour gas wells, leading to proper corrosion and scale management programs, which could be designed to minimize the effects of corrosive gases. This developed tool can be used to monitor the effectiveness of the corrosion treatment and can be deployed in sweet gas wells, oil wells, and water supply wells.

CONCLUSIONS

1. The newly developed DCSM tool is an advanced design that allows direct corrosion and scaling monitoring in the downhole condition. The data generated by this tool provides meaningful technical information about the aspects of the corrosion and scale tendency under real downhole conditions in sour gas wells.
2. A thin layer of iron sulfide was found deposited on the surface of a T-95 carbon steel coupon after 5 months of field exposure. The scale deposition worked as a protective layer to reduce further interactions between the metal coupon and the produced gas and/or fluid media. In this way, further corrosion of the test coupon could be reduced. The thickness of the surface deposition is ~25 µm. The rate of iron sulfide deposition is far less than the field observation. Other sources of iron sulfide scale deposition

should be further investigated in sour gas wells.

3. General corrosion — 3 µm to 8 µm — and localized pitting corrosion — ~13 µm — were found underneath the surface deposition after 5 months of field exposure. It indicates that corrosion happened first, followed by scale layer deposition on the metal coupon surface. Localized pitting corrosion is one of the major concerns for sour gas wells, which can cause significant production loss and costly workover to replace the damaged tubing downhole.
4. In combination with the post-laboratory analysis on the retrieved coupons, the DCSM tool can provide a corrosion and scale mechanism for specific metallurgy in sour gas wells, leading to proper corrosion and scale management programs, which could be designed to minimize the effects of corrosive gases. It can be used to monitor the effectiveness of the corrosion treatment and can be deployed in sweet gas wells, oil wells, and water supply wells.

ACKNOWLEDGMENTS

The authors would like to thank the management of Saudi Aramco for their support and permission to publish this article. The authors would also like to thank Esmael Albelharith for the field application support, Jilin Zhang for XRD analysis, and Jordan Kone for the SEM analysis.

REFERENCES

1. Leal Jauregui, J.A., Solares, J.R., Nasr-El-Din, H.A., Franco, C.A., et al.: "A Systematic Approach to Remove Iron Sulfide Scale: A Case History," SPE paper 105607, presented at the SPE Middle East Oil and Gas Show and Conference, Manama, Kingdom of Bahrain, March 11-14, 2007.
2. Wang, Q., Ajwad, H., Shafai, T. and Lynn, J.D.: "Iron Sulfide Scale Dissolvers: How Effective Are They?" SPE paper 168063, presented at the SPE Saudi Arabia Section Technical Symposium and Exhibition, al-Khobar, Saudi Arabia, May 19-22, 2013.
3. Chen, T., Wang, Q. and Chang, F.F.: "Understanding the Mechanisms of Iron Sulfide Formation in Sour Gas Wells," paper 8211, presented at the 16th Middle East Corrosion Conference and Exhibition, Manama, Kingdom of Bahrain, February 8-11, 2016.
4. Wang, Q., Leal Jauregui, J.A., Syafii, I., Mukhles, A.E., et al.: "Iron Sulfide and Removal in Scale Formation Sour Gas Wells," SPE paper 179869, presented at the SPE International Oil Field Scale Conference and Exhibition, Aberdeen, Scotland, U.K., May 11-12, 2016.
5. Lu, P., Chen, T., Wang, Q. and Chang, F.F.: "New Understanding on Iron Sulfide Deposition during Acid Stimulation in Sour Gas Wells Using an Advanced Modeling Approach," paper 11060, presented at the NACE International/CORROSION 2018 Conference and Exposition, Phoenix, Arizona, April 15-19, 2018.
6. Chen, T., Wang, Q. and Chang, F.F.: "New Insight into the Mechanisms of Iron Sulfide Deposition in Carbonate Reservoir during Acid Stimulation," paper 11141, presented at the NACE International/CORROSION 2018 Conference and Exposition, Phoenix, Arizona, April 15-19, 2018.
7. Hamby Jr., T.W.: "Development of High-Pressure Sour Gas Technology," *Journal of Petroleum Technology*, Vol. 33, Issue 5, May 1981, pp. 792-798.
8. Chen, T., Wang, Q., Chang, F.F. and Albelharith, E.: "Multifunctional and Non-Acidic Iron Sulfide Scale Dissolver for Downhole Applications," SPE paper 188924, presented at the Abu Dhabi International Petroleum Exhibition and Conference, Abu Dhabi, UAE, November 13-16, 2017.
9. Pickthall, T., Rivera, M., McConnell, M. and Vezis, R.: "Corrosion Monitoring Equipment — A Review of Application and Techniques," paper 11280, presented at the NACE International/CORROSION 2011 Conference and Exposition, Houston, Texas, March 13-17, 2011.
10. Fincher, D.R. and Nestle, A.C.: "A Review of Corrosion Monitoring Techniques," SPE paper 4220, presented at the SPE Symposium on Handling of Oil Field Water, Los Angeles, California, December 4-5, 1972.
11. Emmons, D.H., Graham, G.C., Holt, S.P., Jordan, M.M., et al.: "On-Site, Near Real-Time Monitoring of Scale Deposition," SPE paper 56776, presented at the SPE Annual Technical Conference and Exhibition, Houston, Texas, October 3-6, 1999.
12. Bich, N.N. and Goerz, K.: "Caroline Pipeline Failure: Findings on Corrosion Mechanisms in Wet Sour Gas Systems Containing Significant CO_2," paper 26, presented at the NACE International/CORROSION 1996 Conference and Exposition, Denver, Colorado, March 24-29, 1996.

BIOGRAPHIES

Dr. Tao Chen is a Petroleum Engineering Specialist working with the Production Technology Team of Saudi Aramco's Exploration and Petroleum Engineering Center – Advanced Research Center (EXPEC ARC). His interests are production chemistry and flow assurance in the oil and gas industry, specializing in oil field scale management.

Prior to joining Saudi Aramco in 2014, Tao spent more than 15 years on oil field scale management and worked at Clariant, Champion Technologies, Nalco Champion, and LR Senergy in Aberdeen, U.K.

He has published nearly 70 technical publications about scale management in oil fields.

Tao received both his B.S. and M.S. degrees in Chemical Engineering from Dalian University of Technology, China, and his Ph.D. degree in Chemical Engineering from Heriot-Watt University, Edinburgh, U.K. Tao also received an MBA from Warwick University, Coventry, U.K.

Dr. Feng Liang is currently a Petroleum Engineer at the Aramco Services Company, Aramco Research Center, Houston, TX. She has been with the company for almost five years.

Prior to joining the Aramco Research Center, Feng was a Principal Scientist at Halliburton for nearly eight years. Her research interests are the new materials and product development in fracturing fluid, advanced fluid additives, waterless fracturing technologies, bio-degradable diversion materials, sand control products, cement additives, and nanomaterial reinforced elastomers.

Feng holds more than 40 issued patents and 30 additional published patent applications. She has also authored or coauthored more than 60 technical papers, with a few published in very high impact factor journals. Feng has coauthored two book chapters as well. Her publications have been cited over 2,800 times.

Feng has been a member of the Society of Petroleum Engineers (SPE) since 2007. In 2017, she received the SPE Regional Production and Operations Award for the Gulf Coast North American region. Also in 2017, Feng received the 2017 Effective Publication Award from EXPEC ARC.

She received her Ph.D. degree in Organic Chemistry from Rice University, Houston, TX.

Dr. Fakuen "Frank" F. Chang is the focus area champion for Productivity Enhancement in the Production Technology Team of Saudi Aramco's Exploration and Petroleum Engineering Center – Advanced Research Center (EXPEC ARC).

Prior to joining Saudi Aramco in September 2012, he worked at Schlumberger for 16 years. Before that, Frank was at Stimlab for 4 years. He has developed many products and technologies dealing with sand control, fracturing, acidizing and perforating.

Frank is an inventor and recipient of 23 granted U.S. patents, and he is the author of more than 40 Society of Petroleum Engineers (SPE) technical papers.

Frank received his B.S. degree in Mineral and Petroleum Engineering from the National Cheng Kung University, Tainan City, Taiwan; his M.S. degree in Petroleum Engineering from the University of Louisiana at Lafayette, Lafayette, LA; and his Ph.D. degree in Petroleum Engineering from the University of Oklahoma, Norman, OK.

Amro E. Mukhles is a Petroleum Engineer supervisor in Saudi Aramco's Southern Ghawar Production Engineering Department. He has 12 years of experience in the oil and gas industry in areas like production optimization, well completion, stimulation, well intervention operations as well as scale and corrosion mitigation.

Amro received his B.S. degree in Petroleum Engineering from West Virginia University, Morgantown, WV, and his M.S. degree in Petroleum Engineering from the University of Texas at Austin, Austin, TX.

Material Overview for Electric Submersible Pumps: Part 1 — Metallic and Ceramic Materials

Dr. Jinjiang Xiao, Rafael A. Lastra, Brian A. Roth, and Dr. Woon Lee

ABSTRACT

An electric submersible pump (ESP) is a key artificial lift technology to the petroleum industry. Worldwide installations of ESPs are in the range of 130,000 units, contributing to approximately 60% of the total worldwide oil production. An ESP is made up of hundreds of components integrated together to perform the lifting function. Materials in these components belong to several categories, including metals, ceramics, polymers, and others. A good understanding of these materials and vigilant selection for a specific application are critical to the reliability and run life of an ESP system. This article presents an overview of two classes of materials used in ESP systems: metallic and ceramic materials. A subsequent article is planned to cover all other categories of materials. The intent is to provide a reference for ESP field application engineers who are responsible for ESP design, component selection, the equipment longevity, and production optimization.

The information compiled in this article is a result of extensive literature review. It covers materials used in the motor, protector, pump, and cable — sensor, packer, Y-tool, diverter valve, surface components of variable speed drives, and transformer not included. For each class of materials, it identifies relevant material properties and discusses suitable application conditions.

INTRODUCTION

An electric submersible pump (ESP) is a complex electromechanical system that requires each and every component to perform its intended function to achieve the system's artificial lift purpose. The proper function and reliability of each component depends not only on the design, but more importantly on the specific material chosen. These materials can be grouped into several major categories, as indicated in Table 1. This article contains a review of two material classes: metallic and ceramic materials.

Information of ESP material specifications is scattered in published papers, industrial standards, ESP manuals, textbooks and the internet. A compressive summary of such an important subject cannot be found in the ESP industry. This article intends to fill the gap. It provides a handy reference and a guidance for ESP application engineers. Accurate information on ESP materials is essential for application engineers to properly specify materials and understand ESP failure mechanisms to improve system reliability. Material science is a vast area requiring special expertise and experience. This article is not intended to be a substitute for expert advice, but to provide a starting point for higher level discussions.

Every effort is made to avoid the use of material tradenames in the article; however, tradenames do frequently appear in ESP publications, and it becomes necessary for application engineers to get familiar with them in the literature. Therefore, some tradenames are included in the article where it is unavoidable. There is no intention to promote any specific types of materials in this article.

METALLIC MATERIALS

Metallic materials or metals are used in an ESP system for their mechanical strength to carry the load (tensile, compressional, and torsional), abrasion/corrosion resistance, and electrical/thermal conductivity. The classification of metal is a wide and complex topic since different industry organizations and countries

	Metallic Materials	Ceramic Materials	Polymeric Materials	Others
General Description	Solid-state material of an element, compound or alloy with good thermal and electrical conductivity.	Solid-state material of compounds with high hardness and brittleness.	Solid-state material with molecules made up of a large number of repeating chemical units and having heavy average molecular weight.	Liquids, carbon nanotube, composite, etc.

Table 1. Major categories of materials used in ESPs

adopt and follow different systems and conventions. This article only focuses on what is most relevant and common to the ESP industry.

In general, metals can be divided into ferrous and nonferrous types, depending on their iron (Fe) content. Ferrous metals contain mostly Fe, and nonferrous metals do not contain appreciable amounts of Fe.

Ferrous Metals

Components in the ESP system using ferrous metals include the head, base, housing, stages, shaft, motor lamination, and cable armor and jacket. Ferrous metals are grouped into several categories, Fig. 1.

Cast iron represents a group of Fe-carbon (C) alloys with a C content higher than 2 wt%. This type of alloy is hard — high compressive strength — and relatively brittle, but can be readily cast in a mold due to their low melting temperatures. ESP shipping caps, pothead housing, and more importantly, stages (impeller and diffuser) are typically made in a casting process from cast iron. The most common cast iron used for ESP stages are nonmagnetic Ni-Resist™ alloys, which have high nickel (Ni) content to provide good corrosion and wear resistant properties for corrosive and abrasive well applications. Ni-Resist Type 1 generally contains Ni 13.5 wt% to 17.5 wt%, chromium (Cr) 1.5 wt% to 2.5 wt%, copper (Cu) 5 wt% to 7 wt% and other elements somewhat. This has historically been the dominant stage material. Ni-Resist Type 4 has the Ni content increased to 29 wt% to 32 wt%, together with 4.5 wt% to 5.5 wt% Cr, and a maximum of 0.5 wt% Cu to further harden the stages for high rate and sandy well applications[1] where improved resistance to erosion and abrasion is required. Ni-Resist Type 4 also offers better oxygen corrosion resistance for surface horizontal pump application[2]. Among all metallic materials, cast iron generally offers the best abrasive wear resistance[3].

Steel is a group of Fe-C alloys with a C content lower than 2 wt% to reduce brittleness and improve tensile strength and machinability. Depending on the content of Cr in the alloy, steel is subdivided into low alloy, carbon steel with Cr < 10.5 wt%, and high alloy with Cr > 10.5 wt%. Carbon steel plates can be rolled, welded and drawn into tubes and used as the ESP's housing. Bar stocks of carbon steel can be machined (drilled, threaded) to make the ESP's head and base. Carbon steel can also be the material for the ESP shaft in low demanding applications. Wrought carbon steel — C content 0.3 wt% maximum — can be used to make cable protector clamps through casting.

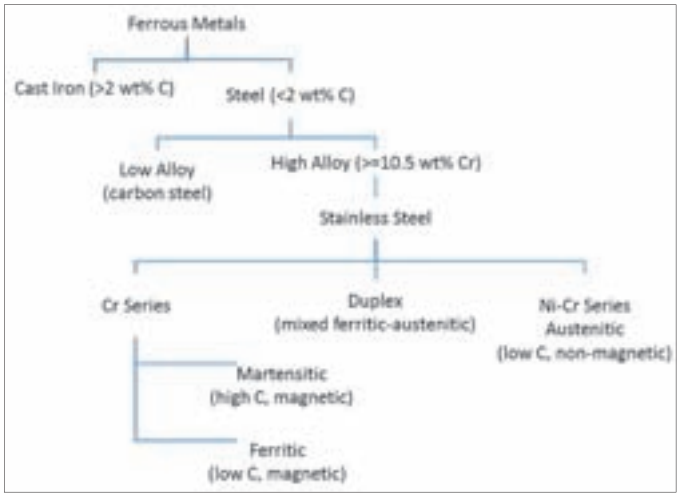

Fig. 1. Ferrous metal classification.

Silicon (Si) steel — also called lamination steel or electrical steel — is a low carbon steel alloy. Commercial grades of Si steel usually have Si content up to 3.2 wt%, manganese (Mn) and aluminum (Al) up to 0.5 wt%. Si significantly increases the electrical resistivity of the steel, which decreases the induced eddy currents and narrows the hysteresis loop of the material, thereby lowering the core loss. Si steel plates with 0.5 mm thickness are widely used as the ESP motor (stator and rotor) lamination.

Galvanized steel is carbon steel coated with a layer of zinc oxide (ZnO). This coating adds some corrosion protection to carbon steel. Galvanized steel is often used as the ESP cable armor, providing mechanical protection for the power cable. Due to the limited thickness and strength of the ZnO coating, galvanized steel is still subject to damage in highly corrosive/abrasive environments[4], and one solution is to use stainless steel armor[5].

Nitralloy™ is a group of low alloys that have gone through the surface hardening treatment process, called nitriding, where nitrogen is diffused into the steel surface to increase its hardness. Nitralloy has been used to make rotor radial bearings for ESP motors.

9Cr-1Mo, also designated as 9% Cr-molybdenum (Mo) steel, is a series of alloy steels intended for high temperature and high-pressure sweet corrosion — carbon dioxide (CO_2) — services. The ability of 9Cr-1Mo to withstand sulfide stress cracking is limited to about 0.7 psi hydrogen sulfide (H_2S) partial pressure[6]. One type of 9Cr-1Mo is Redalloy™. In ESP equipment, the head, base and housing materials are sometimes upgraded from carbon steel to Redalloy to increase their corrosion resistance[4, 7].

The naming or designation of steel can be confusing. In addition to the use of trade names, there are also several classification systems often referenced in the ESP industry. These include systems by the American Iron and Steel Institute (AISI), the Society of Automotive Engineers (SAE) International, and the Unified Numbering System (UNS) for metals and alloys jointly developed by SAE International and the American Society for Testing and Materials (ASTM) International. Cross reference or grade equivalence can be found in online resources or handbooks[8]. For example, the UNS name for low alloy carbon steel AISI 4130 used for the motor shaft in some applications is UNS G41300, and the UNS designation for cast carbon steel ASTM A216 is UNS J03002.

Stainless steel is one type of high alloy with a minimum of 10.5 wt% Cr content. The increase of Cr improves the alloy's corrosion and erosion resistance over carbon steel. Stainless steel can be further classified into several subgroups based on their crystal structures: martensitic, ferritic, austenitic, duplex and super duplex stainless steel.

Martensitic stainless steel — also called the 400-Series stainless steel in SAE designation — generally contains 12 wt% to 18 wt% Cr, and 0.1 wt% to 1.2 wt% C. Common grades of martensitic stainless steel used in the oil field environments include 13Cr, UNS S41000 and UNS S42000. They offer good CO_2 corrosion resistance, but have limited protection against H_2S cracking. Additional CO_2 corrosion protection is provided with super 13Cr, which has a reduced content of C (maximum of 0.03 wt% of C), and increased amounts of Ni (5 wt%) and Mo (2 wt%). In high salinity, severe corrosive ESP applications, 13Cr was found unsuitable due to localized corrosion, although super 13Cr was considered as a more suitable replacement material[4]. Wilson (1986)[9] reported that steels such as 9Cr-1Mo and 13Cr can be the materials for ESP housing and head/base in CO_2 corrosion environments, but are not suitable for H_2S, due to pitting and stress corrosion cracking.

Ferritic stainless steel usually contains 10.5 wt% to 27 wt% Cr, with low C content. It has high ductility and is easily formed. Example grades of ferritic stainless steel includes UNS S43000 and UNS S44400. Lea et al. (1994)[10] reported several cases where ESP housing material was upgrade to ferritic stainless steel alloys to combat CO_2 corrosion. Ferritic steel is good for CO_2 corrosion, but carbon steel with a flame sprayed Monel/epoxy combination coating may be better for H_2S corrosion if mechanical damage to the coating can be prevented[9].

Austenitic stainless steel — also called 300-Series stainless steel — usually contains 16 wt% to 26 wt% Cr, and up to 35 wt% Ni — Ni-Cr series stainless steel. It is in general nonmagnetic (not always true; some austenitic stainless steel, e.g., UNS S30400, becomes magnetic after cold working) and exhibits high tensile strength, ductility and weldability. Example grades of austenitic stainless steel include UNS S30300, S30400, S31600, S31603, and S34565.

Nitronic™ is a family of nitrogen strengthened austenitic stainless steels with better corrosion resistance than UNS S31600 or S31603. XM-19, also referred to as Nitronic 50, has been used as shaft material[11]. Wilson (1986)[9] reported that austenitic stainless steel can withstand CO_2 and H_2S corrosion, but is susceptible to chloride cracking for service in salt water. Shaft couplings made of S30300 can suffer from chloride stress cracking[12]. S34565 was tested as a potential cable jacket material for cable deployed ESPs, and cracks were found to develop in the base metal with chloride levels of 150,000 ppm, and with H_2S as low as 1 mol%[13]. The process of making the cable jacket involves longitudinal welding of metal strips and cold drawn the completed tube into a desired diameter cable. There is no subsequent heat treatment applied to the jacket to avoid damage to the internal power cable. Otherwise, a carbon steel material may be sufficient to make the cable jacket.

Duplex stainless steel is formed from a combination of austenite and ferrite grains, providing high strength/ductility with improved corrosion resistance over either austenitic or ferritic stainless steel. Duplex stainless steel generally contains higher Cr (21 wt% to 24 wt%), lower Ni (4 wt% to 6 wt%), and 2 wt% to 3 wt% Mo. Example grades of duplex stainless steel include 22Cr, UNS S31803 and S32205. UNS S32205 is a potential candidate for the external cable jacket for a cable deployed ESP in non-H_2S environments. It failed in the seam weld area under tests with H_2S as low as 1 mol%, and a chloride level of 150,000 ppm[13].

Super duplex stainless steel is a more highly alloyed material. The addition of Mo and nitrogen provides enhanced corrosion resistance over the duplex stainless steel. Example grades of super duplex stainless steel includes super duplex 25Cr, UNS S32550, S32750, and S32760. Super duplex stainless steel can be formulated for casting. Pump impellers cast from UNS J93380 were shown in seawater pumping applications[14] to withstand sulfide pitting and other forms of corrosion where other materials failed. Pump stages cast from UNS J93404 have been in service in water supply wells to resist chloride pitting attacks.

Nonferrous Metals

Cu and Cu Alloys

Cu exhibits good thermal and electrical conductivity. Conductors in the power cable (solid or stranded wires) and motor stator winding (magnet wires) and rotor conductor bars (round or shaped) are made of Cu. Cu is very susceptive to H_2S corrosion, and good insulation is required[15]. The Cu conductor is generally coated with a tin (Sn)/lead (Pb) alloy when it is insulated with polypropylene to prevent "Cu poisoning" of the insulation. It is sometimes gold plated to provide a H_2S barrier — only molecules thick and subject to damage. Cu has also been utilized as a sacrificial material (H_2S scavengers) in ESP protector (or seal) chambers to slow H_2S migration into the motor[16].

Bronze is an alloy of Cu and Sn — usually about 12%. Bushings — designed to be stationary within the housings — in the radial bearings in the ESP's seal sections are commonly made of bronze. Cu in bronze can react with H_2S in the well fluids. The corrosion product (Cu sulfide) has a higher volume, causing the surface of the bushing to swell. Consequently, bushings may grow or even seize onto the shaft or shaft sleeve — keyed to the shaft, rotating — preventing oil circulation and resulting in the bushing spinning and/or localized overheating. Issues with the bearing can lead to either shaft vibration/movement, shaft seal leakage, fluid invasion into the motor, electrical failure or shaft breakage failure. To prevent a H_2S attack on radial bushings in the ESP protectors, for H_2S environments, it is recommended to avoid use of bronze bushings[16].

One type of bronze is **Al bronze**. It is formed with 6% to

12% of Al added together with some amount of Fe and Ni. Al bronze has been used as magnet retention sleeves in permanent magnet motor designs to overcome the centrifugal forces at high rotational speeds. Bronze, along with brass, Al, Cu, and Zn, are nonmagnetic and does not interact with magnetic fields.

Ni-Al bronze (NAB) has 8 wt% to 11 wt% of Al with the addition of Fe and Ni to give it a higher strength. It is particularly suitable for services with seawater or groundwater containing dissolved oxygen due to its excellent corrosion resistance performance[17, 18]. This material also offers superior protection against cavitation damages[3]. NAB grade C95500 has been used as pump stage material in ESP subsea applications; however, for applications where the water contains sulfide and the pump rate is high, super duplex stainless steel is a more suitable stage material than NAB[14].

Another type of bronze is **Si bronze**. It usually contains about 96% Cu with the remainder being either Si alone, or some amount of other elements such as Mn, Sn, Fe, or Zn. Si bronze plates are usually used for stator lamination at the rotor radial bearing locations.

Brass is an alloy of Cu and Zn. The ESP's motor rotor endrings, bearings and bearing sleeves can be made from brass.

Beryllium (Be) Cu is an alloy of Cu and 0.5 wt% to 3 wt% Be. This is a nonmagnetic, high strength Cu-based alloy. It can be used as stator winding terminals, offering strength, conductivity, hardness, and corrosion resistance.

Ni Alloys

Ni alloys are a group of alloys in which Ni is the base or dominant constituent. These alloys are often called super alloys, and are developed for a wide range of applications demanding superior corrosion resistance and mechanical strength under high temperature. Ni-based alloys common in ESP applications include Monel™, Inconel™, Hastelloy™, and MP35N™.

Monel is a group of alloys composed of Ni, up to 67 wt%, and Cu with small amounts of other elements. With strength greater than pure Ni, Monel is difficult to machine and more expensive than carbon steel. An example of Monel is Monel K-500, which is produced with some amount of Al and titanium added to provide greater strength and corrosion resistance. In highly corrosive conditions, Monel K-500 is used as the material of choice for cable armor[19], shaft, vent plugs, bolts, and washers. The use of Monel coated carbon steel plugs should be avoided since the coating may be chipped away during plug tightening[20].

Inconel is a family of alloys composed of Ni with Cr. Inconel possesses excellent performance characteristics, including mechanical strength and resistance to H_2S, CO_2, chloride corrosion and oxidation at elevated pressure and temperature conditions. Commonly used Inconel in ESP applications includes Inconel 625 (Ni: 58 wt%, Cr: 20 wt% to 23 wt%, Mo: 8 wt% to 10 wt%, with other elements), Inconel 718 (Ni: 50 wt% to 55 wt%, Cr: 17 wt% to 21 wt%, Mo: 2 wt% to 3 wt%, with other elements) and Inconel 825 (Ni: 38 wt% to 46 wt%, Fe: 22 wt% minimum, Cr: 19 wt% to 23.5 wt%, Mo: 2.5 wt% to 3.5 wt%, with other elements). Inconel alloys are the shaft material of choice for demanding applications. Also, to improve the electrical reliability of the motor lead extension cable in H_2S and high salinity environments, Inconel 625 has been used to encapsulate the individual motor lead cable[21] to provide a hermetical seal against the well fluids. For rigless cable deployed ESP applications under H_2S and high chloride corrosive environments, Inconel 825 was tested to be the only suitable material[13] for the cable external jacket. A shaft seal design using Inconel metal bellows offers better performance over a combination of spring and elastomer boot[22]. A metal C-ring made of Inconel 718, coated with silver, is proven reliable as a static sealing solution and is a superior choice over traditional elastomer O-rings in severe service applications.

Hastelloy is a collection of alloys of Ni and Mo. The inclusion of Mo allows this type of alloy to be easily welded, fabricated and formed. The metal bellow shaft seal, cable sheath, and cable armor wires can be made from Hastelloy. One common Hastelloy known as Ni alloy C22 has tungsten (W) added to provide enhanced resistance to pitting, crevice corrosion, and stress corrosion cracking.

MP35N (UNS R30035), is an alloy of Ni and cobalt (Co) with combined strength and stress corrosion cracking resistance in H_2S and salt water environments. It has been used as armor wires in the design for cable deployed ESPs[23].

A Ni-Phosphorous alloy is sometimes used as a coating material for ESP stages to enhance the corrosion and abrasion resistance of pumps.

Pb Alloys

Pure **Pb** is never used in ESP applications. To reduce H_2S attack, motor lead extension (MLE) cable is typically covered with a Pb alloy sheath[20] as a H_2S barrier. Field experiences, however, have shown that the Pb barrier is often inadequate in terms of mechanical strength to protect the MLE and pothead from damage and failures, and cannot be trusted as a positive barrier[16]. Pb is also commonly used as Pb washers for drain or fill ports in the motor and protector. Blanksby et al. (2005)[24] reported that the use of Pb washers in motor drain/fill ports resulted in water leakage into the motor due to the incompatibility between bromide brine and Pb.

Babbitt metals used to coat the surface of the thrust bearing pads refer to several Pb- or Sn-based alloys. The name was taken from its initial creator Isaac Babbitt when he first formulated the alloy in 1839 with a composition of 89.3 wt% Sn, 7.1 wt% antimony, and 3.6% Cu. Babbitt material used in thrust bearings can heat up and begin to smear, leading to shaft vibration, and the consequent leaking of well fluids into motors[25].

Other Metallurgies

Al alloy as an electric conductor has been discussed and used in ESP applications. As a conductor, its conductivity is 60% of an equivalent size Cu wire[26]. The advantage of Al over Cu is its tensile strength. For a rigless cable deployed ESP, Al can be used as the strength member as well as the conductor to simplify the cable design[23]. Cable splicing is a challenge with Al[15]. An Al alloy conductor has demonstrated its capability to survive in environments having high H_2S[27].

Graphalloy™ is a group of metallic materials impregnated with graphite, a form of C crystalline structure. The materials are commonly used as self-lubricating bushing/bearings as a replacement to the tungsten carbide (WC) design.

Samarium Cobalt — an alloy of samarium and Co — and neodymium or simply Neo Magnet — NdFeBr, an alloy of neodymium, Fe and boron — are permanent magnet materials. Applications of these magnet materials in ESPs include permanent magnet motors, magnetic coupling, and levitation.

CERAMIC MATERIALS

Ceramic materials are inorganic, nonmetallic solids, which have strong compression properties (erosion resistance), but in general are brittle (weak in shearing and tension). They are used in an ESP system as radial and thrust bearings. The three common types of ceramics used in the ESP industry are zirconia, silicon carbide (SiC) and WC.

Zirconia is a synthesized ceramic made from zirconium dioxide (ZrO_2) and sometime with magnesium oxide added for enhanced properties. Abrasion resistant zirconia (ARZ) bearings used to be the standard radial bearing design for ESP applications in sandy wells[28].

SiC is a compound of Si and C. SiC ceramic is formed by bonding grains of SiC compounds in the sintering process. This ceramic possesses good thermal conductivity, low thermal expansion, high tensile strength and high corrosion resistance.

WC is a compound of W and C. Fine powders of WC compounds are pressed to form WC ceramic using Ni or Co as a binding material. Sometimes, WC is also called an alloy. In the pure form, WC is a ceramic material. With the addition of Co or Ni, WC behaves like metal and so it can be classified as a metallic material. For example, one grade of WC, YG6X, has WC 94 wt% and Co 6 wt%. The primary use of WC for ESP applications is as radial and thrust bearing — runners and pads — materials in the pump and protector. In addition, WC can also be applied as a coating to the pump's impeller and diffuser, to enhance erosion resistance of the flow passages[29]. In some high horsepower applications[30], bronze bushings were replaced with WC bushings after motor premature wear/failures were experienced with bronze bushings in rotor bearings and head/base radial bearings.

In general, the hardness — wear resistance — of several common materials can be listed in an increasing order[26, 31] as: Cu < Ni-Resist < quartz < zirconia < WC < SiC < diamond. Radial bearings of abrasion resistant pumps traditionally used zirconia materials. In very abrasive applications, bearing materials have to be upgraded to harder and more wear resistant materials such as SiC and WC to improve system reliability[1]. In some applications the combination of two ceramic materials had been used for bushings and sleeves, respectively, i.e., zirconia SiC[22, 32]. Some companies prefer to use WC as the default/standard radial bearing design. Besides hardness or wear resistance capability, material tolerance to impact or toughness is an equally important parameter to consider when selecting the most suitable bearing material. In terms of toughness, the three ceramics are ranked[32] as: zirconia > WC > SiC. Zirconia offers better impact toughness, but is not as hard and wear resistant as SiC. SiC is hard enough, but can break up due to impact induced by, for example, gas slugging. For high sand production with slugging, it was decided to use a better grade of WC for the bearing material, which is slightly less hard than SiC, but much more impact resistant.

DISCUSSIONS

Table 2 provides a summary of commonly used metallic and ceramic materials as they are applied to each major ESP component. This is not intended to be an exhaustive list. The philosophy of material selection for any particular application is a balancing act and optimization process with several factors taken into consideration: material cost, functionality, and manufacturability. For example, the choice for pump stage material ranges from low cost cast iron, to more expensive Ni-Al bronze and super duplex stainless steel. The more expensive materials can be the overall cost-effective solution for critical applications demanding corrosion resistant, reliable equipment after considering repair and replacement cost and lost production. A comparison on corrosion resistance performance and relative cost of various metallic materials can be found in Strang (2006)[17].

It is worth pointing out that material quality, even a slight variation, sometimes can have a significant impact on performance. Testing is required to ensure material quality.

An ESP system is an integration of hundreds of components/elements. In selecting materials, mechanical and chemical compatibility needs to be taken into account since it plays an important role on system functionality and reliability. For example, Merrill and Dwiggins (2017)[11] discussed the importance of having balanced thermal growth between the protector shaft and the housing to prevent shaft seal movement, fluid ingress, and motor electrical failures. Chemical incompatibility between dissimilar metals in close contact can lead to galvanic corrosion and system failures in the presence of an electrolyte. This can happen between the ESP string — super duplex steel diffusers — and the carbon steel tubular pup joint[33] and between the different components — stainless steel head/base and carbon steel housing — within the ESP system[34].

Moreover, the choice of material has to be combined with

ESP Component	Commonly used Metallic and Ceramic Materials
Head, Base, and Housing	Carbon steel; carbon steel with coating (flame spray stainless steel or Monel coat with epoxy overcoat; phosphate coatings) Redalloy, and stainless steel
Shaft	Carbon steel, Nitronic 50, Monel, and Inconel
Stage	Gray cast iron, white cast iron, Ni-Resist Type 1, Ni-Resist Type 4, Ni-Al bronze, stainless steel Stage coating: WC
Bushing, Sleeve, and Abrasion Resistance Insert	Bronze, Ni-Resist, zirconia, WC, and Graphalloy
Protector Thrust Bearing and Runner	Thrust pad: bronze, Babbitt, Si or WC Runner: heat treated stainless steel, WC
Mechanical (shaft) Seal	Face seal: stainless steel, bronze, Monel, WC, and SiC Spring/retainer: Monel Metal bellow: Hastelloy and Inconel
Motor Winding/Lamination	Magnetic wire (Cu), Si steel, Si bronze, samarium Co
Motor Thrust Bearing and Runner	Bronze, Babbitt, WC, and stainless steel
Motor Rotor Bearing and Head/Base Radial Bearing	Brass, bronze, Nitralloy, Co alloy, and WC
Cable	Conductor: solid or stranded Cu with Pb or Sn coating Jacket (gas barrier): Pb Armor: galvanized steel, stainless steel, Monel, Hastelloy Cable band: stainless steel, Monel Solid cast cable clamp: wrought carbon steel Cable encapsulation for CDESP: austenitic stainless steel, duplex stainless steel, Inconel
Bolts, screw, washer, coupling, fasteners, plug, bag clamp, and relief valve	Carbon steel, Si bronze, Pb, stainless steel, Monel, Inconel

Table 2. Commonly used metallic and ceramic materials of major components in an ESP

improved designs to achieve higher reliability. For example, one common design of the radial bearing for the pump and protector is to have the sleeve keyed to the shaft. Bearing sleeve cracks have been reported as a cause of failure[1] for abrasive well applications. An improved design is to change the sleeve to a keyless design, removing the stress concentration and enhancing the impact tolerance[32]. Another way to address reliability is to apply redundancy. As an example, to enhance shaft stability in sandy applications the number of radial bearings in a pump can be increased from one bearing for every three stages to a full bearing housing, i.e., one bearing for every stage[1].

CONCLUSIONS

This article reviewed and discussed the different types of metallic and ceramic materials commonly in use in the ESP industry. Relevant properties and suitable application areas are briefly highlighted. The article is intended to be a high level guide to help engineers develop some basic understanding on ESP materials. This knowledge is required to correctly specify materials and understand failures so that ESP run life can be improved. For any particular application, defining material specifications is often an evolving process and always involves considerations of factors such as material cost, the ability to function, and the ability to fabricate. In addition, ESP run life depends not only on materials, but is also equally important on design, quality fabrication, e.g., on critical dimensions, assembly, testing, installation, and operation.

A follow-up article is planned to discuss polymeric and other materials used in ESP systems.

ACKNOWLEDGMENTS

The authors would like to thank the management of Saudi Aramco and Alkhorayef Petroleum Company for their support and permission to publish this article.

This article was presented at the SPE Artificial Lift Conference and Exhibition — Americas, The Woodlands, Texas, August 28-30, 2018.

REFERENCES

1. Sanchez, L.M., Maldonado, J.S., Martin, J.L., Vargas, H., et al.: "First Successful Experience of Hardened Stages for Sandy Wells at Northern Llanos Field, Case History," SPE paper 185270, presented at the SPE Electric Submersible Pump Symposium, The Woodlands, Texas, April 24-28, 2017.

2. Saveth, K.: "New Stage Material Combined with Permanent Magnet Motor Technology Widens ESP Application Window," SPE paper 171348, presented at the SPE Artificial Lift Conference and Exhibition — North America, Houston, Texas, October 6-8, 2014.

3. Budris, A.R.: "The Impact of Component Material Selection on Pump Reliability," *WaterWorld*, Vol. 30, Issue 12, December 2014.

4. Brahmi, H.: "Recommended Solutions for ESP Installed in Very High Salinity Reservoirs and Severe Corrosive Media," SPE paper 184181, presented at the SPE Middle East Artificial Lift Conference and Exhibition, Manama, Kingdom of Bahrain, November 30-December 1, 2016.

5. Al-Jabri, J. and Al-Farsi, I.: "Significant Electric Submersible Pumps (ESP) Run Life Improvement in OXY Oman," presentation presented at the SPE Workshop Maximizing ESP Lifting: Solutions for Today and Tomorrow, Muscat, Oman, January 24-25, 2018.

6. Trasatti, S., Scoppio, L. and Cheldi, T.: "H_2S and CO_2 Corrosion of Some 9Cr1Mo Alloys for Downhole Applications," paper presented at the NACE International/ CORROSION 2001 Conference and Exposition, Houston, Texas, March 11-16, 2001.

7. Gallegos, M., Ordonez, E.F., Milne, A.W. and Robles, M.: "Stimulation in Wells with Electric Submersible Pumps Increases Production and Save Costs without Damaging Pumps," SPE paper 152320, presented at the SPE Latin America and Caribbean Petroleum Engineering Conference, Mexico City, Mexico, April 16-18, 2012.

8. Huyett, G.L.: *Engineering Handbook: Steelmaking Materials, Attributes, and Manufacturing Processes*, 2nd edition, 2004, 144 p.

9. Wilson, B.L.: "Materials for ESPs in Corrosive Environments," paper presented at the Electric Submersible Pump Workshop, Houston, Texas, April 8-9, 1986.

10. Lea, J.F., Wells, M.R., Bearden, J.L., Wilson, L., et al.: "Electrical Submersible Pumps: On and Offshore Problems and Solutions," SPE paper 28694, presented at the International Petroleum Conference and Exhibition of Mexico, Veracruz, Mexico, October 10-13, 1994.

11. Merrill, D. and Dwiggins, J.: "Understanding Seal Sections and the Phantom Failures," SPE paper 185133, presented at the SPE Electric Submersible Pump Symposium, The Woodlands, Texas, April 24-28, 2017.

12. Wilson, B.L. and Comeau, T.P.: "Increasing the Run Life of ESPs in High H_2S Wells," SPE paper 28527, presented at the SPE Annual Technical Conference and Exhibition, New Orleans, Louisiana, September 25-28, 1994.

13. Brian, B.A., Xiao, J. and Paquette, M.: "Novel Electric Submersible Pump Cable Operates in High H_2S Production Environment," SPE paper 188737, presented at the Abu Dhabi International Petroleum Exhibition and Conference, Abu Dhabi, UAE, November 13-16, 2017.

14. Francis, R. and Hebdon, S.: "The Selection of Stainless Steels for Seawater Pumps," paper presented at the NACE International/CORROSION 2015 Conference and Exposition, Dallas, Texas, March 15-19, 2015.

15. Del Pino, J.J., Nunez, W., Maldonado, J.S., Martin, J.L., et al.: "Implementation of Torque and Drag Analysis to Simulate Forces While Running in Hole Electric Submersible Pump — ESP Assemblies, to Reduce Power Cable Mechanical Damages," SPE paper 185269, presented at the SPE Electric Submersible Pump Symposium, The Woodlands, Texas, April 24-28, 2017.

16. Al-Khalifa, M.A., Shepler, R.A., Cox, R.L. and Al-Quwizani, S.A.: "ESP Reliability Lessons Learned from Three H_2S Saudi Arabia Fields," SPE paper 184176, presented at the SPE Middle East Artificial Lift Conference and Exhibition, Manama, Kingdom of Bahrain, November 30-December 1, 2016.

17. Strang, J.R.C.: "Cast Valve Materials for Seawater Service: Nickel-Aluminum Bronze and its Rivals," paper P0607, presented at the Valve World Conference at the Maastricht Exhibition and Congress Center, Maastricht, the Netherlands, November 7-9, 2006.

18. Jha, M., Singh, R., Chavan, C., Karthik, R., et al.: "High Rate ESP Application in Onshore Rajasthan Fields: A Case Study," SPE paper 163117, presented at the SPE Artificial Lift Conference and Exhibition, Manama, Kingdom of Bahrain, November 27-28, 2012.

19. Brahmi, H., Grifantini, S. and Abouzid, M.: "Run Life Extension of ESP Installed in Very High Salinity Reservoirs and Severe Corrosive Media Case Study," paper presented at the Offshore Mediterranean Conference and Exhibition, Ravenna, Italy, March 29-31, 2017.

20. Durham, M.O. and Miller, G.: "Enhancing Performance of Submersibles Operating in Miscible Flood Conditions," SPE paper 25446, presented at the SPE Production Operations Symposium, Oklahoma City, Oklahoma, March 21-23, 1993.

21. Xiao, J., Shepler, R., Windiarto, Y., Parkinson, S., et al.: "Development and Field Test of an Electric Submersible Pump Reliable Power Delivery System," *SPE Production & Operations*, Vol. 33, Issue 3, August 2018, pp. 449-458.

22. Pastre, L.F. and Fastovets, A.: "The Evolution of ESP Technology in the North Sea: A Reliability Study Based on Historical Data and Survival Analysis," SPE paper 187735, presented at the SPE Russian Petroleum Technology Conference, Moscow, Russia, October 16-18, 2017.

23. Xiao, J., Roth, B.A., Lastra, R., Sarawaq, Y., et al.: "Cable Concept Evaluation for ESP Rigless Deployment," SPE

paper 184193, presented at the SPE Middle East Artificial Lift Conference and Exhibition, Manama, Kingdom of Bahrain, November 30-December 1, 2016.

24. Blanksby, J.M., Hicking, S. and Milne, W.H.: "Deployment of High Horsepower ESPs to Extend Brent Field Life," SPE paper 96797, presented at the Offshore Europe Conference, Aberdeen, U.K., September 6-9, 2005.
25. Bowen, C.G. and Kennedy, R.J.: "Electric Submersible Pumps — Improving Run Lives in the North Kaybob BHL Unit No. 1," SPE paper 19379, 1989, unpublished.
26. Takacs, G.: *Electrical Submersible Pumps Manual: Design, Operations, and Maintenance*, 1st edition, Gulf Professional Publishing, 2009, 440 p.
27. Vandevier, J.: "Electric Submersible Pumping Systems — Yesterday's Challenges, Today's Opportunity," paper presented at the Electric Submersible Pump Workshop, Houston, Texas, April 8-9, 1986.
28. Abdou, H.A.: "Case History in Solving ESP Problems in Oil and Water Wells," SPE paper 49542, presented at the Abu Dhabi International Petroleum Exhibition and Conference, Abu Dhabi, UAE, October 11-14, 1998.
29. Horn, M., Coudeville, F., Bespalov, E. and Butcher, H.: "Otter: the World's Longest Subsea Tie-back with Dual ESP," OTC paper 15369, presented at the Offshore Technology Conference, Houston, Texas, May 5-8, 2003.
30. Del Pino, J.J., Martin, J.L., Gomez, S., Gonzalez, A., et al.: "Electric Submersible Pumps (ESP) Performance Improvement by Implementation of Extreme Performance Motor Technology in Cano Limon Field," SPE paper 173915, presented at the SPE Artificial Lift Conference — Latin America and Caribbean, Salvador, Bahia, Brazil, May 27-28, 2015.
31. Wilson, B.L.: "The Effects of Abrasives on Electric Submersible Pumps," *SPE Drilling Engineering*, Vol. 5, Issue 2, June 1990, pp. 171-175.
32. Muecke, N.B., Kapelhoff, G.H. and Watson, A.: "ESP Design Changes for High GLR and High Sand Production; Apache Stag Project," SPE paper 77801, presented at the SPE Asia Pacific Oil and Gas Conference and Exhibition, Melbourne, Australia, October 8-10, 2002.
33. Kalu-Ulu, T.C. and Salemeh, A.E.: "Issues of Material Compatibility in Artificial Lift Completions: Case Study of Harsh Water Wells," SPE paper 183853, presented at the SPE Middle East Oil and Gas Show and Conference, Manama, Kingdom of Bahrain, March 6-9, 2017.
34. Britvar, J. and Williams, S.: "Improving ESP Application for Unconventional Wells in the Bakken," SPE paper 185150, presented at the SPE Electric Submersible Pump Symposium, The Woodlands, Texas, April 24-28, 2017.

BIOGRAPHIES

Dr. Jinjiang Xiao is a Senior Petroleum Engineering Consultant working in Saudi Aramco's Exploration and Petroleum Engineering Center – Advanced Research Center (EXPEC ARC). His current focus is artificial lift research and development.

Prior to joining Saudi Aramco in 2003, Jinjiang spent 10 years with Amoco and later BP-Amoco, working on multiphase flow, flow assurance and deepwater production engineering.

He received both his M.S. and Ph.D. degrees in Petroleum Engineering from the University of Tulsa, Tulsa, OK.

Rafael A. Lastra is a Petroleum Engineering Consultant working with the Production Technology Division of Saudi Aramco's Exploration and Petroleum Engineering Center – Advanced Research Center (EXPEC ARC). He provides internal consultation related to artificial lift technologies, especially in the area of electric submersible pumps.

Rafael has more than 25 years of extensive and versatile oil industry experience obtained through a variety of international engineering and management positions, including research and development, management of artificial lift operations, project control, and business development.

He received his B.S. degree in Electrical Engineering from the Universidad del Valle, Cali, Valle del Cauca, Colombia, and his M.S. degree in Management of Information Systems from Texas A&M University, College Station, TX.

Brian A. Roth is a Petroleum Engineering Consultant in the Production Technology Division of Saudi Aramco's Exploration and Petroleum Engineering Center – Advanced Research Center (EXPEC ARC). His focus is on R&D efforts with an emphasis on artificial lift technologies. Before joining Saudi Aramco in 2012, Brian spent over 25 years in engineering and leadership roles in large oil and gas service companies.

He has over 24 applied and granted patents, and has authored or coauthored several technical and journal papers.

Brian received his B.S. degree in Mechanical Engineering from the University of Texas at Austin, Austin, TX, and an MBA degree from Texas A&M University, College Station, TX.

Dr. Woon Lee is the R&D Manager of Alkhorayef Petroleum Company, Dammam, Saudi Arabia, which is a supplier of electric submersible pump (ESP) equipment.

Prior to joining Alkhorayef in 2008, he spent 18 years with Reda, a Schlumberger company, and later with Weatherford ESP, working on designs of pumps, gas separators, and gas handling pumps.

Woon received both his M.S. and Ph.D. degrees in Mechanical Engineering from Rice University, Houston, TX.

SUBSCRIPTION ORDER FORM

To begin receiving the *Saudi Aramco Journal of Technology* at no charge, please complete this form.

Please print clearly.

Name _____

Title _____

Organization _____

Address _____

City _____

State/Province _____

Postal code _____

Country _____

E-mail address _____

Number of copies _____

TO ORDER

By phone/email:

Saudi Aramco Corporate Communication Support Department
JOT Distribution
+966-013-876-0498
william.bradshaw.1@aramco.com

By mail:

Saudi Aramco Corporate Communication Support Department
JOT Distribution
Box 5000
Dhahran 31311
Saudi Arabia

Current issues, select back issues and multiple copies of some issues are available upon request.

The *Saudi Aramco Journal of Technology* is published by the Saudi Aramco Corporate Communication Support Department, Saudi Arabian Oil Company, Dhahran, Saudi Arabia.

GUIDELINES FOR SUBMITTING AN ARTICLE TO THE SAUDI ARAMCO JOURNAL OF TECHNOLOGY

These guidelines are designed to simplify and help standardize submissions. They need not be followed rigorously. If you have additional questions, please feel free to contact us at CCSD. Our address and phone numbers are listed on page 76.

Length

Varies, but an average of 2,500-3,500 words, plus illustrations/photos and captions. Maximum length should be 5,000 words. Articles in excess will be shortened.

What to send

Send text in Microsoft Word format via email or on disc, plus one hard copy. Send illustrations/photos and captions separately but concurrently, both as email or as hard copy (more information follows under file formats).

Procedure

Notification of acceptance is usually within three weeks after the submission deadline. The article will be edited for style and clarity and returned to the author for review. All articles are subject to the company's normal review. No paper can be published without a signature at the manager level or above.

Format

No single article need include all of the following parts. The type of article and subject covered will determine which parts to include.

Working title

Abstract

Usually 100-150 words to summarize the main points.

Introduction

Different from the abstract in that it "sets the stage" for the content of the article, rather than telling the reader what it is about.

Main body

May incorporate subtitles, artwork, photos, etc.

Conclusion/summary

Assessment of results or restatement of points in introduction.

Endnotes/references/bibliography

Use only when essential. Use author/date citation method in the main body. Numbered footnotes or endnotes will be converted. Include complete publication information. Standard is *The Associated Press Stylebook*, 52nd ed. and *Webster's New World College Dictionary*, 5th ed.

Acknowledgments

Use to thank those who helped make the article possible.

Illustrations/tables/photos and explanatory text

Submit these separately. **Do not place in the text.** Positioning in the text may be indicated with placeholders. Initial submission may include copies of originals; however, publication will require the originals. When possible, submit both electronic versions, printouts and/or slides. Color is preferable.

File formats

Illustration files with .EPS extensions work best. Other acceptable extensions are .TIFF, .JPEG and .PICT.

Permission(s) to reprint, if appropriate

Previously published articles are acceptable but can be published only with written permission from the copyright holder.

Author(s)/contributor(s)

Please include a brief biographical statement.

Submission/Acceptance Procedures

Papers are submitted on a competitive basis and are evaluated by an editorial review board comprised of various department managers and subject matter experts. Following initial selection, authors whose papers have been accepted for publication will be notified by email.

Papers submitted for a particular issue but not accepted for that issue will be carried forward as submissions for subsequent issues, unless the author specifically requests in writing that there be no further consideration. Papers previously published or presented may be submitted.

Submit articles to:

Editor
The *Saudi Aramco Journal of Technology*
C-11B, Room AN-1080
North Admin Building #175
Dhahran 31311, Saudi Arabia
Tel: +966-013-876-0498
Email: *william.bradshaw.1@aramco.com.sa*

Submission deadlines

Issue	Paper submission deadline	Release date
Summer 2019	February 13, 2019	June 30, 2019
Fall 2019	May 15, 2019	September 30, 2019
Winter 2019	August 1, 2019	December 31, 2019
Spring 2020	November 12, 2019	March 31, 2020

NOTES:

NOTES:

NOTES:

Deployment of Liner Systems in Extreme High Mud Weight Environments in Gas Wells

Abdullah H. Oqaili, Abdulaziz S. Alluhaydan, Peter C. Ezi, and Alvaro Tirado

ABSTRACT

During the development phase of a gas field, the abnormal pressure in a dolomitic limestone formation demanded an extremely high mud weight (MW) to control the well. The casing design of this case study field has entailed the installation of a 7" × 9⅝" liner hanger in combination with a liner top packer followed by a tie back to the surface. Due to this hole section being directly above the pay zone, it is crucial that the liner installation and the wellbore integrity are not compromised for the subsequent well completion.

Further Insight into Calcium Carbonate Scale Inhibition at High Temperature

Dr. Qiwei Wang and Dr. Tao Chen

ABSTRACT

Threshold inhibitors are commonly used to prevent scale formation in oil field production systems. Effective scale control still remains a significant challenge under harsh environmental conditions such as high temperatures. The risk of calcium carbonate ($CaCO_3$) scale deposition is increased with higher temperatures by the inverse solubility behavior, which will accelerate the precipitation kinetics; while the inhibitor performance deteriorates with thermal degradation, incompatibility with produced water, and decreased inhibition efficiency. Although extensive works have been devoted to study the $CaCO_3$ inhibition behavior, the performance of inhibitors under harsh conditions is still not fully understood.

Integrated 3D Geomechanics Model to Characterize the in Situ Stress Rotations and their Implications on the Mechanical Behavior of the Natural Fractures and Drilling Operations: A Case Study for a Carbonate Reservoir, Saudi Arabia

Dr. Tariq Mahmood, Otto E. Meza, Ali H. Al-Gawas, Khalid A. Al-Hawas, Abdulrazaq Reda Nashar, Dr. Ivan Deshenenkov, and Carlos A. Planchart

ABSTRACT

This work presents the determination of the in situ stress field of a carbonate reservoir in a complex tectonic area within the Arabian Plate. The detailed determination of the stress field is important to field characterization as it controls the fundamental mechanical behavior of open and closed fractures. The presence of open natural fractures can have an adverse effect on drilling operations, e.g., "total loss circulation," etc. An integrated 3D geomechanical model was built to characterize the rock mechanical properties and the stress orientations to analyze the behavior of natural fractures and micro-faults under the current state of stress.

An Effective Approach Using Microemulsion Treatment Techniques to Remove Sandstone Formation Damage: Lab Testing and Field Application

Hussain A. Almajid, Hisham I. Al-Shuwaikhat, Saleh M. Abou Zeid, and Ajay Kumar V. Addagalla

ABSTRACT

Matrix stimulation treatments executed with coiled tubing (CT) face various challenges in terms of design, execution, and evaluation. The design phase typically relies on information that is usually poorly known, e.g., extent of damage. Treatment pumping schedules and fluid concentrations are often determined based on previous experience and accepted local practices. In most cases, tools like high-pressure differential jetting nozzles are used to provide deeper penetration and lower breakout pressures. The depths at which these tools are operated usually depend on a prior log interpretation. The treatment evaluation is typically limited to the comparison of pre- and post-stimulation wellhead pressures and rates.